



# Etude et réalisation d'un magnétomètre isotrope miniature à pompage optique de l'hélium -4

Jaroslav Rutkowski

## ► To cite this version:

Jaroslav Rutkowski. Etude et réalisation d'un magnétomètre isotrope miniature à pompage optique de l'hélium -4. Signal and Image processing. Université de Franche-Comté, 2014. English. NNT : 2014BESA2005 . tel-01345743

**HAL Id: tel-01345743**

**<https://theses.hal.science/tel-01345743>**

Submitted on 15 Jul 2016

**HAL** is a multi-disciplinary open access archive for the deposit and dissemination of scientific research documents, whether they are published or not. The documents may come from teaching and research institutions in France or abroad, or from public or private research centers.

L'archive ouverte pluridisciplinaire **HAL**, est destinée au dépôt et à la diffusion de documents scientifiques de niveau recherche, publiés ou non, émanant des établissements d'enseignement et de recherche français ou étrangers, des laboratoires publics ou privés.

# SPIM

## Thèse de Doctorat



école doctorale sciences pour l'ingénieur et microtechniques  
UNIVERSITÉ DE FRANCHE-COMTÉ

# Study and Realization of a Miniature Isotropic Helium Magnetometer



RUTKOWSKI Jarosław

Thèse soutenue le 11/03/14

Thèse préparée au CEA – LETI – Direction de la Recherche Technologique

Département Systèmes et Intégration Système

Service Capteurs et Systèmes Electroniques

Laboratoire Capteurs Innovants





# Thèse de Doctorat de l'Université de Franche-Comté

Jarosław RUTKOWSKI

## Study and Realization of a Miniature Isotropic Helium Magnetometer

### Composition du Jury:

J. DZIUBAN	Rapporteur	Professeur	Wrocław University of Technology, Pologne
L. WINDHOLZ	Rapporteur	Professeur	Graz University of Technology, Autriche
V. GIORDANO	Président du jury	HDR	FEMTO-ST Besançon, France
C. GORECKI	Directeur de thèse	HDR	FEMTO-ST Besançon, France
R. LAMMEGGER	Examinateur	Docteur	Graz University of Technology, Autriche
S. LECOMTE	Examinateur	Docteur	CSEM Neuchâtel, Suisse
S. MORALES	Encadrante CEA	Docteur	CEA-LETI Grenoble, France
J-M. LEGER	Invité	Docteur	CEA-LETI Grenoble, France





## Remerciements / Acknowledgments

Cette thèse a été réalisée au sein du Laboratoire des Capteurs Innovants du CEA-Leti à Grenoble au cours des années 2011-2014. J'aimerais remercier Matthieu Le Prado de m'avoir accueilli et m'avoir donné l'opportunité de rejoindre son équipe.

Un grand merci à Sophie Morales qui a infatigablement suivi mon travail du début jusqu'à fin et qui a toujours su trouver le temps pour orienter mon travail sur la bonne voie.

Je remercie Jean-Michel Léger pour son enthousiasme constant et la relecture critique du mémoire.

Je remercie également mon directeur de thèse, Christophe Gorecki, pour ses nombreux conseils.

I would like to thank J. Dziuban, L. Windholz, V. Giordano, R. Lammegger and S. Lecomte for accepting to take part in my thesis committee, insightful review of the manuscript and difficult questions.

Je veux également remercier F. Alcouffe, T. Amrane, M. Baicry M. Béranger F. Bertrand, A. Boness, MC. Corsi, E. Delevoye, W. Fourcault, C. Gobbo, T. Jager, V. Josselin, A. Palacios-Laloy et Y. Troadec pour leurs nombreuses contributions.

A Grenoble, le 16 janvier 2014



## Résumé

Les magnétomètres à pompage optique souffrent de problèmes d'anisotropie liés aux zones d'ombre et d'erreurs directionnelles qui limitent leur précision. Ces problèmes sont directement liés à leur principe de fonctionnement. Afin de pouvoir répondre aux besoins des applications mobiles, les magnétomètres atomiques utilisent des architectures complexes reposant par exemple sur l'utilisation de trois capteurs orthogonaux ou de plusieurs résonances (cas des magnétomètres CPT). Le CEA-LETI a conçu un magnétomètre isotrope à pompage optique de l'hélium-4. Ce capteur est caractérisé par une sensibilité de  $1 \text{ pT}/\sqrt{\text{Hz}}$  (DC-100 Hz) et une précision meilleure que 45 pT. Son isotropie est assurée par un moteur piézoélectrique qui maintient l'axe de la polarisation rectiligne du faisceau pompe à angle droit avec le champ magnétique à mesurer.

Cette thèse se focalise sur la miniaturisation de ce magnétomètre. Elle est une continuation des travaux réalisés par le CEA-LETI et le CNES dans le cadre du projet SWARM de l'Agence Spatiale Européenne.

La miniaturisation nécessite une étude détaillée des lois d'échelle qui décrivent le comportement du capteur et ses caractéristiques. Pour ce faire, un modèle numérique a été développé. Les mesures expérimentales des caractéristiques les plus importantes (densité des atomes métastables et temps de relaxation) confirment la pertinence du modèle théorique. Le modèle permet de prévoir la gamme de pression optimale de remplissage des cellules d'hélium et la limite théorique du bruit du capteur.

Le processus de miniaturisation nécessite également une redéfinition de l'architecture globale du système. Un rotateur de polarisation à cristaux liquides a été identifié pour remplacer le moteur piézoélectrique, utilisé dans le projet SWARM. Ce composant a un grand potentiel de miniaturisation et est parfaitement compatible avec les techniques de fabrication collective. Les premiers rotateurs à cristaux liquides ont été fabriqués et caractérisés. Ce composant permet d'effectuer une rotation de la polarisation dans la gamme entre 0 et plus que 300 degrés avec des temps de réponse compatibles avec les applications mobiles et spatiales. Les résultats montrent que la construction du rotateur et son pilotage électrique sont amagnétiques et peuvent par conséquent être appliqués dans la construction d'un magnétomètre isotrope à pompage optique de l'hélium-4.

Suite à ces étapes, un premier démonstrateur d'un magnétomètre isotrope miniature à l'hélium-4 a été conçu et caractérisé. La valeur maximale de la sensibilité, obtenue avec une cellule d'hélium de  $100 \text{ mm}^3$  de volume et un rotateur de polarisation à cristaux liquides, est voisine de  $8 \text{ pT}/\sqrt{\text{Hz}}$ . Cette valeur peut encore être optimisée.

En parallèle, les briques de base d'un magnétomètre tout intégré ont été étudiées individuellement. Des VCSELs ont été réalisés pour remplacer le laser à fibre. Une architecture de magnétomètre tout optique a été proposée. Enfin, des premières cellules d'hélium micro-fabriquées en verre-silicium-verre ont été réalisées. Les premiers résultats expérimentaux montrent qu'il est possible de confiner de l'hélium dans une structure de ce type, ce qui ouvre la voie à un processus de fabrication collective.

## Summary

Optically pumped magnetometers suffer from dead zones and heading errors that limit their accuracy. These problems are inherently related to their operating principle. In order to meet the isotropy requirements of mobile applications, atomic sensors use complex architectures, for example three orthogonally mounted sensors or multiple resonances (case of CPT sensors). CEA-LETI has successfully designed and manufactured an isotropic  $^4\text{He}$  magnetometer with a  $1 \text{ pT}/\sqrt{\text{Hz}}$  resolution (DC-100 Hz) and an accuracy better than 45 pT. Its isotropy is obtained thanks to a non-magnetic servo-driven piezoelectric motor which fixes the axis of linear polarization of pumping light at right angle with respect to the magnetic field to be measured.

This thesis concentrates on the miniaturization of the isotropic helium-4 magnetometer. It is a continuation of the work realized by the CEA-LETI and CNES within the SWARM project of the European Space Agency.

Miniaturization requires a study of the scaling laws, which describe the behavior of the sensor and its characteristics during the miniaturization process. To this end, a theoretical model whas been developed. Experimental measurements of key characteristics (metastable atom density and their relaxation time) show a reasonably good agreement with theoretical expectations. The model allows to predict the optimal value of pressure, with which the glass cells of the miniature magnetometer have to be filled as well as the theoretical shot noise level of the miniature sensor.

The miniaturization process needs the system architecture to be redefined. Some of the components used in the macroscopic version should be replaced with ones allowing easy integration.

A polarization rotator based on liquid crystals has been identified as a replacement of the piezoelectric motor, used to provide isotropic measurements in the SWARM magnetometer. This device has a large miniaturization potential and is fully compatible with semiconductor batch processing. Sample structures of this type have been fabricated and characterized. The device allows a continuous polarization rotation from  $0^\circ$  to more than  $300^\circ$  with response times sufficient for mobile or space applications. Results have shown that the construction of the developed liquid crystal polarization rotator as well as its electrical driving scheme are non-magnetic and therefore can be successfully applied in the construction of a miniature isotropic Earth's field helium-4 magnetometer.

In the next step, a first demonstrator of a miniature isotropic  $^4\text{He}$  magnetometer has been designed and characterized. An overall magnetic field sensitivity around  $8 \text{ pT}/\sqrt{\text{Hz}}$  has been obtained using a  $100 \text{ mm}^3$  glassblown gas cell and the liquid crystal rotator. This sensitivity could be further optimized.

Furthermore, first steps towards a "chip-scale" physics package of the sensor have been realized. A batch of microfabricated helium cells has been fabricated. Experimental tests gave promising results since the possibility of confinement of helium inside glass-silicon-glass microfabricated cells has been confirmed.

## Table of contents

Table of contents .....	9
List of abbreviations .....	11
List of symbols .....	13
Introduction .....	15
1. Atomic magnetometers – operating principle and state of the art .....	21
1.1. Physical principles of helium-4 magnetometers.....	21
1.1.1. Optical pumping .....	23
1.1.2. Magnetic resonance .....	23
1.1.3. Detection of resonance – absorption signals .....	25
1.1.4. Isotropy of measurement .....	27
1.1.5. Practical realization – the SWARM magnetometer .....	30
1.2. State of the art on miniature atomic magnetometers .....	31
1.2.1. Optically pumped helium magnetometer – Polatomic Inc. ....	32
1.2.2. Coherent population trapping magnetometers.....	33
1.2.3. $M_x$ alkali-vapor magnetometers.....	34
1.2.4. All-optical Bell-Bloom alkali-vapor magnetometers .....	36
1.2.5. Spin Exchange Relaxation-Free (SERF) magnetometers.....	37
1.2.6. Summary .....	39
1.2.7. Conclusion.....	41
2. Helium gas cells .....	45
2.1. Desired specifications.....	45
2.2. Glassblown cells.....	46
2.3. Gas purity .....	47
2.4. Impedance matching.....	49
2.4.1. Electrical equivalent circuit of the discharge .....	49
2.4.2. Resonant impedance matching networks .....	49
2.4.3. Discharge impedance and power transfer.....	51
2.5. High-frequency breakdown and the low pressure limit.....	54
2.5.1. HF breakdown mechanism .....	55
2.5.2. Breakdown voltage measurement.....	57
2.6. Alfa and gamma modes and the high pressure limit .....	61
2.7. Optimal pressure and its scaling with size .....	63
2.7.1. Metastable density .....	63
2.7.2. Metastable relaxation.....	76
2.7.3. Optimal pressure.....	83
2.8. Conclusion.....	84
3. The architecture of the sensor.....	89

3.1.	Desired specifications.....	89
3.2.	Magnetically vs. optically driven spin precession mode .....	89
3.2.1.	Optically driven Spin Precession (OSP).....	90
3.2.2.	Conclusion.....	92
3.3.	Optical architecture .....	92
3.3.1.	Optical source – laser .....	92
3.3.2.	Light collimation .....	100
3.4.	HF electrode geometry .....	102
3.5.	Isotropy of measurement and the liquid crystal polarization rotator.....	103
3.5.1.	State-of-the-art polarization rotation techniques .....	103
3.5.2.	Operating principle and construction of the liquid crystal polarization rotator.....	105
3.5.3.	Performance of the LC polarization rotator.....	106
3.6.	System architecture .....	108
3.7.	Conclusion.....	109
4.	First demonstrator of an isotropic miniature scalar magnetometer .....	113
4.1.	First results obtained with glassblown cells .....	113
4.1.1.	Results obtained with the $\Phi 10 \times 10$ mm 20 Torr VE cell .....	114
4.1.2.	Results obtained with the $\Phi 5 \times 5$ mm 20 Torr VE cell .....	114
4.1.3.	Results obtained with the $\Phi 5 \times 5$ mm 20 Torr GB cell .....	115
4.1.4.	Results obtained with the $\Phi 5 \times 5$ mm 40 and 50 Torr GB cell .....	116
4.1.5.	Conclusion – VE versus GB cells .....	116
4.2.	Packaging and system architecture of the final demonstrator .....	117
4.3.	Performance of the demonstrator .....	118
4.4.	Perspectives: first steps towards a chip scale helium magnetometer .....	119
4.4.1.	The study on technological solutions for a chip-scale helium magnetometer .....	119
4.4.2.	Microfabricated helium cells.....	122
4.4.3.	Concept of a chip scale helium magnetometer .....	128
4.5.	Conclusion.....	130
	Conclusion.....	134
	Literature .....	136

## List of abbreviations

ASM	Absolute Scalar Magnetometer
CCP	Capacitively Coupled Plasma
CEA	French Alternative Energies and Atomic Energy Commission
CNES	French National Center for Space Studies
CPT	Coherent Population Trapping
DBR	Distributed Bragg Reflector
DFB	Distributed Feedback
DOPT	Optronics Departament of the CEA-LETI
DSIS	Systems and Solutions Integration Departament of the CEA-LETI
EMI	Electromagnetic Interference
ESA	European Space Agency
ESR	Electron Spin Resonance
FLF	Full Larmor Frequency
FM	Frequency Modulation
FM	Frequency Modulation
FWHM	Full Width at Half Maximum
GB	Stands for Precision Glassblowing Inc. – One of the helium cells manufacturers
GRIN	Gradient Index
HF	High Frequency
HLF	Half Larmor Frequency
IM	Intensity Modulation
IM	Intensity Modulation
IPHT	Institute of Photonic Technology, Jena Germany
LC	Liquid Crystal
LETI	Laboratory of Electronics and Information Technology, subsidiary of the CEA
LFA	Local Field Approximation
LNA	Lanthanum Neodymium hexa-Aluminate
LTCC	Low Temperature Co-fired Ceramic
MAC-TFC	MEMS Atomic Clocks for Timing Frequency Control and Communication, FP7 project
MAD	Magnetic Anomaly Detection
MCG	MagnetoCardioGraphy
MEG	MagnetoEncephaloGraphy
MEMS	Micro-Electro-Mechanical System
MSP	Magnetically driven Spin Precession
NIST	National Institute of Standards and Technology, Boulder USA
NMOR	Nonlinear Magneto-Optical Rotation
NMR	Nuclear Magnetic Resonance
OSP	Optically driven Spin Precession



PCB	Printed Circuit Board
PER	Polarization Extinction Ratio
PLZT	Lanthanum-doped lead zirconium titanate
PM	Polarization Maintaining
RF	Radio-Frequency
RIN	Relative Intensity Noise
RMS	Root Mean Square
S/N	Serial Number
SBIR	Small Business Innovation Research, US Government program
SERF	Spin Exchange Relaxation Free
SMSR	Side Mode Suppression Ratio
TRL	Technology Readiness Level
UXO	Unexploded Ordinance
VCO	Voltage Controlled Oscillator
VCSEL	Vertical Cavity Surface Emitting Laser
VE	Stands for Verre Equipements – One of the helium cells manufacturers

## List of symbols

$a_0$	Bohr radius
$Abs$	Absorption
$B$	Magnetic flux density
$C$	Capacitance, $C_{sh}$ – sheath capacitance
$d$	Electrode separation (cell diameter)
$d_s$	Sheath thickness
$E$	Electric field, $\vec{E}_0$ - light polarization axis, $\Delta E$ – energy separation
$e$	Elementary charge
$F$	Frequency
$g_j$	Landé factor
$h$	Planck constant
$j$	Imaginary unit
$k_B$	Boltzmann constant
$k_{mi, el, 1-7}$	Rate coefficients
$L$	Inductance
$LA_{0, 1, 2}$	Resonance signals: continous (0), at Larmor frequency (1) and its double (2)
$l_{opt}$	Effective optical path
$M$	Magnetic moment
$m_{e, He}$	Mass – electron (e) and helium atom (He)
$n_s$	Electron density at sheath edge
$P$	Power, $P_{F, R}$ – forward and reflected power
$p$	Pressure
$Q_{A, B2}$	Cross section, absorbtion (A) and transverse light broadening (B2)
$R$	Resistance
$T$	Temperature, $T_{e, i}$ – electron and ion temperature
$v$	Velocity
$V$	Voltage, $V_B$ – breakdown voltage
$X$	Reactance
$Z$	Impedance
$\gamma$	Gyromagnetic ratio of $^4\text{He}$
$\Gamma$	Torque
$\varepsilon_0$	Vacuum permittivity
$\theta_P$	Angle between the light polarization axis and the ambient magnetic field
$\theta_{RF}$	Angle between the imposed RF magnetic field and the ambient magnetic field
$\Lambda$	Characteristic diffusion length
$\lambda$	Wavelength, $\lambda_i$ – ion mean free path
$\mu_B$	Bohr magnetom
$\mu_{e, i}$	Mobility, electron (e) and ion (i) mobility

## List of symbols

---

$\tau_{l, 2, R}$	Relaxation time – longitudinal (1), transverse (2) and collisional (R)
$\nu$	Collision frequency
$\omega$	Angular frequency

## Introduction

Since the discovery of nuclear magnetic resonance (NMR) by Bloch and Purcell in 1946 high-precision atomic magnetometers have found numerous applications in science and technology. One of their first applications concerns magnetic anomaly detection (MAD) used in military airborne submarine detection systems and geophysical prospecting. As such, they allow the detection of very weak magnetic signals originating from ferromagnetic materials used in submarines or mineral deposits located deep underground. Applications developed up to date also include space exploration, where such sensors help to map the magnetic field of Earth as well as other planets.

The development of high precision magnetic field sensors has been one of the fields of interest of the Laboratory of Electronics and Information Technology (LETI) of the French Alternative Energies and Atomic Energy Commission (CEA<sup>1</sup>) for over 50 years. During that time various magnetometers have been developed. From 1960 to 1990 CEA-LETI designed Nuclear Magnetic Resonance (NMR) Overhauser magnetometers. Those instruments, designed to be placed in orbit, were used in the Oersted (1999) and CHAMP (2000) space missions. Commercial development of LETI's NMR sensors was ensured by SAFARE-CROUZET (now THALES-SAFARE S.A.), which successfully brought NMR-based MAD systems for airborne platforms like helicopters or maritime patrol aircrafts to market. Commercialization in the field of geophysical applications was done by IXSEA.

In order to overcome the limitations on the NMR technology (like gyroscopic effects and low bandwidth), LETI has designed, developed and characterized an Absolute Scalar Magnetometer (ASM) based on Electron Spin Resonance (ESR) of helium-4  $2^3S_1$  metastable state. The isotropy of measurement provided by this sensor is the key feature which distinguishes it from the current state-of-the-art. This isotropic optically pumped sensor (c.f. Fig. 1) uses a non-magnetic piezo-electric motor to set the polarization of the pumping beam at  $90^\circ$  with respect to the ambient magnetic field. The work on the present form of the sensor began at LETI in 2001. Since 2005 its further development was realized under cooperation with the French National Center for Space Studies (CNES) in the course of the SWARM project of the European Space Agency (ESA).

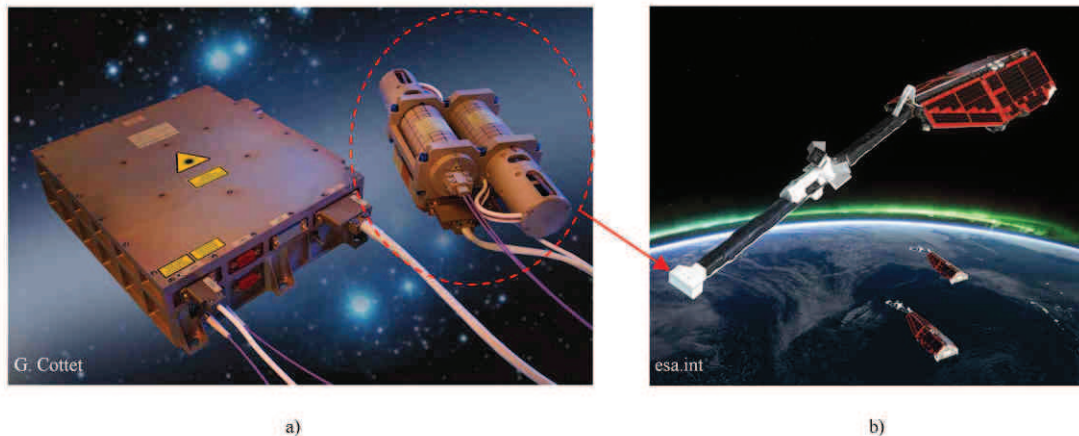


Figure 1. ASM SWARM. a) Sensor head and electronics unit. b) Placement of the sensor at the tip of SWARM's satellite boom.

The device reached the ESA's 8<sup>th</sup> stage of Technology Readiness Level (TRL), which means that it is a complete "flight qualified" ready-to-use system. The technology behind it is sufficiently mature

<sup>1</sup> CEA - Commissariat à l'Energie Atomique et aux énergies alternatives.

for an industrial transfer, although its applications are currently limited to very specialized niche markets.

Benefiting from its large experience in magnetometry and system integration, LETI started a development program (named MiniMag) which aims at the reduction of size of the developed optically pumped isotropic helium-4 magnetometer. Miniaturization (and associated unit cost reduction) is one of the most important steps in addressing a wider spectrum of applications, such as medical imaging, non-destructive testing and magnetic impurity detection. The desired set of specifications for the miniature magnetometer is presented in table 1 as referred to the ASM SWARM performances.

Table 1. Desired set of specifications for a miniature magnetometer, as compared to ASM SWARM characteristics.

SWARM - performance		Miniature sensor - specifications
<b>Sensitivity</b>		1 pT/ $\sqrt{\text{Hz}}$
<b>Accuracy</b>		50 pT
<b>Bandwidth</b>		DC – 100 Hz
<b>Size</b>	<b>Electronics</b>	72x248x300 mm <sup>3</sup>
	<b>Sensor head</b>	460 cm <sup>3</sup>
	<b>Helium cell</b>	32 cm <sup>3</sup>
<b>Power consumption</b>	7 W	< 1 W
<b>Magnetic field dynamic range</b>		20 – 80 $\mu\text{T}$
<b>Isotropy</b>	Full – provided by a piezoelectric motor	Full – technical solution to be identified

Work on miniaturization of atomic magnetometers has been largely inspired by the recent developments made in the field of miniature atomic clocks [1], closely related in principle to atomic magnetometers. For the last ten years, enormous progress has been done in this matter, in particular at the National Institute of Standards and Technology (NIST) in the USA. Thanks to the use of microfabrication technology along with a better understanding of their physics and its scaling laws, sensor heads with characteristic dimensions of less than a centimeter have been obtained [2]. The benefits of technologies originating from the semiconductor industry (MEMS technologies) include not only size reduction but also unit cost reduction due to their compatibility with automated batch processing and packaging. The constructions presented up to date rely on alkali metal vapours (Rb, Cs or K) as the sensitive medium.

Due to their physical principle of operation, all optically pumped magnetometers suffer from anisotropy, which limits their accuracy. It manifests itself as a dependence of the resonance signal amplitude on the orientation of the sensor with respect to the magnetic field direction, with an extreme case of “dead zones” (signal extinction) for certain configurations. Such behavior makes it difficult to

use them in applications where the direction of the field to be measured is unknown, which is in general the case in mobile applications. In order to meet the isotropy/accuracy requirements of mobile and space applications, atomic magnetometers usually rely on various complex architectures, as listed below.

- The use of several separate, orthogonally mounted sensors in order to cover each axis.
- The use of mechanical systems which align the sensor head in a dead zone-free orientation.
- The use of a magnetometer based on Coherent Population Trapping (CPT) with multiple CPT resonances monitored simultaneously [3].
- The use of a servo-mechanism to control the polarization axis of the pumping light. CEA-LETI has successfully realized an isotropic atomic magnetometer, based on a non-magnetic piezoelectric motor driven by a feedback loop in order to set the angle of the linear polarization of the pumping light at  $90^\circ$  with respect to the field to be measured. However, this system is difficult to downscale and it generates micro vibrations (which are difficult to damp on space platforms).

All miniaturized atomic magnetometer constructions reported up to date present problems related with anisotropy, dead zones and heading errors. On the other hand, all state of the art isotropic atomic magnetometer systems are quite bulky and expensive.

The objective of this thesis is to develop a high-performance miniature version of a scalar, isotropic optically pumped helium-4 magnetometer. This Ph.D. thesis is realized as a part of the MiniMag project, supported by the French National Research Agency (ANR) through Carnot funding. The work needs to address several physical and technological challenges, of which the most important are:

- operation of the magnetometer with a miniature helium cell and thus a limited number of metastable atoms,
- identification and characterization of a technological solution that ensures the isotropy of the measurement,
- design of the optical architecture as well as packaging considerations,
- characterization of sensitivity, accuracy and anisotropy of the developed demonstrator.

The developments to be done are summarized in table 2. The solutions used by the SWARM magnetometer are given as a reference.

Table 2. Developments to be done in comparison to ASM SWARM.

	SWARM	MiniMag
<b>Active medium confinement.</b>	Glass-blown helium cell	Miniature glass-blown or a microfabricated glass-silicon-glass structure
<b>Light source</b>	Diode-pumped fiber laser	To be identified
<b>Resonance excitation mechanism</b>	RF magnetic field obtained with coils – magnetically driven spin precession.	All-optical excitation by modulation of the pumping beam or magnetically driven spin precession

Table 2. Continued.

	SWARM	MiniMag
<b>Isotropy-providing polarization control mechanism</b>	Non-magnetic piezoelectric step motor which rotates a linear polarizer	To be identified
<b>Optics assembly</b>	Classical optics	Miniature optics, eventually including gradient-index (GRIN) optics.
<b>Packaging</b>	Dedicated precision mechanics	Dedicated precision mechanics, eventually LTCC <sup>2</sup> packaging.

The first chapter of this thesis describes the operation principle of helium magnetometers and presents the state-of-the-art on miniature atomic magnetometers, with examples of isotropic and anisotropic constructions.

Chapter two deals with the electrical and optical characterization of the discharge ignited inside the cell in order to create  $2^3S_1$  metastable atoms. It presents a numerical model used to predict the behavior of the sensor with respect to the helium cell size reduction and to determine the optimal value of helium pressure in order to maximize the performance of the sensor.

The third chapter presents the architecture of the miniaturized sensor and the path chosen for the downscaling of the basic key elements of the macroscopic sensor.

The last chapter focuses on the developed demonstrator, its construction, performance and possible further miniaturization developments.

<sup>2</sup> Low Temperature Co-fired Ceramic (LTCC) – microsystem packaging technique used in small and medium-scale production.

# Chapter 1: Atomic magnetometers – operating principle and state of the art

---

---

1.1.	Physical principles of helium-4 magnetometers	21
1.1.1.	Optical pumping	23
1.1.2.	Magnetic resonance	23
1.1.3.	Detection of resonance – absorption signals	25
1.1.4.	Isotropy of measurement	27
1.1.5.	Practical realization – the SWARM magnetometer	30
1.2.	State of the art on miniature atomic magnetometers	31
1.2.1.	Optically pumped helium magnetometer – Polatomic Inc.	32
1.2.2.	Coherent population trapping magnetometers	33
1.2.3.	$M_x$ alkali-vapor magnetometers	34
1.2.4.	All-optical Bell-Bloom alkali-vapor magnetometers	36
1.2.5.	Spin Exchange Relaxation-Free (SERF) magnetometers	37
1.2.6.	Summary	39

---

---

## Chapter highlights

- A phenomenological description of the operating principle of a helium-4 atomic magnetometer is presented.
- Main mechanisms leading to heading errors in helium-4 magnetometers are discussed.
- The system architecture of an isotropic helium-4 magnetometer is explained (at the example of the SWARM absolute scalar magnetometer).
- State of the art constructions of miniature atomic magnetometers are described.





## 1. Atomic magnetometers – operating principle and state of the art

The aim of this chapter is to explain the physics which underlays the operation principle of helium atomic magnetometers. The second part of the chapter focuses on the state-of-the-art technological solutions used to obtain miniature atomic magnetometers.

### 1.1. Physical principles of helium-4 magnetometers

This section presents a phenomenological description of the operating principle of atomic magnetometers as applied to the case of a helium-4 magnetometer. It is partially based on the descriptions presented in ref. [4] and [5]. A detailed analytical description, using the density matrix formalism can be found in ref. [5] and [6].

Optically pumped helium-4 magnetometers developed at CEA-LETI use the phenomenon of paramagnetic resonance, induced in helium atoms excited to the  $2^3S_1$  metastable state by means of a weak high frequency (HF) discharge. Their sensitive element comprises high-purity helium contained in a cylindrical glass cell. The HF power is capacitively coupled to the gas with copper electrodes glued on the sides of the cylinder. Figure 2 shows the energy band diagram of helium-4.

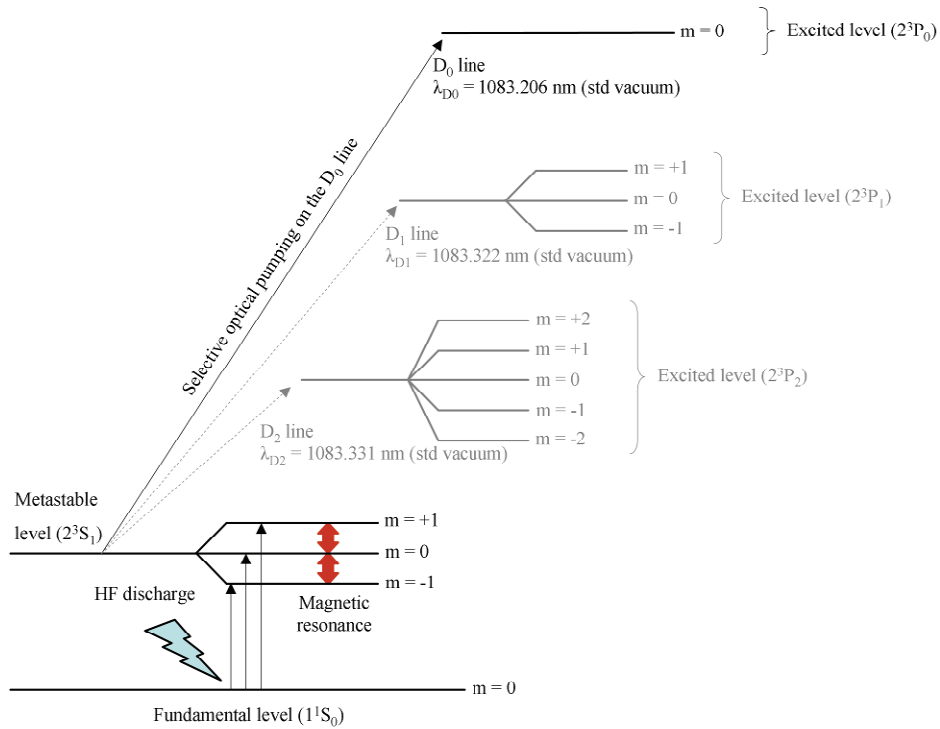


Figure 2. Helium-4 energy band diagram. Not to scale.

The lifetime of a helium-4 atom in the  $2^3S_1$  state is quite long (0.1 up to 1 ms) because of the fact that a radiative transition back to the fundamental state ( $1^1S_0$ ) is forbidden. Thus metastable atoms may be destroyed only by collisions or excitation to other states. Under the influence of an external magnetic field, the  $2^3S_1$  level splits into three Zeeman sublevels which represent the three possible orientations of the electron spin angular momentum (+1, 0, -1). Since helium has no nuclear spin and

therefore no hyperfine structure, the energetic separation of Zeeman sublevels can be expressed as a linear function of the applied magnetic field with Eq. 1.

$$\Delta E = g_j \mu_B B_0 = \frac{\gamma \hbar B_0}{2\pi} \quad (1)$$

Where:  $g_j$  – Landé factor of the metastable state

$\mu_B$  – Bohr magneton

$\gamma$  – gyromagnetic ratio of helium ( $\gamma/2\pi = 28.04$  GHz/T)

$\hbar$  – Planck's constant

$B_0$  – magnetic field

Resonant transitions between Zeeman sublevels are induced by applying a weak RF field which tends to equalize their population. At thermal equilibrium their populations follow the Boltzmann distribution (c.f. Eq. 2)[5], therefore they are almost equally populated. The occurrence of resonance is undetectable.

$$\frac{N_i}{N_j} = \exp\left(\frac{\Delta E}{k_B T}\right) = \exp\left(\frac{5,2 \cdot 10^{-9} \text{ eV}}{2,6 \cdot 10^{-2} \text{ eV}}\right) = 1 - (2 \cdot 10^{-7}) \approx 1 \quad (2)$$

Where:  $N_i, N_j$  – populations of the Zeeman sublevels,

$T$  – temperature – 300 K,

$\Delta E$  – sublevel separation (calculated for  $B_0 = 45$   $\mu$ T),

$k_B$  – Boltzmann constant.

In order to detect the resonance a dissymmetry of populations has to be induced. Selective optical pumping on the  $D_0$  line (c.f. Fig. 2) creates such a dissymmetry by emptying selectively some of the sublevels, which results in the appearance of a non-zero macroscopic magnetic moment and an amplification of the resonance signal.

Helium magnetometers have several advantages over their alkali counterparts. These features are listed below.

- Helium has no nuclear spin (and therefore no hyperfine structure) which results in a linear dependence of the Zeeman splitting with respect to the external magnetic field. The non-linearity due to hyperfine structure is a limiting factor for the accuracy of alkali-vapor magnetometers.
- Metastable ( $2^3S_1$ ) helium species, which are the magnetically-sensitive media, are relatively short-lived ( $10^{-4} - 10^{-3}$  s) which makes the sensor's response quite fast in transient magnetic fields [4].
- Negligible gyroscopic effects due to the high gyromagnetic ratio.
- No need to control the cell temperature.

Miniaturized helium-4 magnetometers could thus be a very competitive alternative to currently developed alkali-vapor based solutions.

The operating principle of the helium-4 magnetometer developed at LETI can be divided into three separate phenomena:

- optical pumping, used to polarize the atoms,
- magnetic resonance induced by the weak oscillating RF field,

- detection of resonance, which in the case of the designed magnetometer is done by observation of the absorption of the pumping light transmitted through the helium cell.

### 1.1.1. Optical pumping

The mechanism of optical pumping was first described by A. Kastler [8]. In the case of the described magnetometer, the cell containing helium-4 atoms in the  $2^3S$  metastable state is irradiated with light at a wavelength corresponding to the  $2^3S_1 \rightarrow 2^3P_0$  transition ( $D_0$  line – c.f. Fig. 2). The probabilities of absorption of the different Zeeman sublevels of the  $2^3S_1$  state obey the quantum selection rules (angular momentum conservation). Since the angular momentum of a photon depends on its polarization ( $m = \pm 1$  for circular and 0 for linear) the quantum selection rules differ for linearly and circularly polarized beams. The absorption probabilities for linearly polarized light have angular dependences presented in table 3.

Table 3. Probabilities of absorption of light by different Zeeman sublevels – linear polarization [5].

<b>m</b>	<b>-1</b>	<b>0</b>	<b>+1</b>
Absorption probability ( $A_m$ )	$\sin^2 \theta_p/2$	$\cos^2 \theta_p$	$\sin^2 \theta_p/2$

The optical pumping depletes diversely the Zeeman sublevels, depending on the optical polarization. The excited  $2^3P_0$  atoms spontaneously decay non-selectively to each of the Zeeman sublevels of the  $2^3S$  metastable state. Thus the optical pumping establishes a macroscopic magnetic polarization of the gas which allows the detection of the resonance signal.

### 1.1.2. Magnetic resonance

A metastable  $^4\text{He}$  atom has a nonzero magnetic moment which is related with its total angular momentum ( $\vec{J}$ ) by Eq. 3.

$$\vec{M}_m = g_J \mu_B \vec{J} = \frac{\gamma \hbar \vec{J}}{2\pi} \quad (3)$$

An external magnetic field exerts a torque on this magnetic moment (eq. 4)

$$\vec{\Gamma} = \vec{M}_m \times \vec{B}_0 = \frac{\gamma \hbar \vec{J}}{2\pi} \times \vec{B}_0 \quad (4)$$

Following the angular momentum theorem, the magnetic moment performs a precession motion (Larmor precession) around  $\vec{B}_0$  (c.f. Fig. 3a). This movement is described by Bloch's equation (c.f. Eq. 5).

$$\frac{d\vec{M}_m}{dt} = \gamma \vec{M}_m \times \vec{B}_0 \quad (5)$$

The principle of measurement of magnetic field with atomic magnetometers is to determine the frequency of this precession which, for the case of helium-4, is linearly dependent on magnetic field (c.f. Eq. 6).

$$f_L = \frac{\gamma}{2\pi} B_0 \quad (6)$$

In order to measure the Larmor frequency  $f_L$  a small RF magnetic field ( $\vec{B}_1$ ) is imposed on the precessing atoms thus subjecting them to a resultant oscillating magnetic field vector  $\vec{B} = \vec{B}_0 + \vec{B}_1$  with:  $\vec{B}_0 \perp \vec{B}_1$ . The best way of presenting this problem is to introduce a reference frame rotating at an angular frequency  $\omega$  (with  $\omega = 2\pi f_L$ ). Such a situation is presented in Fig. 3b.

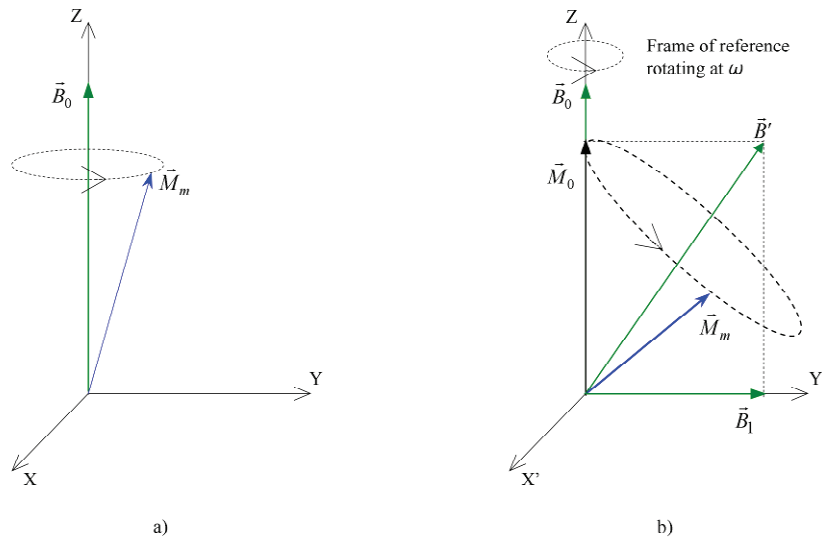


Figure 3. a) Larmor precession. b) Magnetic moment subjected to a constant DC magnetic field  $B_0$  and a rotating RF magnetic field  $B_1$  presented in a frame of reference rotating at an angular frequency  $\omega$  [4].

In the rotating reference frame the resulting magnetic field influencing the movement of the magnetic moment is  $\vec{B}' = (B_0 - \omega / \gamma) \hat{u}_z + B_1 \hat{u}_{Y'}$  (with  $\hat{u}_{x,y,z}$  - unit vector and  $\hat{u}_{x',y',z'}$  - unit vector in the rotating frame of reference). Therefore the Bloch's equation describing the movement of the magnetic moment takes the form of eq. 7.

$$\frac{d\vec{M}_m'}{dt} = \gamma \vec{M}_m' \times \vec{B}' \quad (7)$$

Taking relaxation processes into account and assuming  $\vec{M}_0 \parallel \vec{B}_0$ , the solution of this equation provides the three components of the magnetic moment, expressed in the rotating system of coordinates ( $\hat{u}_{x'}$ ,  $\hat{u}_{Y'}$ , and  $\hat{u}_{z'} = \hat{u}_z$ ) [4] (eq. 8).

$$M'_x = -M_0 \frac{\gamma B_1 T_2}{1 + (\Delta\omega T_2)^2 + (\gamma B_1)^2 T_1 T_2}$$

$$M'_y = M_0 \frac{\Delta\omega\gamma B_1 T_2^2}{1 + (\Delta\omega T_2)^2 + (\gamma B_1)^2 T_1 T_2} \quad (8)$$

$$M'_z = M_0 \frac{1 + (\Delta\omega T_2)^2}{1 + (\Delta\omega T_2)^2 + (\gamma B_1)^2 T_1 T_2}$$

Where:  $M'_x$  and  $M'_y$  – transverse components of the magnetic moment in the rotating reference frame,  
 $M_z$  – longitudinal component of the magnetic moment,  
 $M_0$  – stationary value of the magnetic moment,  
 $\Delta\omega$  – detuning of the RF signal from Larmor frequency ( $\Delta\omega = \omega_L - \omega$ ),  
 $T_1, T_2$  – longitudinal and transversal relaxation time constants.

By going back to the laboratory reference frame, a set of equations describing the transverse (perpendicular to  $\vec{B}_0$ ) evolution of the magnetic moment can be obtained (cf. Eq. 9).

$$M_x = M'_x \cos(\omega t) - M'_y \sin(\omega t) \quad (9)$$

$$M_y = M'_x \sin(\omega t) + M'_y \cos(\omega t)$$

The longitudinal component in the laboratory reference frame takes the same form as in the rotating frame (c.f. Eq. 10)

$$M_z = M'_z \quad (10)$$

At resonance (i.e. when  $\Delta\omega = 0$ ), the y component ( $M'_y$ ) disappears, thus the magnetic moment precesses in-quadrature to the oscillating field  $\vec{B}_1 = B_1 \hat{u}_y$ , ( $90^\circ$  phase shift between  $\vec{M}'$  and  $B_1 \hat{u}_y$ ).

### 1.1.3. Detection of resonance – absorption signals

Once the imposed RF magnetic field frequency matches Larmor frequency (resonance condition) the atomic system enters resonance. At resonance the opacity of helium changes and additional optical absorption appears on the pumping light because the sublevels susceptible of absorbing the pumping light are repopulated. Therefore resonance can be monitored by observation of the optical power ( $P_T(t)$ ) transmitted through the helium cell [9]. At resonance, the voltage on the photodetector can be described by Eq. 11.

$$V_d(t) \propto P_T(t) [1 - LA_0(t) - LA_1(t) - LA_2(t)] \quad (11)$$

Where:  $LA_0$  – continuous (mean) part of the absorption signal,  
 $LA_1$  and  $LA_2$  – modulations of absorption at  $\omega_L$  and  $2\omega_L$  respectively.

#### 1.1.3.1. Longitudinal detection mode – $LA_0$ signal

$LA_0$  is the continuous absorption signal (null frequency). It reflects the evolution of the populations of the Zeeman sublevels.

The use of  $LA_0$  as a detection signal is not possible directly, since the signal is symmetric and reaches a maximum value at resonance. In order to make it anti-symmetric a low frequency modulation ( $\omega_{\text{mod}}$ ) is imposed on the RF magnetic signal (fig. 4a).

This way the response of the system at  $\omega_{\text{mod}}$  is anti-symmetric (fig. 4b) and passes through zero at resonance. Such a signal can be used as a command for a voltage controlled oscillator (VCO), generally used as a source of the RF signal.

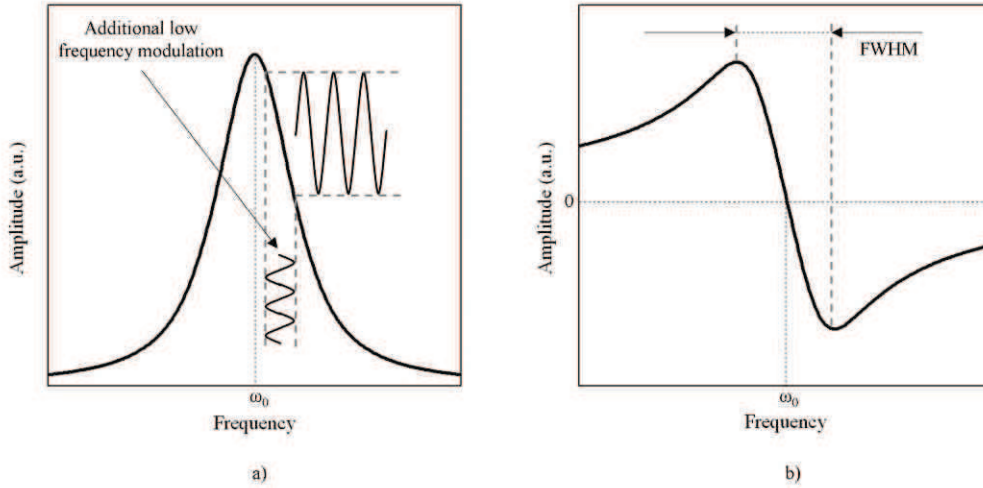


Figure 4. a)  $LA_0$  signal and the low frequency modulation of the RF magnetic field. b) Resulting anti-symmetric signal.

### 1.1.3.2. Transverse detection modes – $LA_1$ and $LA_2$ signals

$LA_1$  and  $LA_2$  are alternating signals at  $\omega_L$  and  $2\omega_L$  respectively. They may be decomposed into in-phase and in-quadrature components by means of phase sensitive detection (c.f. Fig 5 and 6). These two signals show the evolution of coherences of the atomic system. The two antisymmetric components ( $LA_1$  in-phase and  $LA_2$  in-quadrature) can be used to lock the VCO frequency at the Larmor frequency ( $\omega_L$ ).

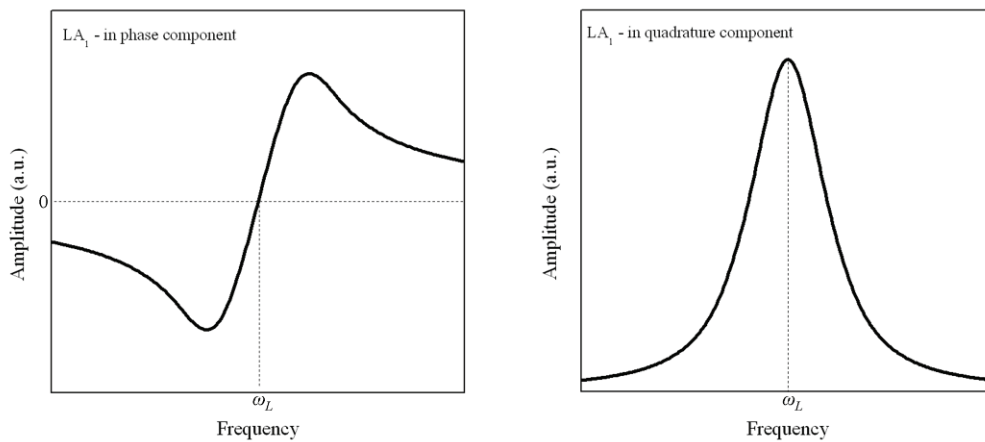


Figure 5. The lineshapes of in-phase and in-quadrature components of the  $LA_1$  signal.

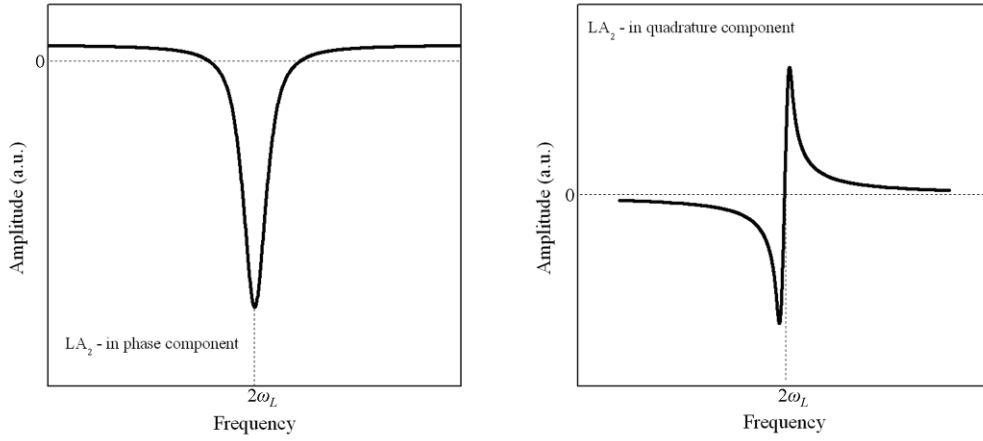


Figure 6. lineshapes of in-phase and in-quadrature components of the  $LA_2$  signal.

### 1.1.4. Isotropy of measurement

By construction all atomic magnetometers suffer from isotropy related problems. In general, their physical principle of operation imposes the fact that their sensitivity depends on the angular relationship between the sensor and the measured magnetic field. Helium magnetometers are not an exception. This section describes several sources of their anisotropy and solutions which allow to minimize their influence on the accuracy of the designed magnetometer. The vector convention used throughout the thesis is presented in Fig. 7.

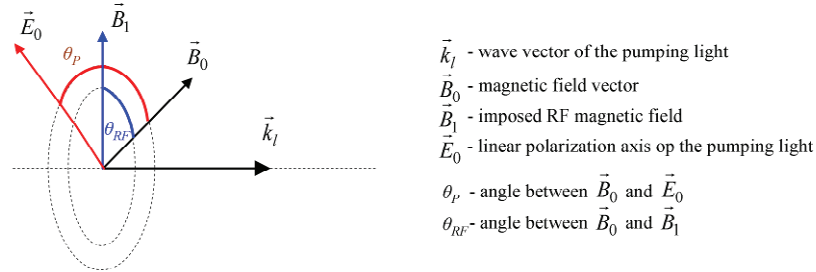


Figure 7. The vector convention used throughout the thesis. The angle between  $\vec{k}_l$  and  $\vec{B}_0$  is arbitrary.

#### 1.1.4.1. Anisotropy induced by the pumping light

A slight detuning of wavelength of the pumping light from the center of the absorption line degrades significantly the sensors parameters. Apart from increasing the resonance linewidth and signal amplitude, it introduces additional error to the measurement due to a shift in the energy splitting of the Zeeman sublevels. This error originates from two phenomena: real and virtual light shifts.



#### 1.1.4.1.1. Real light shifts

Real light shifts are caused by coherence transfer from optically excited states. It is a factor which limits the accuracy at high values of helium pressure due to P-level mixing [4]. In  $^4\text{He}$ , this shift can be completely suppressed by applying optical pumping on the  $D_0$  line, instead of  $D_1$  and  $D_2$  (c.f. Fig. 2).

#### 1.1.4.1.2. Virtual light shifts

A small deviation of wavelength of the pumping light from the absorption line center results in a slight displacement of the energy of the Zeeman sublevels which changes the frequency of the transitions. This energy shift has the same angular dependence on the  $\theta_p$  angle as the absorption probabilities for each Zeeman sublevel [5] [10] (c.f. table 3 and Eq. 12).

$$\Delta E_m = A_m \Delta E' \propto A_m \Delta \nu I_l \quad (12)$$

Where:  $A_m$  – absorption probability (c.f. table 3),  
 $\Delta \nu$  – wavelength detuning of the laser,  
 $I_l$  – Intensity of the laser beam.

This situation is schematically presented in Fig. 8.

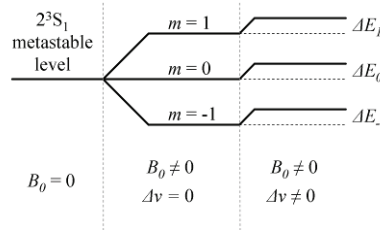


Figure 8. Shift of Zeeman energy levels of the triplet metastable state. Not to scale.

The application of linearly polarized light suppresses the influence of virtual shift on the resonance frequency since sublevels  $m = \pm 1$ , which are equally populated, exhibit the same energy shift [10].

#### 1.1.4.2. Anisotropy related with the driving field ( $B_1$ ) – the Bloch-Siegert shift

Magnetic resonance is driven by the component of  $\vec{B}_1$ , which is perpendicular to  $\vec{B}_0$ . The influence of this linear driving field on the measurement of  $\vec{B}_0$  is known as the Bloch-Siegert shift, which imposes an error on the measurement of magnetic field. The shift in resonance frequency can be expressed by Eq. 13 [5].

$$\Delta f = \frac{\gamma}{2\pi} \frac{B_{1\perp 0}^2}{4B_0} \quad (13)$$

Where:  $\vec{B}_{1\perp 0}$  - component of  $\vec{B}_1$  which is perpendicular to  $\vec{B}_0$ .

For a constant value of  $\vec{B}_0$ , the error introduced by the Bloch-Siegert shift depends on  $\theta_{RF}$  thus it introduces anisotropy to the measurement. The only solution to obtain an isotropic measurement in

this situation is to maintain a constant value of  $\theta_{RF}$ . This angle is fixed at  $90^\circ$ , since only the part of  $\vec{B}_1$  perpendicular to  $\vec{B}_0$  induces resonance.

In such a configuration, the maximal value of error introduced by the Bloch-Siegert shift for  $B_I = 0.1 \mu\text{T}$  and  $B_0 = 46 \mu\text{T}$  is around 54 pT. This value is greater than the desired accuracy specification (c.f. table 1). Since the Bloch-Siegert shift has a constant value (for a fixed  $\theta_{RF}$ ) it may be corrected using a postprocessing algorithm [11].

#### 1.1.4.3. Resonance signal amplitude anisotropy

Signal amplitude anisotropy is common to all optically pumped atomic magnetometers. It is caused by two phenomena.

First of which is the angular dependence of the probability of transition between sublevels of interest. In the case of the designed helium-4 magnetometer, which uses the mechanism of magnetically driven spin precession (resonance induced by RF magnetic field) and linearly polarized pumping light, this means a dead zone for  $\theta_P \approx 55^\circ$ . This is caused by the fact that transition probabilities (c.f. table 3) become the same for all three Zeeman sublevels therefore pumping does not redistribute their populations and therefore no resonance signal amplification occurs.

The second mechanism is related with the detection method used. In the discussed case, resonance is observed in the pumping light transmitted through the cell. The angular characteristics of the three resonance signals detected this way are presented in Fig. 9.

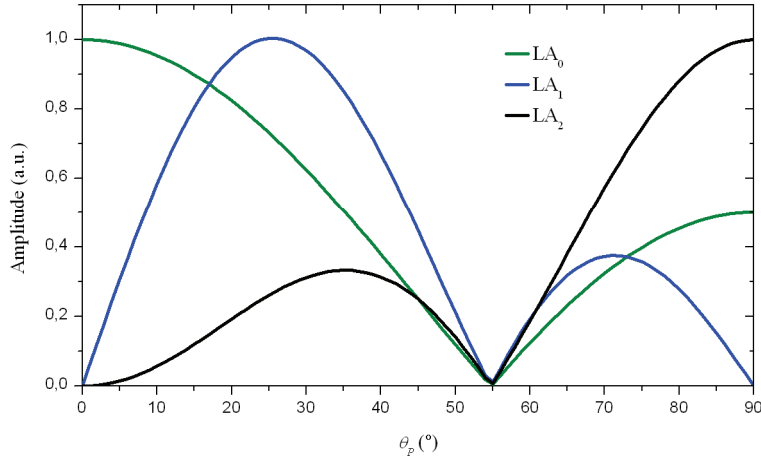


Figure 9. Angular characteristics of the designed helium magnetometer.

The solution developed at LETI, allowing an isotropic measurement, consists of fixing this angle at  $90^\circ$ . In the SWARM project, this is done with a servo-driven piezoelectric motor which fixes the transmission axis of a linear polarizer at  $\theta_P = 90^\circ$  and the RF saddle coil to obtain  $\theta_{RF} = 90^\circ$ . The servomechanism uses  $LA_1$  as error signal to adjust the position.

#### 1.1.4.4. Mechanical design

The influence of the materials used in the construction of the sensor head is of dual nature. All materials have a remanent and an induced magnetization. Both should be reduced to an absolute minimum since they influence the measurement.

The magnetic field related with the remanent magnetization of the sensor head materials is superimposed on the measured value ( $B_0$ ). What is more, the superposition depends on the angle between the sensor and  $\vec{B}_0$  therefore it is a source of anisotropy. Remanent magnetization can be significantly reduced by selecting non-ferromagnetic materials (diamagnetic or paramagnetic). Additional attention should be paid to machining processes to which the elements of the sensor head are subjected. Some tools (e.g. drills or polishing disks) may leave a ferromagnetic residue on the samples (e.g. cobalt or iron).

The induced magnetization of the materials is related with their magnetic susceptibility and the external magnetic field. Every mechanical design which differs from a perfectly spherical geometry (which in practice is impossible to realize) is subject to introduce heading errors to the measurement. These problems are generally addressed by the use materials with very low magnetic susceptibility (e.g. PEEK) and the use of cylindrical geometry, which is much easier to realize in practice.

The problems described above can never be resolved perfectly. They can be minimized to some extent but the sensor head will always have some residual magnetic signature. However this signature can be measured and subtracted from the actual measurement [11].

#### 1.1.5. Practical realization – the SWARM magnetometer

A block diagram of a practical realization of a helium magnetometer, based on the above description is presented in Fig. 10.

The discharge is ignited inside the helium cell by a capacitively coupled HF signal. A Voltage Controlled Oscillator (VCO) provides the RF signal to a saddle coil wrapped around the cell. The RF magnetic field induces resonant transitions between the Zeeman sublevels. The VCO is driven by the resulting absorption signal ( $LA_0$  or  $LA_2$  signals).

Isotropy is provided by a servo-driven piezoelectric motor which fixes the polarization axis of the pumping light ( $\theta_p$ ) and the direction of the RF magnetic field ( $\theta_{RF}$ ) at right angle with the ambient magnetic field.  $LA_1$  is used as error signal for the servomechanism (this signal is null at  $\theta_p = 90^\circ$  - c.f. Fig. 9). The angle between  $\vec{B}_1$  and  $\vec{E}_0$  is fixed at  $0^\circ$  by construction, so as to maintain  $\theta_{RF}$  at  $90^\circ$ .

The SWARM magnetometer provides absolute scalar magnetic field measurements with a  $1 \text{ pT}/\sqrt{\text{Hz}}$  resolution over a bandwidth from DC to 100 Hz. An in-depth theoretical and experimental analysis of the various factors affecting the magnetometer accuracy (like residual magnetism and Bloch-Siegert shift) made it possible to create a correction algorithm [11]. The correction allows for an overall precision better than 45 pT ( $1 \sigma$ ).

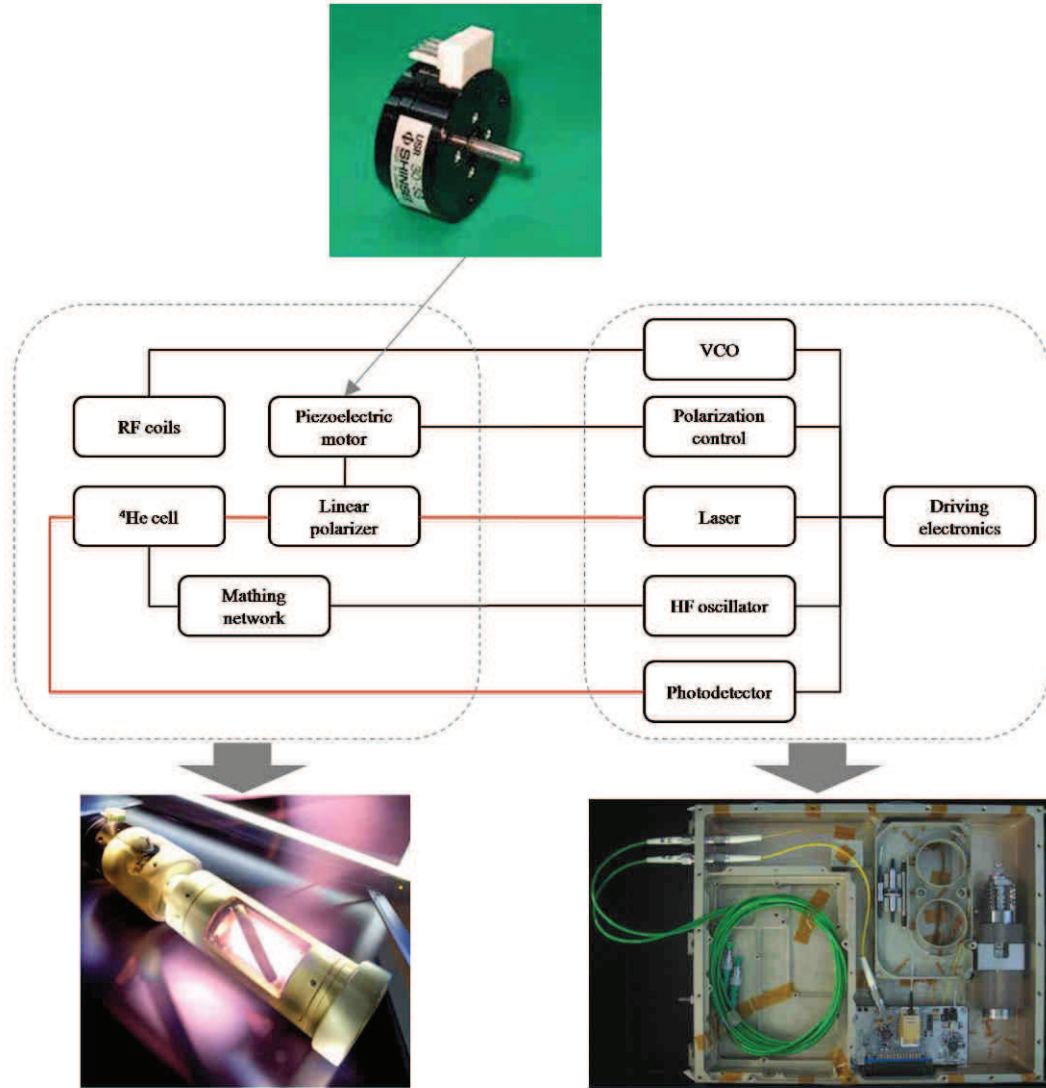


Figure 10. Block diagram presenting the operating principle of the SWARM magnetometer developed at LETI.

## 1.2. State of the art on miniature atomic magnetometers

The reduction of size of atomic magnetometers opens a new broad range of applications which can benefit from their high sensitivity. There is a constantly rising scientific interest in the physical and technological aspects of their construction. Figure 11 presents the number of papers published in the field of atomic magnetometry per year.

A large increase of interest seems to start around the year 2000 which can be explained by the beginning of work on their miniaturization at the NIST institute, a leading research and development organization in the field.

This section will present the most recent achievements reported up to date with a particular focus on miniaturized sensors. Present state of the art is largely dominated by constructions based on alkali-vapours. Their technology exhibits a much faster scaling-down trend. Several research groups worldwide employ intensive scientific and technological efforts in order to obtain compact versions of such sensors. Their large development benefits from previous interest in miniaturized atomic clocks

and frequency references because all their key elements, like lasers and physics packages, are the same.

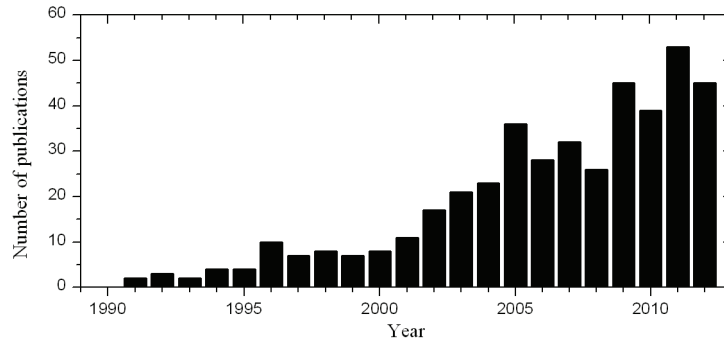


Figure 11. Number of publications per year in the domain of atomic magnetometry. Data collected with SciVerse Scopus database.

In order to allow a better understanding of the state of the art, it is important to introduce a short classification of atomic magnetometers. These sensors generally use circularly polarized light. Based on the resonance excitation and detection scheme used in their construction, we can distinguish three types of sensors.

- *$M_x/M_z$  magnetometers*

These sensors use a RF magnetic field, introduced by a coil system, to induce resonance in the atomic media (magnetically driven spin precession). The detection can be done by observing the longitudinal ( $M_z$ ) or transverse ( $M_x$ ) component of the magnetic moment.  $M_z$  magnetometers have an equatorial dead-zone, while those using the  $M_x$  signal have both polar and equatorial dead zones.

- *Bell-Bloom magnetometers*

In the Bell-Bloom regime the resonance is induced by modulating the intensity (IM), frequency (FM) or polarisation of the pumping beam (optically driven spin precession). Therefore there is no RF magnetic field applied. These sensors suffer from a polar dead-zone.

- *CPT magnetometers*

This class of sensors uses an indirect measurement of the Larmor frequency by measuring the energy separation of two magnetically sensitive hyperfine states and referencing them to a magnetically insensitive state. By using multiple CPT resonances an isotropic measurement can be provided. These sensors use complex control electronics and data processing units.

Those three types of sensors have their advantages and drawbacks, which make them more or less convenient for use in specific applications.

### 1.2.1. Optically pumped helium magnetometer – Polatomic Inc.

Since the first magnetometer of this type was presented in 1961 [12], not much progress towards its miniaturization has been reported. The smallest construction presented up to date was developed by Polatomic Inc. [13]. It comprises a 6 cm<sup>3</sup> glass-blown helium cell filled to 1.5 Torr of pure <sup>4</sup>He, thus forming a sensor head 6x6x12 cm<sup>3</sup> large. Its relatively small size results mainly from the development

of a new light source used for pumping: the classically used helium discharge lamp was replaced with an InGaAs diode laser. Both constructions are presented in Fig. 12a.

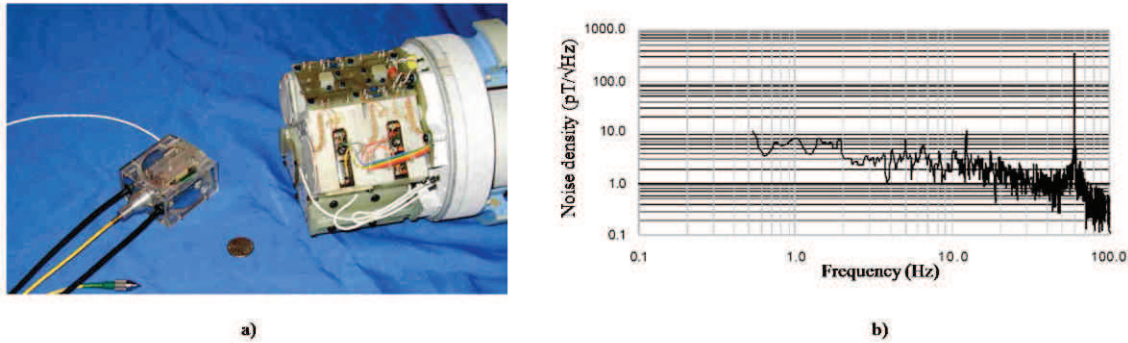


Figure 12. a) Compact version of a helium magnetometer developed by Polatomic Inc. As compared to a lamp-pumped sensor [13]. b) Noise spectral density of the miniature version [14].

Light emitted by a helium lamp contains  $D_0$ ,  $D_1$  and  $D_2$  lines. Since the  $D_2$  line polarizes the atoms in opposite direction than  $D_0$  and  $D_1$  lines, the pumping is less efficient. The finesse of light emitted by a laser allows a selective pumping on the  $D_0$  line which in terms allows to miniaturize the helium cell while maintaining the overall sensor performance. A smaller cell allows to use smaller optics. What is more, a pigtailed diode laser can be separated from the sensor head by an optical fiber. All these aspects influence the final sensor's dimensions, making it smaller. The sensor reaches a sensitivity below  $10 \text{ pT}/\sqrt{\text{Hz}}$  under earth's field operation (c.f. Fig. 12b). The magnetometer operates in the Bell-Bloom regime.

### 1.2.2. Coherent population trapping magnetometers

CPT magnetometers use a pump beam which is frequency modulated (FM) in the microwave range. Resonance occurs when the frequency separation of the 1<sup>st</sup> order sidebands, resulting from FM, matches the field-dependant hyperfine structure energy levels. At resonance the normally opaque alkali media become transparent because they cannot absorb more radiation. By the use of multiple hyperfine levels (multiple resonances), the measurement becomes isotropic [2]. Two compact constructions of this type have been reported in literature.

#### 1.2.2.1. A compact CPT magnetometer for space applications – TU Graz [15]

Scientists from the Technical University of Graz, reported a CPT sensor based on a glassblown rubidium cell (c.f. Fig. 13a). The device is dedicated for space applications.

The dimensions of the assembled sensor head are: 5 cm in diameter and 7 cm of length. The sensor reached  $70 \text{ pT}/\sqrt{\text{Hz}}$  (c.f. Fig 13b) in the frequency range of 0.1 - 3 Hz. It provides an isotropic measurement with a dynamic range up to 1 mT. Its alkali-vapor cell has a volume of  $1 \text{ cm}^3$ .



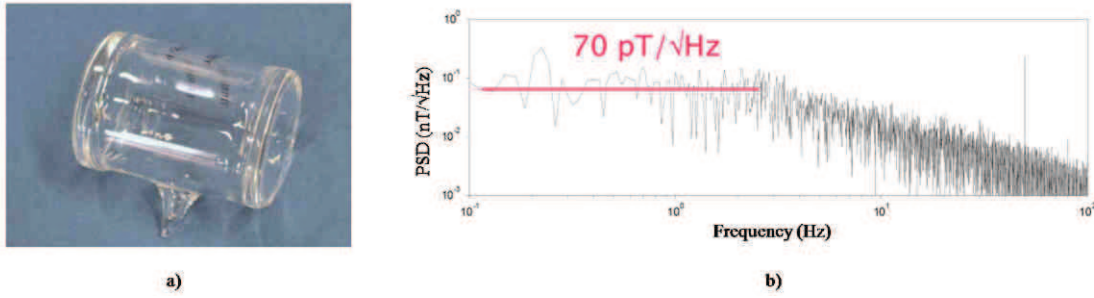


Figure 13. a) Alkali-vapour cell of the presented magnetometer [15], b) Sensitivity of the presented magnetometer [15].

#### 1.2.2.2. A microfabricated CPT magnetometer – NIST [3]

NIST institute reported a sensor of the CPT type made using microfabrication techniques (fig. 14a). In fact, at first, the whole construction was designed to be an atomic clock.

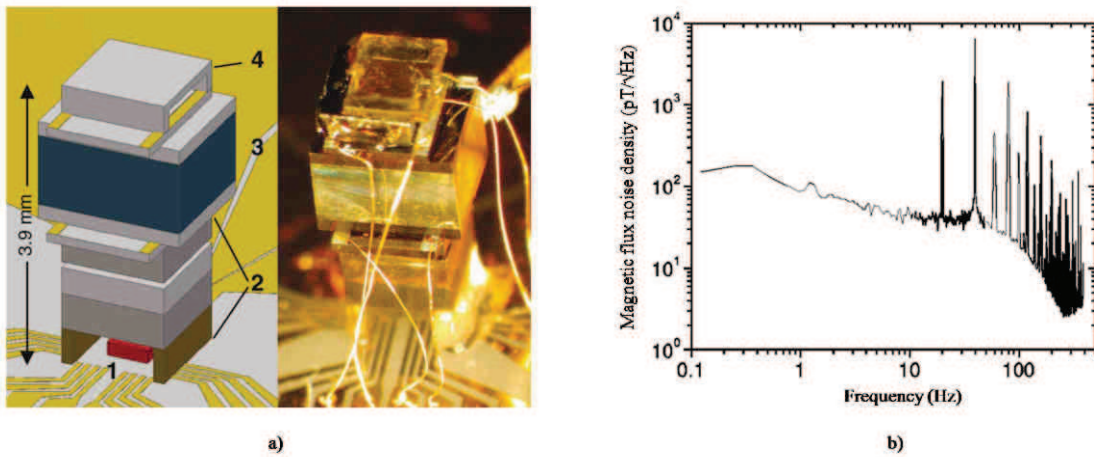


Figure 14. a) Structure of the NIST's CPT magnetometer [3]. b) Noise density of the presented magnetometer [3].

The sensor consists of a VCSEL laser (1), an optics package (2), a glass-silicon-glass rubidium cell (3) and a photodiode (4) stacked together to form a 3.9 mm high structure. By changing the excitation frequency to address magnetically sensitive hyperfine levels and applying specific signal processing a magnetometer was obtained with similar characteristics to the previously described (fig. 14b), although much smaller in size. The sensor occupies a volume of  $12 \text{ mm}^3$ . It reaches a sensitivity of  $50 \text{ pT}/\sqrt{\text{Hz}}$  in the frequency range of 10 - 50 Hz. Its cell volume is  $1 \text{ mm}^3$ .

#### 1.2.3. $M_x$ alkali-vapor magnetometers

The operating principle of  $M_x$  magnetometers imposes anisotropy on the measurement.  $M_x$  magnetometers have generally higher sensitivity than CPT sensors. They are also generally simpler to implement in practice.

### 1.2.3.1. A microfabricated $M_x$ magnetometer – NIST [16]

This  $M_x$ -type magnetometer is also made using microfabrication technologies. Its construction is presented in Fig. 15a.

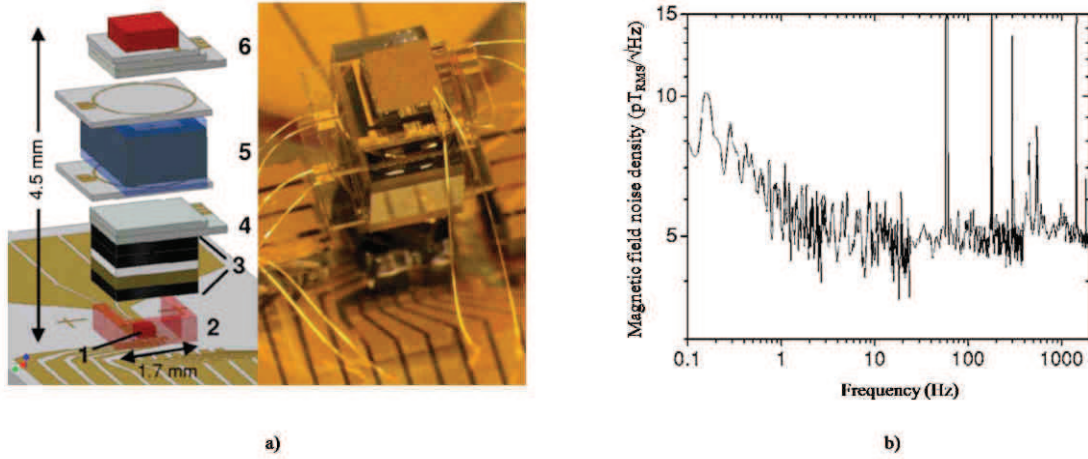


Figure 15. a) Structure of the NIST's  $M_x$  magnetometer [16]. b) Noise density of the presented magnetometer [16].

It is also composed of several microfabricated parts stacked on top of each other: a VCSEL laser (1); a polyimide spacer (2); optics package (3); Indium tin oxide heater (4); glass-silicon-glass rubidium cell (5); heater and photodiode assembly (6). The sensor reached a sensitivity of 5 pT/√Hz in the frequency range of 1-100 Hz (c.f. Fig. 15b).

### 1.2.3.2. Miniature atomic magnetometer sensor array – IPHT [17]

An array consisting of four cesium cells was presented by IPHT. The volume of individual cells is 50 mm<sup>3</sup>. The structure (c.f. Fig. 16a) consists of a glass-silicon-glass cesium cell sandwiched between two PCB's (PCB). The assembly also allows  $M_x$ -type operation by the use of coils on the two PCB boards ( $B_1$ ). The vapor cells are heated on the sides by a laser beam provided by two optical fibers (F). Only two out of four cells were used (R and M).

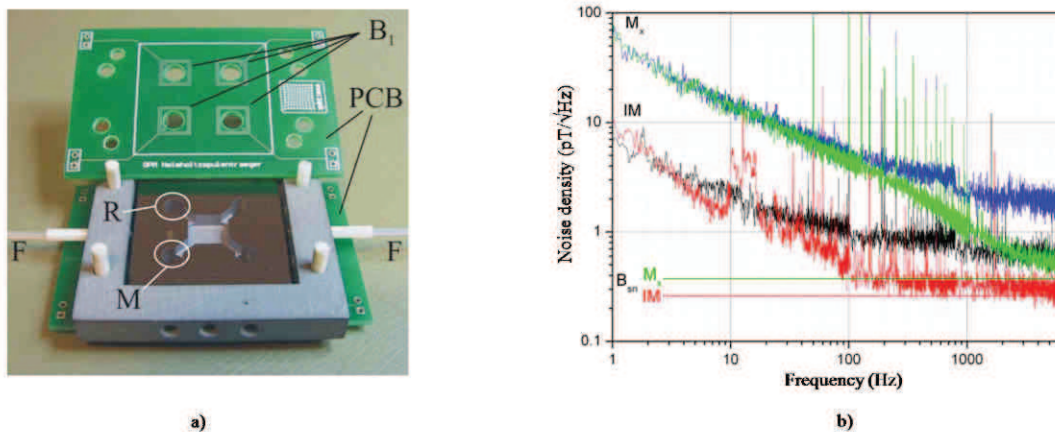


Figure 16. a) Sensor developed at IPHT [17]. b) Comparison between  $M_x$  and Bell-Bloom IM type operation [17]. Red and green traces illustrate a gradiometer mode – subtraction of signals obtained with both cells.



The sensor was operated in the  $M_x$  and Bell-Bloom modes. The noise density obtained with both configurations is presented in Fig. 16b. For frequencies below 100 Hz the noise of the IM magnetometer in Fig. 16b is dominated by  $1/f$  noise. In the  $M_x$  magnetometer configuration the  $1/f$  noise dominates the complete spectrum up to several kHz.

#### 1.2.4. All-optical Bell-Bloom alkali-vapor magnetometers

Bell-bloom type magnetometers have different angular characteristics of the resonance signal amplitude as compared to  $M_x$ -type sensors. Such magnetometers experience only one, polar dead zone, contrary to  $M_x$  magnetometers which have polar and equatorial dead zones.

There is a particular interest in developing such magnetometers when it comes to array operation, since  $M_x$  magnetometers, which use RF magnetic field to induce resonance, can suffer from crosstalk problems.

##### 1.2.4.1. A microfabricated Bell-Bloom magnetometer, using frequency modulation – NIST [18]

In this configuration the resonances are induced optically by means of a frequency modulated pump beam (Bell-Bloom configuration). The structure of the sensor is presented in Fig. 17a.

The construction comprises a microfabricated  $^{87}\text{Rb}$ -filled glass-silicon-glass cell suspended on polyimide tethers. The heating laser is collimated on the side of the structure. The probing signal is collected by an optical fiber and sent to a photodiode which is separated from the sensor head.

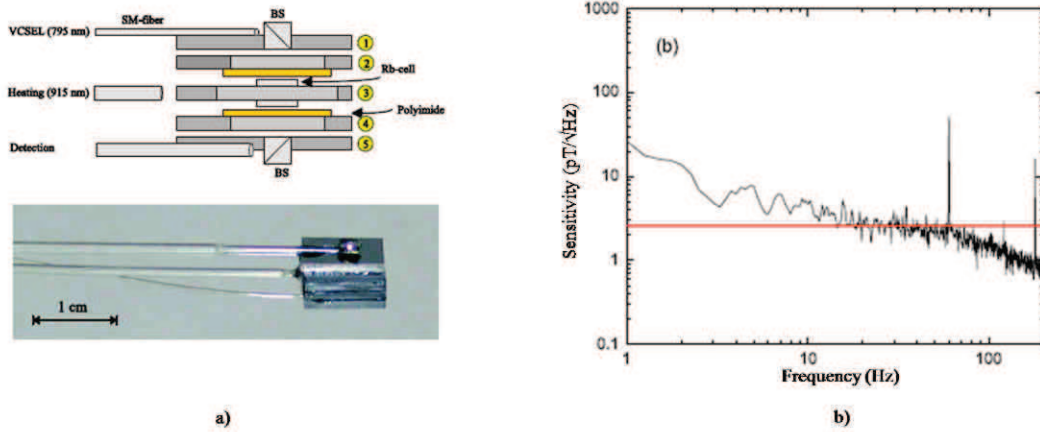


Figure 17. All optical alkali-vapour atomic magnetometer presented by NIST [18]. a) Structure. b) Noise density of the presented magnetometer [18].

The sensor was operated at an ambient magnetic field of  $7 \mu\text{T}$  and reached a sensitivity of  $2.7 \text{ pT}/\sqrt{\text{Hz}}$  in the frequency range [20 Hz; 60 Hz] (c.f. Fig. 17b). Noise level increases for lower frequencies and reaches  $25 \text{ pT}/\sqrt{\text{Hz}}$  at 1 Hz.

##### 1.2.4.2. A microfabricated Bell-Bloom magnetometer array using intensity modulation – IPHT [19]

This construction is also a microfabricated Bell-Bloom type magnetometer although operating with intensity modulation of the probe beam instead of frequency modulation. It uses an array of four glass-

silicon-glass caesium cells, similar to the one presented in 1.2.3.2. Its cell structure is presented in Fig. 18a.

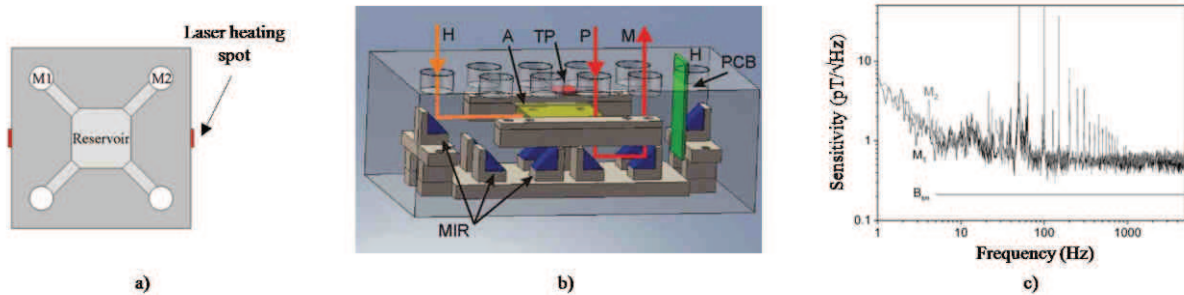


Figure 18. Miniature alkali-vapour magnetometer sensor array presented by IPHT [19]. a) Cell structure. b) Optical assembly. c) Noise density of the presented magnetometer.

The sensor array (c.f. Fig. 18a) consists of a central caesium reservoir which, heated from both sides, provides alkali vapours to adjacent cells (M1,M2...). This structure is used inside an optics mount (c.f. Fig. 18b), containing mirrors (MIR) to direct the pump (P) and heating (H) beams. Temperature is controlled by a sensor (TP) connected to an electronic circuit (PCB). The magnetometer is operated in an ambient field of 50  $\mu\text{T}$  and reaches a sensitivity of 500  $\text{fT}/\sqrt{\text{Hz}}$  for frequencies above 50 Hz (c.f. Fig. 18c) and 6  $\text{pT}/\sqrt{\text{Hz}}$  at 1 Hz.

### 1.2.5. Spin Exchange Relaxation-Free (SERF) magnetometers

The SERF magnetometer, developed for the first time at Princeton University, benefits from the fact that at very high alkali vapor densities (and thus high temperatures) and near-zero ambient magnetic fields, the spin relaxation due to collisions between excited alkali atoms is largely suppressed. By the use of this effect, sensitivities can be lowered by nearly three orders of magnitude, down to 1-10  $\text{fT}/\sqrt{\text{Hz}}$ . Highly sensitive SERF-based sensors can only be operated inside passive magnetic shields. Unshielded SERF magnetometers, using Helmholtz coils to cancel out the external field, were reported [20]. Nevertheless their sensitivity is significantly degraded (1-10  $\text{pT}/\sqrt{\text{Hz}}$ ) due to ambient magnetic noise and field gradients.

In general SERF magnetometers are excluded from mobile applications that require the sensor to operate in the Earth's magnetic field. This class of sensors is widely used in medical applications, to record very weak bio-magnetic fields (MagnetoEncephaloGraphy MEG and MagnetoCardioGraphy MCG).

Since this thesis is dedicated to the realization of an Earth's-field magnetometer, a complete state of the art on SERF magnetometers is beyond its scope. However two miniature SERF-based constructions will be presented here since all the building blocks of SERF and non-SERF magnetometers are basically the same. Both of which are low-field magnetometers. No miniaturized Earth's-field SERF-based magnetometers (using coils to cancel out the external field) have been reported up to date.

### 1.2.5.1. A SERF magnetometer using polarization rotation detection- University of Wisconsin Madison [21]

This construction, presented by the group of Walker et al. at the University of Wisconsin-Madison [21] uses a  $1 \times 1 \times 5 \text{ cm}^3$  rectangular vapor cell filled with  $^{87}\text{Rb}$ . The assembled sensor is presented in Fig. 19a.

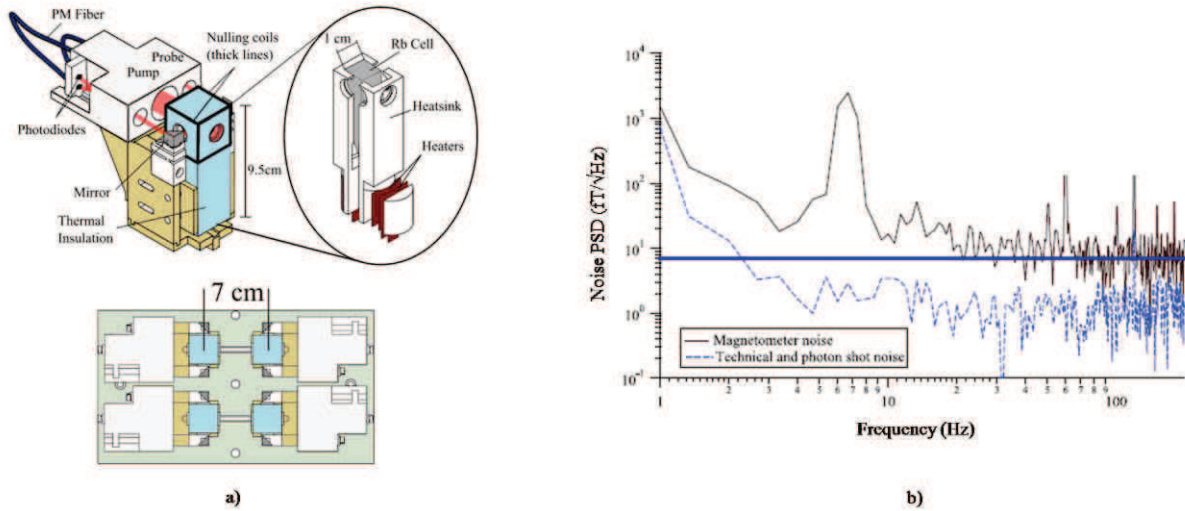


Figure 19. Sensor developed at the University of Wisconsin-Madison [21]. a) Sensor head and four-sensor array arrangement. b) Noise density of the presented magnetometer.

The magnetometer uses an orthogonal pump-probe beam arrangement. The probe beam is linearly polarized; its polarization rotation (Nonlinear Magneto-Optic Rotation - NMOR) is detected as a measure of the magnetic field. It is designed in order to allow array operation (c.f. Fig. 19a) for medical use. In near-zero magnetic field and for frequencies above 20 Hz the sensor reaches  $6 \text{ fT}/\sqrt{\text{Hz}}$  sensitivity (c.f. Fig. 19b).

### 1.2.5.2. A SERF magnetometer using absorption detection – NIST [2]

The most advanced construction of a miniature atomic magnetometer presented by the NIST institute [2] is shown in Fig. 20a. It consists of a microfabricated Glass-Silicon-Glass cell filled with  $^{87}\text{Rb}$  (C in Fig. 20a). Light absorbing filters are glued on the optical aperture of the cell (F). This structure is enclosed in a vacuum package (VAC) and suspended on polyimide threads (S) which limit conductive heat loss. The probe light is provided by a polarization-maintaining fiber (PM), collimated by a lens (L1) and reflected by a reflecting prism (P). A quarter-wave plate (QWP) is used to produce a circularly polarized beam. The absorption signal is reflected by a dichroic mirror and detected by a photodiode (PD). Another laser beam, used for heating, is supplied by a multimode fiber (MM) it is absorbed by the filters thus heating the cell.

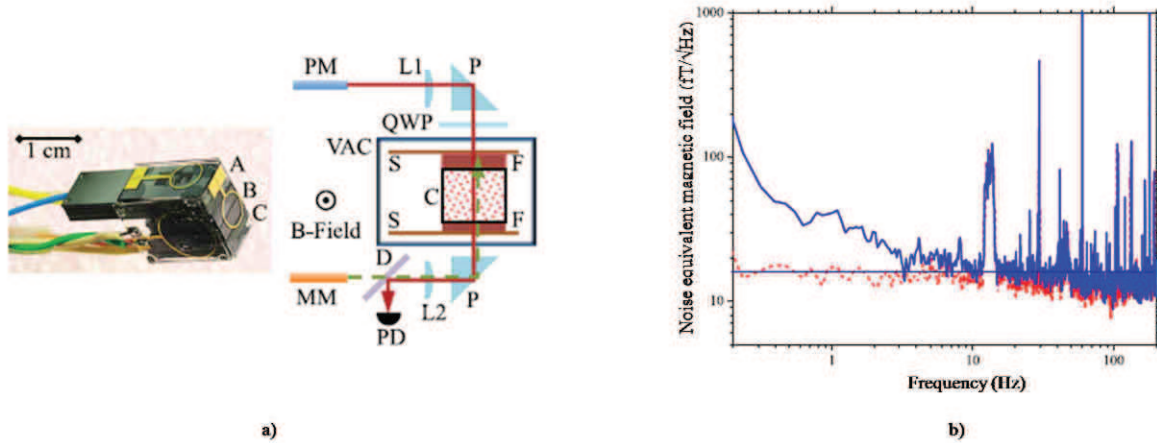


Figure 20. a) Miniature atomic magnetometer presented by NIST (using magnetically driven spin precession) and its building blocks [2], b) Noise spectral density of the sensor [2].

The vapour cell was heated to 150°C and the magnetometer was operated in low ambient magnetic field. The RF magnetic field was supplied by externally mounted Helmholtz coils (c.f. Fig. 20a). The sensor head's volume is 0.36 cm<sup>3</sup>. It reaches a sensitivity of 20 fT/√Hz for frequencies above 5 Hz (c.f. Fig. 20b).

### 1.2.5.3. Twinleaf Inc.

Twinleaf Inc, a start-up created by scientists from Princeton University, claims to commercialize miniature atomic magnetometers operating in the SERF regime (c.f. Fig. 21).

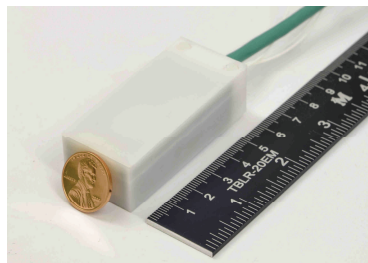


Figure 21. SERF-2 magnetometer commercialized by Twinleaf Inc. [22].

Neither technical data concerning its construction nor technological solutions employed are available. The external dimensions of the sensor head are 16x27x60 mm<sup>3</sup>. It is specified to reach sensitivities below 5 fT/√Hz at low ambient magnetic field. The unit cost of a system of this type is presently around 30k USD.

### 1.2.6. Summary

The ten presented constructions are, to the author's knowledge, the only ready-to-use examples of miniaturized atomic magnetometers reported in the literature. The group at NIST institute presented several other solutions, the ones presented in 1.2.2.2, 1.2.3.1 and 1.2.5.2 are the most recent. Several other groups in China and Japan reported bench-top systems using miniaturized alkali atom vapour cells although they don't seem to have reached a level of maturity allowing to obtain a stand-alone

device. A brief summary of the performance of reported miniaturized atomic magnetometers is presented in Table 4. SERF magnetometers are neglected because they don't fit in the scope of this thesis.

Table 4. Summary of performance of the presented magnetometers.

Group	Type of sensor	Active medium	Cell dimensions	Sensor head dimensions	Sensitivity	Isotropy	Ambient magnetic field	Ref.
Polatomic Inc.	He <sup>4</sup> optically pumped	He <sup>4</sup>	6 cm <sup>3</sup>	432 cm <sup>3</sup>	10 pT/√Hz	Single axis	Earth's field	[13]
TU Graz	CPT	<sup>87</sup> Rb	1 cm <sup>3</sup>	137 cm <sup>3</sup>	70 pT/√Hz	Isotropic	up to 1 mT	[15]
NIST	CPT	<sup>87</sup> Rb	1 mm <sup>3</sup>	12 mm <sup>3</sup>	50 pT/√Hz at 10 Hz	Isotropic	up to 1 mT	[3]
NIST	M <sub>x</sub>	<sup>87</sup> Rb	2 mm <sup>3</sup>	~ 17 mm <sup>3</sup>	5 pT/√Hz	Single axis	up to 10 μT	[16]
IPHT	M <sub>x</sub>	Cs	50 mm <sup>3</sup>	?	15 pT/√Hz at 10 Hz	Single axis	Earth's field	[17]
NIST	Bell-Bloom (FM*)	<sup>87</sup> Rb	< 1 mm <sup>3</sup>	< 1 cm <sup>3</sup>	2.7 pT/√Hz	Single axis	7 μT	[18]
IPHT	Bell-Bloom (IM**)	Cs	50 mm <sup>3</sup>	?	0,5 fT/√Hz	Single axis	50 μT	[19]

\* Frequency-modulated pump beam.

\*\* Intensity-modulated pump beam.

All of the presented constructions are still at research stage although most of them are mature enough for a technology transfer. Twinleaf Inc. issued from the work of T. Kornack at Princeton University, is the only organism, which mentions future commercialization of Earth's-field scalar magnetometers. Its claimed sensitivity is 10 pT/√Hz in a bandwidth of 100 Hz [23]. Nevertheless, like for their SERF magnetometer (1.2.5.3) no information is available on its construction.

Between 2007 and 2011 another American company, Geometrics Inc, obtained SERDP<sup>3</sup> funding for a project aimed at miniaturisation of a scalar atomic magnetometer. Tables 5 and 6, issued from the project final report [24], summarize the performances which can be obtained for the moment with miniature alkali-based sensors and problems related with different architectures, especially dead-zones and heading errors.

<sup>3</sup> SERDP – Strategic Environmental Research and Development Program. Research and development funding program established by the United States Department of Defense

Table 5. Comparison of performance of different types of scalar atomic magnetometers. Extracted from SERDP project report, Geometrics Inc. [24].

Method	Sensitivity (pT)	Dynamic range (nT)	Dead zones	Implementation
CPT	10-100	100,000	None****	Small heading error, difficult signal processing
FMNMOR*	50-100	100,000	Equatorial	Very complicated optics
$M_x$	6	100,000	Polar and equatorial	Wire coil needed, crosstalk in arrays
Bell-Bloom (FLF**)	10-15	100,000	Polar	Extraneous resonances
Bell-Bloom (HLF***)	15-20	100,000	Polar	Easy

\* Frequency Modulated NMOR.

\*\* Full Larmor Frequency – one of operation modes of Bell-Bloom magnetometers.

\*\*\* Half Larmor Frequency - one of operation modes of Bell-Bloom magnetometers.

\*\*\*\* Not all designs allow a complete elimination of dead-zones.

Table 6 presents the results obtained during the project, including heading error, which is a rarely published result in the state-of-the-art. The minimal value of heading error of 2 nT is almost two orders of magnitude higher as compared to the one obtained by the SWARM magnetometer (50 pT) and aimed at by the present thesis. Anisotropy of measurement is of key importance in all mobile applications including spatial and military systems.

Table 6. Performance of different demonstrators obtained by Geometrics Inc. Extracted from SERDP project report, Geometrics Inc. [24].

	Prototype 1	Prototype 2	Commercial version 1	Commercial version 2
Physics package size (cm <sup>3</sup> )	10	10	10	1
Sensor power consumption (mW)	50	400	200	50
Electronics size (cm <sup>2</sup> )	200	100	100	30
Electronics power consumption (W)	5	2	2	0.5
Cell size (cm <sup>3</sup> )	0.001	2	2	0.001
Attainable sensitivity (pT/ $\sqrt{\text{Hz}}$ )	6	1	1	6
Measured sensitivity (pT/ $\sqrt{\text{Hz}}$ )	75	15	5	10
<b>Heading error (nT)</b>	<b>40</b>	<b>30</b>	<b>2</b>	<b>40</b>

### 1.2.7. Conclusion

In conclusion, it can be stated that the main advantage of the developed sensor, as related to the state-of-the-art constructions presented in this section, is its unprecedented accuracy. It allows to limit heading errors to below 50 pT (case of the SWARM magnetometer) and thus to obtain an isotropic measurement. This feature is of key importance in all mobile applications which will be addressed by the miniature version of the sensor.





## Chapter 2: Helium gas cell

---

---

2.1.	Desired specifications	45
2.2.	Glassblown cells	46
2.3.	Gas purity	47
2.4.	Impedance matching	49
2.4.1.	Electrical equivalent circuit of the discharge	49
2.4.2.	Resonant impedance matching networks	49
2.4.3.	Discharge impedance and power transfer	51
2.5.	High-frequency breakdown and the low pressure limit	54
2.5.1.	HF breakdown mechanism	55
2.5.2.	Breakdown voltage measurement	57
2.6.	Alfa and gamma modes and the high pressure limit	61
2.7.	Optimal pressure and its scaling with size	63
2.7.1.	Metastable density	63
2.7.2.	Metastable relaxation	76
2.7.3.	Optimal pressure	83
2.8.	Conclusion	84

---

---

### Chapter highlights

- The problem of matching the impedance of the cell and the discharge to the generator is discussed.
- The value of pressure with which the helium cells can be filled is bounded from the low side by the breakdown mechanism. Below a certain value it becomes impossible to ignite a discharge. Discharge ignited near this critical value is very unstable.
- From the high-side the value of pressure is bounded by the decreasing electron temperature in the discharge and the destruction of metastable atoms by three-body collisions.
- A simple numerical model, describing the scaling of metastable density and relaxation time with pressure and size is developed. It is experimentally validated.
- Maximum values of sensitivity of 3.5 and 8 pT/ $\sqrt{\text{Hz}}$  are obtained for 20 Torr  $\Phi 10 \times 10$  mm and 40 Torr  $\Phi 5 \times 5$  mm glassblown cells respectively.





## 2. Helium gas cells

Helium-4 magnetometers use capacitively-coupled plasma sources as a mean to create triplet metastable helium atoms whose quantum properties underlay their operation principle. Sensors of this type, developed up to date, are based on glassblown helium cells a few centimetres in size, filled with high-purity helium-4 to a pressure of about 1 Torr, which is an empirically determined value. To the author's knowledge no theoretical studies have been done up to date on the effects of miniaturization of such plasma sources as related to magnetometry.

The fundamental sensitivity limit of atomic magnetometers depends on the number of sensitive species (triplet metastables in this case) and their transverse relaxation time. Size reduction of the active element triggers an inevitable decrease of both.

In order to compensate for this effect, the number of sensitive atoms has to be increased. The development of miniature alkali vapour magnetometers followed the path of increasing the pressure inside the cell, which in their context means increasing its internal temperature. When it comes to helium magnetometers, the problem is largely more complex. The two important parameters –  $2^3S_1$  metastable atom density and their relaxation time are a consequence of complex phenomena taking place in the discharge. Moreover, the physics behind miniature plasma sources is still not fully understood, although it is an area of constantly growing interest in plasma physics for many years. What is more, the predicted pressure range (tens of Torrs) is considered useless for most of the other applications, which adds to the difficulty of the problem since not much experimental work has been done in the subject and plasma behaviour is said to vary significantly with pressure.

Scientists working in the domain of plasma physics have generally the convenience of a direct access to the plasma, provided by the construction of their reactors. This allows a direct measurement of many parameters, using Langmuir probes for example. The discharge, discussed here, is hermetically confined inside a Pyrex cell therefore electrically speaking this amounts to a “black box” problem. It is only possible to measure the voltage or current flowing through and, having this information, draw some conclusions on its behavior.

The object of this chapter is to identify a reasonable helium pressure range with which it is possible to create a miniature helium magnetometer and find an optimal value within this range allowing to maintain high performance characteristics of the miniaturized sensor. The desired set of specifications is presented in §2.1.

On one hand, a small value of the product of pressure and helium cell dimensions (electrode separation) results in very high values of power necessary to ignite the discharge and its afterward instability which imposes a lower limit on the possible pressure value used in miniature cells. This aspect is discussed in §2.5.

On the other hand, multiple phenomenon leading to the instability of the discharge and the destruction of the  $2^3S_1$  metastable state impose an upper limit on the value of pressure. This problem is addressed in §2.6 and §2.7.

### 2.1. Desired specifications

The key constraints on the gas cell, the behaviour of the HF discharge and resulting properties of the triplet metastable population, which allow to obtain a high performance helium-4 magnetometer can be expressed with the following points.

- Internal atmosphere – the cells are filled with high-purity helium-4 (grade 6 – 99.9999% of purity). The amount of impurities should be limited to an absolute minimum since they tend to quench metastable atoms thus causing a decrease in their relaxation time and degrading the performance of the sensor
- Power consumption – the discharge should consume a reasonably small amount of power. In practice, the power required for ignition is at least an order of magnitude higher than the minimal power necessary for the maintenance of the discharge. The ignition power should have a reasonably small value compatible with “handheld” applications aimed by the miniaturization process. Attention should be paid at this stage to the ElectroMagnetic Interference (EMI) emissivity levels required by the standards relevant for the application of interest.
- Stability – once ignited, the discharge should be stable and easy to maintain at the limit of extinction, which is in general the optimal operating point of the magnetometer. The power at the limit of extinction should be in the range of few miliwatts.
- Sensitivity – the sensitivity of atomic magnetometers depends on the number of magnetically sensitive species and their transverse relaxation time. Both of these values are determined by the pressure of helium inside the cell therefore an optimal value must be found in order to maximize the sensitivity.
- Uniformity – the radial distribution of metastable atoms inside the discharge is never perfectly uniform. In the simplest case, the maximum value of metastable atom density is in the middle of the cell and decreases towards the walls. This occurs when the majority of metastable atom creation mechanisms take place in the center of the discharge and atoms experience a diffusive loss towards the walls of the cell. The need for such a distribution is dictated by the fact that the majority of pumping light power passes through the center of the cell (Gaussian beam).

The internal atmosphere of the cells will be analyzed by means of emission spectroscopy in §2.3. The power consumption and discharge stability criteria will be monitored by experimental measurements backed by literature information. Finally, the last two criteria will be addressed by developing a numerical model which will be validated experimentally in §2.7.1.2.

## 2.2. Glassblown cells

Fifteen glassblown helium cells were fabricated for the needs of this study. All of which are cylindrical cells. Ten cells were fabricated with an internal diameter of 5 mm and 5 mm length, and five cells with an internal diameter of 10 mm and 10 mm length (c.f. table 7). The cells were made by two different suppliers: the French glassblower Verre Equipement (named VE thereafter) and the NIST supplier Precision Glassblowing (subsequently cited as GB). The quality of the cells from these two manufacturers will also be investigated in this thesis.

Figure 22 presents a comparison between a cell used for the SWARM project and a miniature  $\Phi 5 \times 5$  mm glassblown cell.

Table 7. Glassblown cells fabricated for the need of the study

Size (mm)	Pressure (Torr)	Supplier	Fabrication date
Φ5x5	5	GB	09/2010
Φ5x5	10	GB	09/2010
Φ5x5	10	GB	11/2012
Φ5x5	20	VE	20/06/2011
Φ5x5	20	GB	09/2010
Φ5x5	20	GB	11/2012
Φ5x5	30	GB	11/2012
Φ5x5	40	GB	11/2012
Φ5x5	50	GB	09/2010
Φ5x5	150	GB	11/2012
Φ10x10	2	VE	14/04/2011
Φ10x10	12	VE	16/11/2010
Φ10x10	20	VE	2013
Φ10x10	20	VE	2013
Φ10x10	30	VE	9/06/2011



Figure 22. Φ5x5 mm glassblown cell compared to the cell used for the SWARM project (Φ30x45 mm).

### 2.3. Gas purity

The main advantage of the VE glassblown cells is that they are filled with helium at the CEA following an internal procedure, which results in a high repetability and reliability of the process. The cells are initially fabricated with a small capillary (evacuation pipe) on the side (cf. Fig. 23) which ends with a glass-metal high vacuum connector. This setup is connected to a dedicated vacuum system containing a turbo-molecular pump [5].

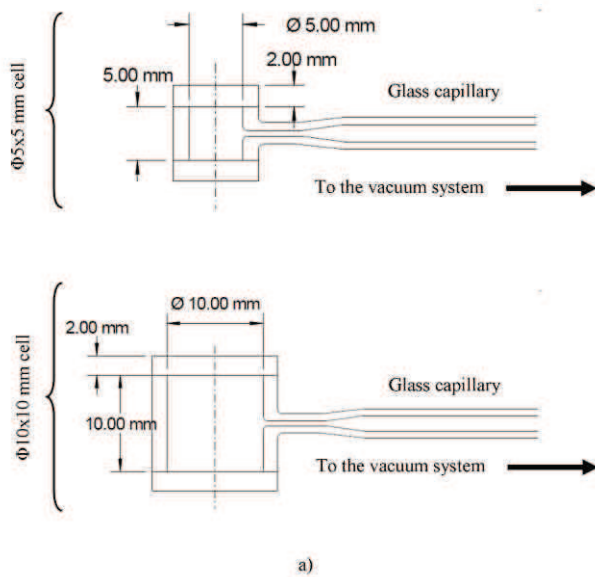


Figure 23. a) Glassblown helium cells – sketch. b) Φ5x5 mm cell with a capillary.

The filling procedure consists of several steps [5]:

- evacuation of the gas ( $10^{-7}$  mbar of vacuum),
- annealing at  $500^{\circ}\text{C}$ ,
- filling with helium,
- establishing and maintaining a microwave discharge inside the cell,
- high vacuum evacuation of the gas ( $10^{-7}$  mbar).

These steps are cycled several times in order to obtain a complete desorption of the glass. The impurities present in its structure are replaced by helium atoms which results in a clean atmosphere inside the cell. In the final step the evacuation pipe is cut off using a burner. This process leaves a small glass tip (fill stem) on the side of the cell.

The inconvenience of American cells is that they are filled by the manufacturer, whose filling process does not allow for the microwave discharge step. Nevertheless GB cells are a lot cheaper (450\$ as compared to about 2000€) which makes them an interesting alternative. The majority of cells used in this study were produced by GB. The purity of both types of cells has been inspected by emission spectroscopy of the discharge. Figure 24 presents a comparison of spectra of cells manufactured by both suppliers.

Some oxygen lines are clearly visible in the spectrum of GB cells. The presence of small amounts of oxygen is known to have a significant influence on the density of  $2^3\text{S}_1$  metastable atoms in a helium plasma. Literature suggests that an addition of 500 ppm of  $\text{O}_2$  may decrease the metastable density by a factor of five [25]. Unfortunately it is not possible to predict exactly the concentration of oxygen from the emission spectra. This problem will be addressed later in this chapter, where some additional attention will be paid to the influence of impurities present inside those cells since it is potentially a factor directly influencing the sensitivity of the designed magnetometer.

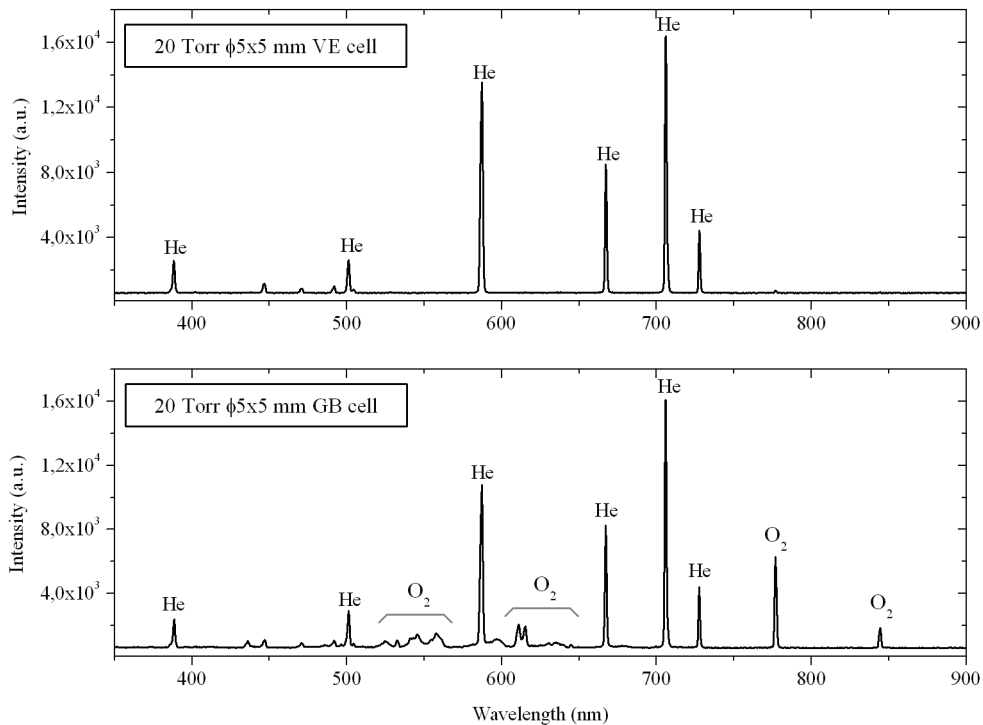


Figure 24. Comparison of emission spectra of 20 Torr 5x5 mm cells from different manufacturers.

## 2.4. Impedance matching

In order to realize the capacitive coupling of power into the discharge, an impedance matching network has to be used. It adapts the impedance of the helium cell and the discharge (once it is ignited) to the  $50\ \Omega$  impedance of the generator and thus maximizes the power transfer.

This section describes the helium discharge in electrical terms. It presents the solutions used to match the impedance of the discharge and a simplified analysis of the circuit.

### 2.4.1. Electrical equivalent circuit of the discharge

Capacitively coupled plasma is a mixture of charged, uncharged and neutral particles which are in constant movement resulting from diffusion and drift (due to electric field). Since the exciting signal is periodic we can expect that charged particles will perform an oscillatory motion. Figure 25a presents this movement in different phases of the HF cycle.

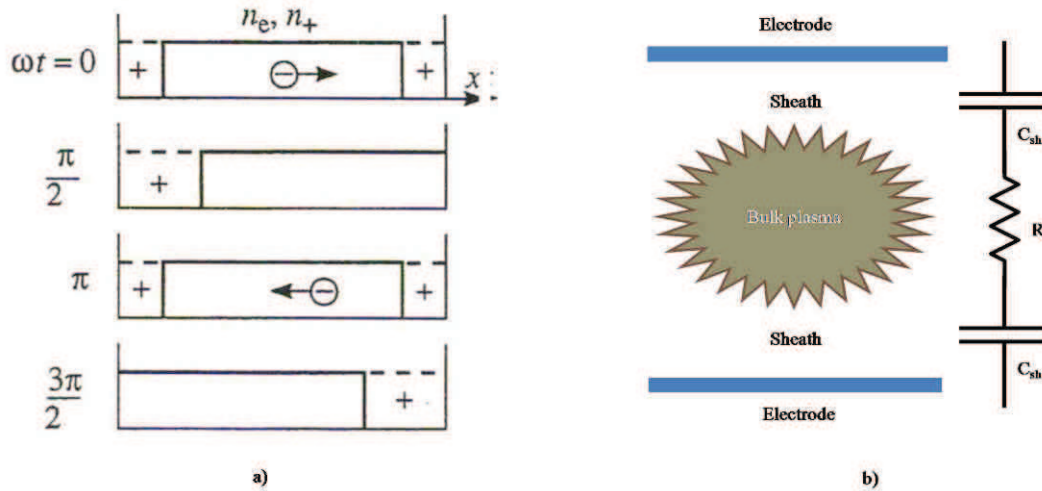


Figure 25. a) Oscillatory movement of electrons [26]; b) Simple equivalent electrical circuit of the discharge.

As electron mobility is nearly two orders of magnitude higher than ion mobility, ions can be considered as immobile. In such a description, the electron concentration will always be the highest in the centre of the cell. Consequently, to a first approximation, such a situation can be described in electrical terms with an equivalent circuit shown in Fig. 25 b where  $C_{sh}$  represents the ion-rich area (called sheath) and  $R_b$  the electron-rich area (bulk plasma).

### 2.4.2. Resonant impedance matching networks

The resonant character of an impedance matching network allows to “amplify” the voltage across the cell in order to reach the breakdown (ex. normally 1 W of power over  $50\ \Omega$  gives about 7 V which is not enough to cause a breakdown). Figure 26 shows a matching network used for the SWARM project. It uses a pair of identical inductors ( $L_1$  and  $L_2$ ) to match the impedance and another pair ( $L_3$  and  $L_4$ ) forming a rotating transformer to provide a convenient rotating joint (the impedance matching network moved along with the polarizer c.f. §1.1.5).

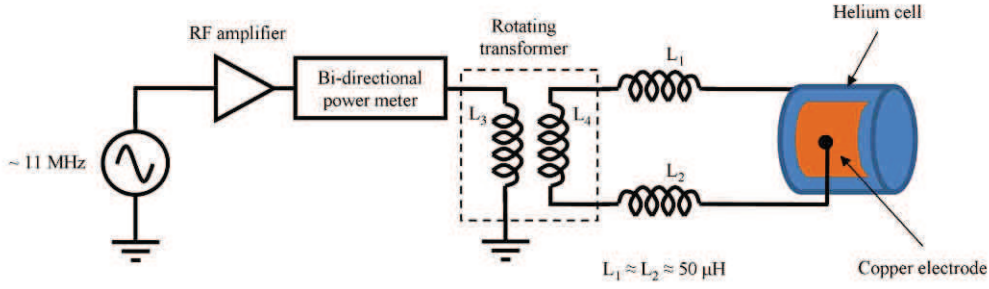


Figure 26. Impedance matching network for the SWARM macroscopic magnetometer.

It should be noted that the coupling of the transformer is not ideal; it is estimated to about 50%. In order to facilitate the analysis, lower the power consumption and make the circuit smaller (there is no need for a rotating transformer in the miniature sensor) a modified version presented in Fig. 27 was designed in the course of this thesis.

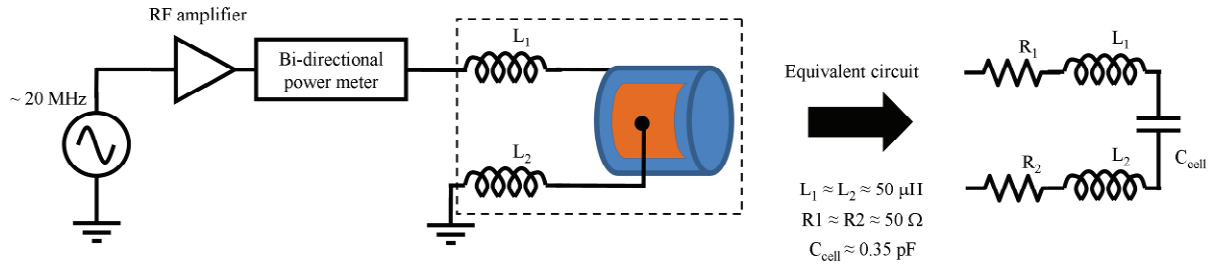


Figure 27. Impedance matching network for the miniature magnetometer.

The  $50 \Omega$  matching is provided by the parasitic resistance ( $R_1$  and  $R_2$ ) of the inductors ( $L_1$  and  $L_2$ ) which is related to skin and proximity effects. It can be estimated numerically [27] to about  $50 \Omega$  per inductor at the circuit resonance frequency, which is a sufficiently close value.

The capacitance of the cell ( $C_{\text{cell}}$ ) cannot be determined by a simple parallel plate formula because the distance between the electrodes is comparable to their characteristic size ( $5 \times 5 \text{ mm}^2$ ) therefore fringing is no longer negligible. It is often assumed that self-capacitance of a metal plate is equal to  $1 \text{ pF}$  times its largest characteristic dimension in cm. The capacitance of the cell, calculated with this approximate assumption, should be of the order of  $0.35 \text{ pF}$  (two electrodes in series), which makes it an order of magnitude larger compared to the one given by the parallel plate formula.

When the capacitive (due to  $C_{\text{cell}}$ ) and inductive (due to  $L_1$  and  $L_2$ ) reactances become equal to each other, the circuit enters resonance (the imaginary part disappears). The most difficult task is to design the circuit so that resonance condition and the  $50 \Omega$  matching occur at the same frequency. Due to stray capacitances and inductances the circuit is never ideal.

At resonance the voltage rises very rapidly, reaching the breakdown value. Once the discharge is established the characteristics of the circuit change due to the discharge impedance (c.f. Fig. 28). The circuit becomes slightly detuned from resonance (influence of the capacitive part  $C_{\text{sh}}$ ) and the ratio of reflected to forward power, measured by the power meter, rises due to the resistive part  $R_b$  (c.f. Fig. 28b).



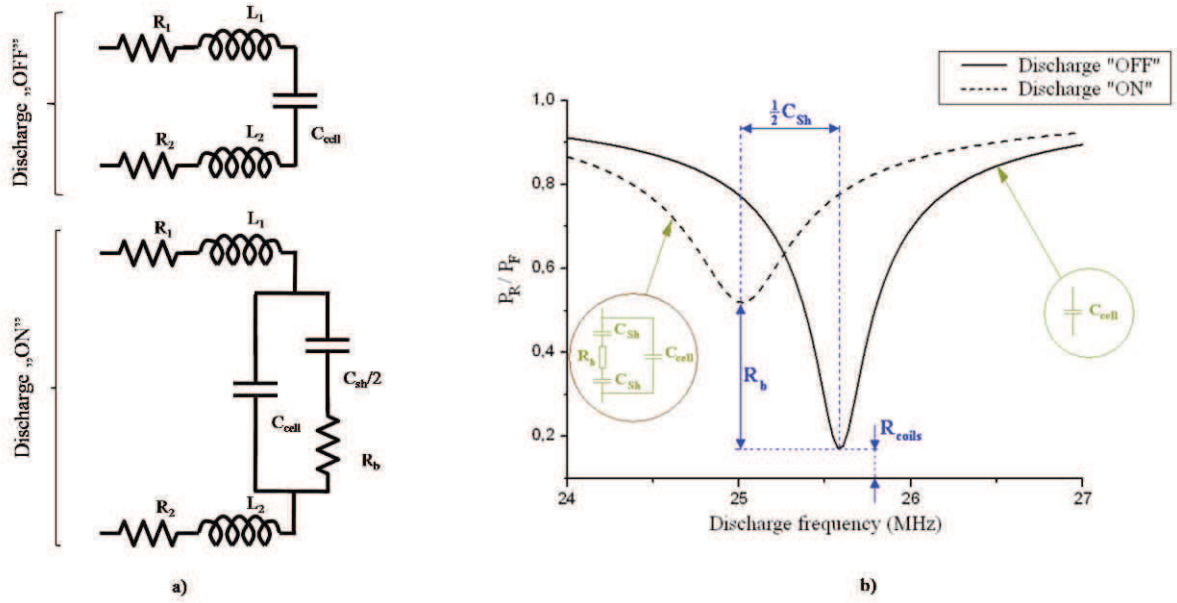


Figure 28. a) Equivalent circuits before and after discharge ignition. b) The ratio of reflected to forward power ( $P_R/P_F$ ), measured with a bidirectional power meter as a function of frequency.

### 2.4.3. Discharge impedance and power transfer

The amount of power which is actually dissipated into the discharge allows to obtain important information about the plasma. It will be used as input data in a numerical description of the discharge which helps to predict the optimal value of helium pressure for the designed magnetometer.

The value of absorbed power measured at the input of the matching network by the bi-directional power meter (c.f. Fig. 27) is not the actual value consumed by the discharge. The matching inductors ( $L_1$  and  $L_2$ ) consume a significant part of it due to their series resistance. In order to quantify the generator-discharge power transfer, an estimate of the discharge impedance is necessary.

The discharge impedance can be determined approximately from the ratio of reflected to forward power ( $P_R/P_F$ ) measured by the power meter. Results obtained this way are rough estimates rather than precise measurements which would require much more precise experimental methods and instruments.

The  $P_R/P_F$  ratio is a measure of detuning of the circuit impedance ( $Z_{Circ}$ ) from the generator impedance ( $50 \Omega$ ). It can be expressed by Eq. 14.

$$\frac{P_R}{P_F} = \left( \frac{Z_{Circ} - 50}{Z_{Circ} + 50} \right)^2 \quad (14)$$

The equivalent circuit of the matching network before the discharge is ignited is presented in Fig. 29. It contains additional parasitic components: coil capacitance ( $C_{L1}$  and  $C_{L2}$ ) and series resistance ( $R_s$ ) related with wires and solder (few ohms). It can be simplified using coils and cell impedances ( $Z_{L1}$ ,  $Z_{L2}$  and  $Z_C$ ).

The impedance of a coil can be expressed with Eq. 15.

$$Z(j\omega) = \frac{R + j\omega L}{1 + j\omega RC + (j\omega)^2 LC} \quad (15)$$



This simplifies the expression of the circuit impedance before the ignition of the discharge to Eq. 16.

$$Z_{Circ} = Z_{L1} + Z_{L2} + Z_C + R_S \quad (16)$$

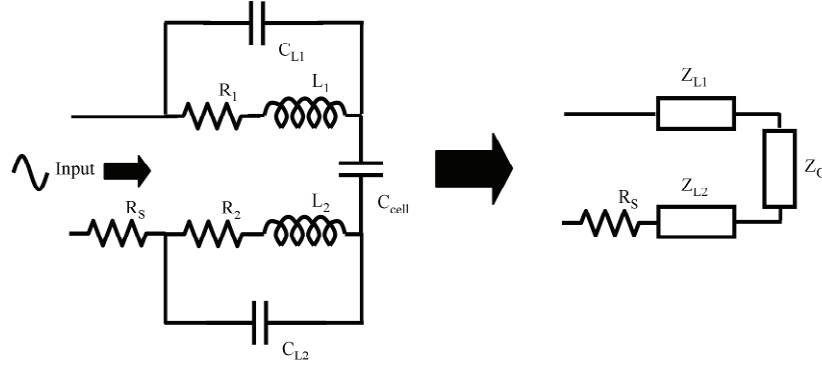


Figure 29. Equivalent circuit of the matching network before the ignition of the discharge

The inductance of the inductors was measured using a precision LCR bridge. Values of 38.6 and 39.1  $\mu\text{H}$  were obtained. In order to determine the missing parameters a measurement of the  $P_R/P_F$  ratio was done for several values of frequency close to the resonance frequency using a power inferior to the breakdown power (discharge “off”). The obtained values were fit with the above set of equations (Eq. 14 to 16). Results are presented in Fig. 30 and table 8.

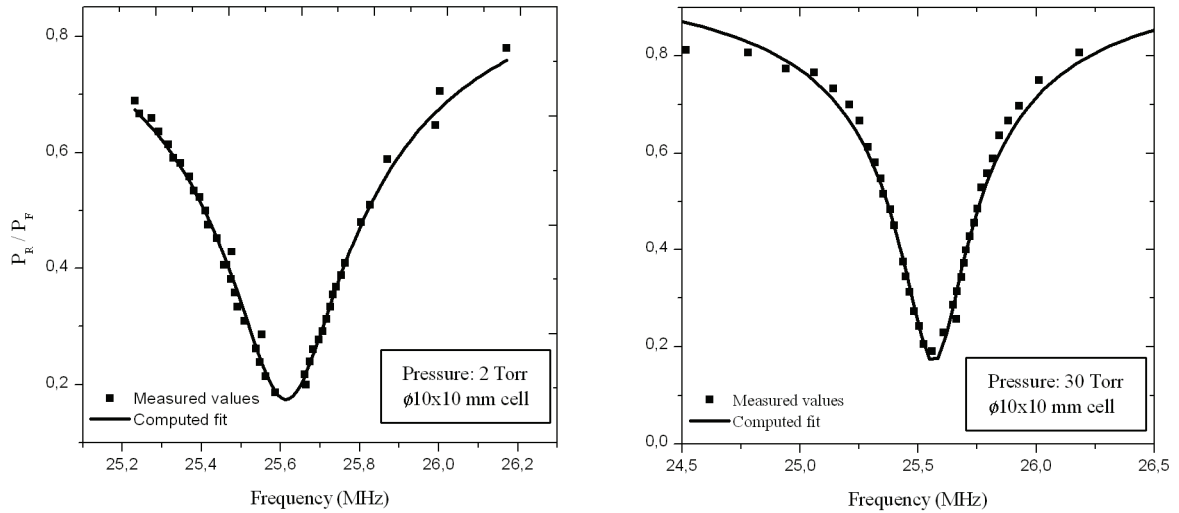


Figure 30. Experimental values of  $P_R/P_F$  for two  $\Phi 10 \times 10$  mm cells vs. computed fits.

Once the discharge is ignited, the resonance frequency shifts towards lower values and the corresponding maximal value of  $P_R/P_F$  increases (c.f. Fig. 28b) due to the appearing discharge impedance ( $Z_{dis}$ ). This situation is presented in Fig. 31.

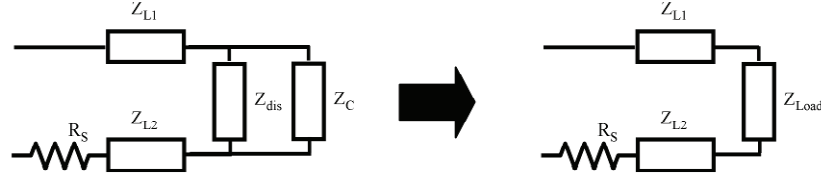


Figure 31. Equivalent circuit of the matching network after the ignition of the discharge

The equivalent impedance ( $Z_{Load}$ ) in this case is composed of a parallel connection of the cell impedance ( $Z_{cell}$ ) and discharge impedance ( $Z_{dis}$  – c.f. Fig. 28a). Assuming that at resonance the reactive part disappears, the resistive part of  $Z_{Load}$  can be expressed by Eq. 17.

$$\text{Re}(Z_{Load}) = R_{equiv} = \frac{50 \left( 1 + \sqrt{\frac{P_R}{P_F}} \right)}{1 - \sqrt{\frac{P_R}{P_F}}} - [\text{Re}(Z_{L1}) + \text{Re}(Z_{L2}) + R_S] \quad (17)$$

The reactive part ( $X_{Load}$ ) of the load impedance is equal to the reactance of the inductors (resonance condition, c.f. Eq. 18).

$$\text{Im}(Z_{load}) = X_{Load} = -[\text{Im}(Z_{L1}) + \text{Im}(Z_{L2})] \quad (18)$$

Finally, the discharge impedance can be calculated using Eq. 19.

$$Z_{dis} = \frac{Z_{Load} Z_{cell}}{Z_{cell} - Z_{Load}} \quad (19)$$

The results obtained for two helium cells are presented in table 8. Once ignited, the discharge was operated at the limit of extinction in both cases.

Table 8. Obtained parameters.

Helium cell	Discharge “off”				Discharge “on”				
	$f_{rez}$ (MHz)	$Z_{L1}$ ( $\Omega$ )	$Z_{L2}$ ( $\Omega$ )	$C_{cell}$ (pF)	$f_{rez}$ (MHz)	$Z_{Load}$ ( $\Omega$ )	$Z_{dis}$ ( $\Omega$ )	$R_B$ ( $\Omega$ )	$C_{sh}$ (fF)
2 Torr	25.611	65+j7.6k	56+j6.8k	0.434	25.102	187-j14.0k	84k-j283k	84k	45
30 Torr	25.558	78+j8.4k	43+j6.2k	0.429	25.566	155-j14.6k	121k-j440k	121k	30

Active power is only absorbed by the resistive parts of  $Z_{L1}$ ,  $Z_{L2}$  and  $Z_{Load}$ . This means that roughly half of the power absorbed by the matching network is actually transferred to the discharge.

An ideal matching network would consist of a variable impedance element, for which the resistance would change from 50 to 0  $\Omega$  after ignition. This is basically the concept of automatic impedance matching networks widely used in the plasma processing industry where even a slight detuning from the generator impedance may cause a power loss of several Watts. In a future perspective, the development of such a circuit for a miniature version of a helium magnetometer seems very beneficial. Apart from the obvious ease of use (especially in a sensor array), miniature sensors are

increasingly subjected to very strict power consumption requirements therefore all means to decrease it are of key importance.

## 2.5. High-frequency breakdown and the low pressure limit

The value of helium pressure, which can be used to fill the cell of a helium magnetometer, is bounded from the low side by the power consumption and discharge stability criteria (c.f. §2.1).

In the simplest case of a DC discharge, the processes leading to the development of plasma are described by Paschen's law which expresses the dependence of breakdown voltage on the product of pressure and electrode separation (c.f. Eq. 20).

$$V_B = \frac{B_{He} p d}{\ln \left( \frac{A_{He}}{\ln(1 + 1/\gamma) + \ln(p d)} \right)} \quad (20)$$

Where:  $B_{He}$  – molecular constant.  $B_{He} = 5.3 \cdot 10^3 \text{ (Torr} \cdot \text{m)}^{-1}$  [28]

$A_{He}$  – molecular constant.  $A_{He} = 80 \text{ (Torr} \cdot \text{m)}^{-1}$  [28]

$p$  – pressure (Torr)

$d$  – electrode separation (m)

$\gamma$  – secondary electron emission coefficient.  $\gamma = 0.23$  [29]

Calculated DC breakdown voltages for three values of electrode separation are presented in Fig. 32a. It can be seen that below a certain threshold, which depends on the electrode separation (size of the helium cell), this power starts to increase exponentially and the ignition of the discharge becomes impossible.

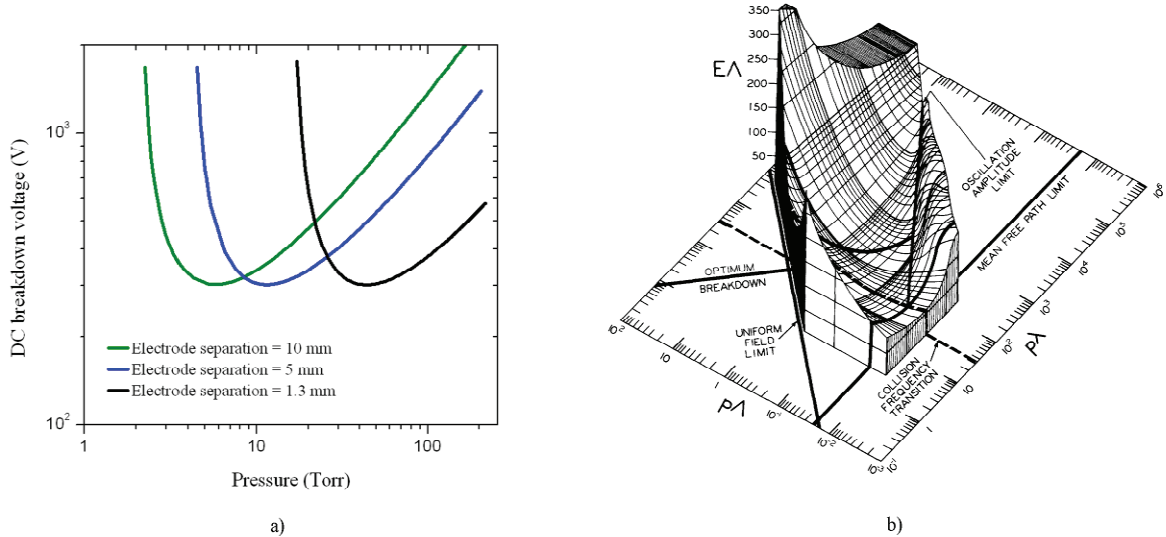


Figure 32. a) Paschen curves, DC breakdown voltage in helium. b) RF breakdown in hydrogen [30].

Paschen's law applies for the case of DC discharges therefore it fails to fully describe the breakdown used in helium magnetometers, which use HF excitation (11-25 MHz). In order to predict

the limiting value of helium pressure for the designed magnetometer an understanding of the mechanism of HF breakdown is necessary.

The description of the HF breakdown is more complex due to the presence of another degree of freedom, namely the frequency of the applied field. The easiest way to present it is in terms of dependence of  $E\Lambda$  on  $p\Lambda$  and  $p\lambda$ , where  $\Lambda$  stands for the characteristic diffusion length<sup>4</sup> and  $\lambda$  is the wavelength of the applied HF field  $E$ . A representation like this is shown in Fig. 32b for the case of hydrogen. Similar literature data for helium discharges have not been found in the range of pressure and electrode spacing of interest.

### 2.5.1. HF breakdown mechanism

The discussion of HF gas breakdown will be largely based on the studies of Brown [30] and Park et al. [31] who studied this phenomenon in detail for helium-mercury and helium-nitrogen plasmas respectively.

The simplest case of HF capacitively-coupled plasma (CCP) breakdown is presented in Fig. 33. It consists of two parallel plate electrodes. One of the electrodes is powered by an RF electric field source and the other one is grounded. The imposed electric field has a sinusoidal waveform ( $E_0 \exp(j\omega t)$  with  $E_0$  - amplitude). The initial ionization ( $I_{init}$ ) originates either from the interaction with cosmic rays or some external radiation source with the inert gas and has a very small value.

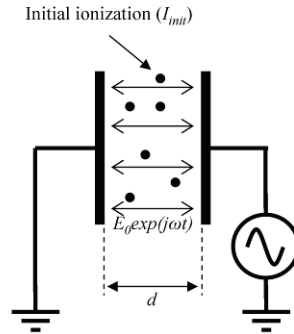


Figure 33. Basic CCP excitation scheme.

In vacuum, an electron accelerated by the external electric field oscillates 90 degrees out of phase and thus gains no energy from the field. If the space between the electrodes is filled by a gas, its oscillations are damped by the collisions with inert particles which can be considered as the only mean of energy transfer from the field to the electron.

Electric breakdown occurs when a balance is reached between the creation of free electrons through ionizing collisions and their loss due to wall collisions. Wall collisions happen either due to their chaotic movement caused by diffusion or due to acceleration by electric field (drift). Therefore we can distinguish two types of breakdown: diffusion-controlled (c.f. Fig. 34a) and drift-controlled (c.f. Fig. 34b).

<sup>4</sup> In a parallel plate configuration  $\Lambda = \frac{d}{\pi}$ , with  $d$  – electrode separation. For a cylindrical geometry  $\Lambda^{-2} = \left(\frac{2.405}{r}\right)^2 + \left(\frac{\pi}{l}\right)^2$ , with  $r$  – radius and  $l$  – length.

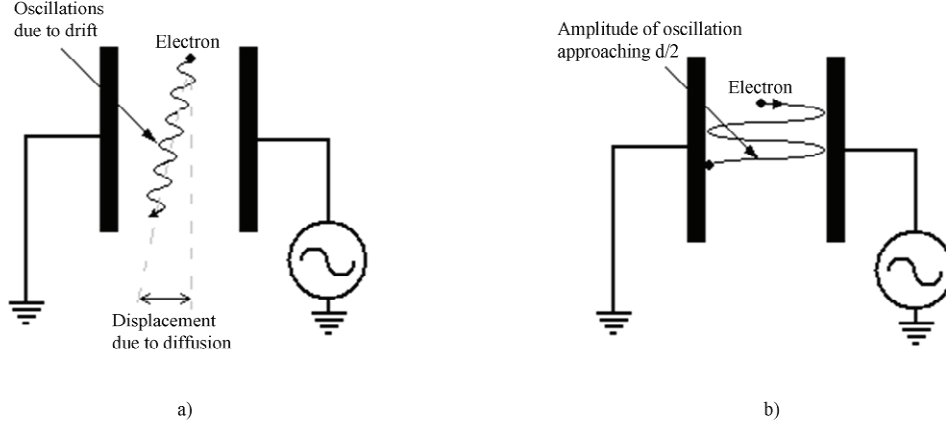


Figure 34. a) Diffusion controlled breakdown. b) Drift controlled breakdown.

- In the drift-controlled breakdown the amplitude  $A_e$  of drift oscillations becomes comparable to the electrode separation  $d$  (c.f. Fig. 34b) and the breakdown becomes drift-controlled rather than diffusion controlled. This in terms means that electrons will be lost during one HF cycle. This process is known to largely increase the amplitude of the field necessary to cause a breakdown [30][31] and cause its instability. Drift-controlled discharges behave similarly to DC discharges (basically the same mechanism) and their breakdown voltage can be described by the Paschen's law (c.f. Eq. 20 and Fig. 32).
- In the diffusion-controlled breakdown the “confinement” of electrons by the rapidly changing HF field effectively limits the electron loss to the walls and therefore lowers the value of electric field necessary for the breakdown. This is a very favourable phenomenon, when it comes to magnetometry applications, since it largely limits the power which needs to be applied to the matching network in order to ignite and maintain the discharge.

In order to predict the limits of the diffusion-driven breakdown it is necessary to derive an approximate analytical formula which expresses the amplitude of oscillation. Following [31] this can be done by using the drift-diffusion equation (Eq. 21) which expresses the balance between the creation of electrons through ionising collisions and loss through drift and diffusion. This balance is the breakdown condition.

$$\underbrace{-D_e \nabla n_e}_{\text{Diffusion term}} - \underbrace{n_e \mu_e E_B}_{\text{Drift term}} = \underbrace{n_e \nu_e}_{\text{Electron creation rate}} \quad (21)$$

Where:  $D_e$  – electron diffusion coefficient,  
 $n_e$  – electron density,  
 $\mu_e$  – electron mobility,  
 $E_B$  – electric field at breakdown,  
 $\nu_e$  – electron drift velocity.

In order to characterize the amplitude of the drift oscillations, it has to be considered that diffusion is negligible, therefore:  $D_e \nabla n_e = 0$ . This way Eq. 22 is obtained.

$$v_e n_e = -n_e \mu_e E_B \Rightarrow v_e = -\mu_e E_B \quad (22)$$

Since  $E_B$  is an oscillating field, the amplitude of electron oscillation  $A_e$  can be expressed with Eq. 23.

$$v_e = \frac{dx_e}{dt} = -\mu_e \frac{V_B}{d} \cos(\omega t) \Rightarrow A_e = \langle \mu_e \rangle \frac{V_B}{\omega d} \quad (23)$$

Where:  $x_e$  – displacement,

$V_B$  – breakdown voltage,

$A_e$  – electron oscillation amplitude,

$\omega$  – angular frequency of the applied field,

$\langle \mu_e \rangle$  – mean electron mobility,  $\langle \mu_e \rangle = 1.132 \cdot 10^{-1} (760/p) \text{ m}^2/\text{Vs}$ , with  $p$  – pressure in Torr.

To sum up the description, it is important to note that the boundary determined by  $A_e$  is not stepwise. The breakdown voltage increases quite sharply but there exists a certain intermediate region where both mechanisms have a pronounced influence.

## 2.5.2. Breakdown voltage measurement

The possibility to ignite the discharge with a relatively small amount of power is of key importance for a helium magnetometer. The low pressure limit for which it is still possible is a function of the electron loss mechanism which governs the gas breakdown. For instance, if the breakdown is drift-controlled (therefore described by the Paschen curves – c.f. Fig. 32a), its ignition may become impossible in a  $\Phi 5 \times 5$  mm cell filled to 4 Torr.

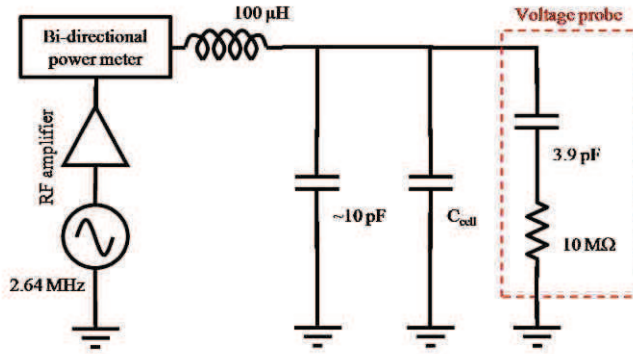
The major electron loss mechanism is determined by the dimensions of the cell, pressure and frequency of the applied field. In order to estimate a reasonable low pressure limit, a measurement of breakdown voltage as a function of those three parameters has to be done. The major electron loss mechanism can be then determined by comparing the value of  $A_e$  calculated using Eq. 23 with the dimensions of the cell.

### 2.5.2.1. Experimental setup

The measurement of voltage in HF resonance circuits is a complex task. The small value of capacitance of the helium cell makes such measurements impossible using impedance matching networks presented in §2.4.2. The circuit becomes detuned far from resonance immediately after connecting a voltage probe.

Previous work [5] suggests a measurement of current using a current probe and, given all the impedances in the circuit, afterward calculation of voltage. This approach was tested, unfortunately it failed since the current probe incorporated additional impedance to the circuit which was very hard to estimate accurately enough to obtain reliable measurements.

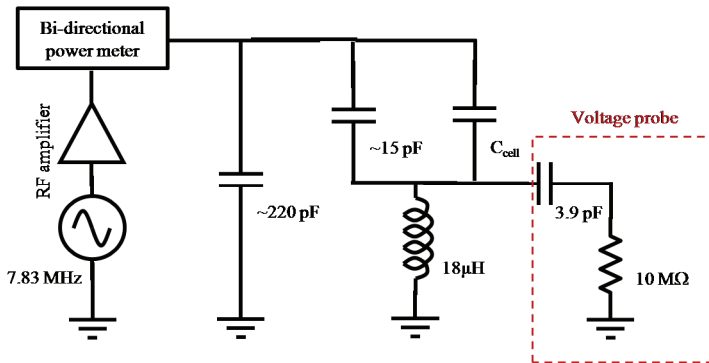
Another approach was chosen instead. Three dedicated matching circuits, operating at different frequencies, were designed to compensate for the capacitance of the voltage probe. These circuits are not intended to be used in the construction of a magnetometer (due to large power consumption) but as a measurement tool developed to allow for the necessary characterisations. The circuits are presented in Fig. 35, 36 and 37 along with a brief description.



**Circuit characteristics:**

- Resonance frequency: 2.64 MHz
- Direct voltage measurement
- Maximal voltage limited by the rating of the voltage probe to 400 V

Figure 35. Impedance matching network used for the breakdown voltage measurement at 2.64 MHz.



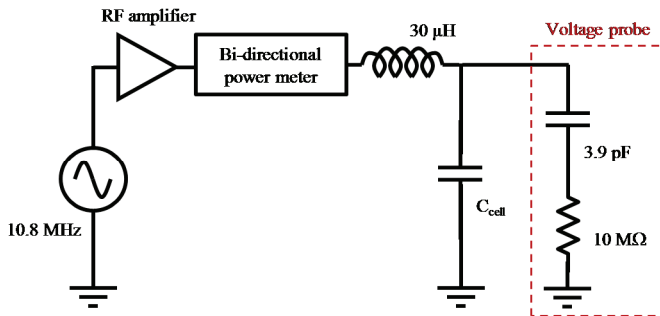
**Circuit characteristics:**

- Resonance frequency: 7.83 MHz
- Maximal voltage limited by the rating of the circuit elements to 260 V
- Indirect voltage measurement. Voltage on the cell:

$$V_{cell} = V_{mes} - \sqrt{P_{abs} \cdot 50 \Omega}$$

With:  $V_{cell}$  – voltage on the helium cell,  
 $V_{mes}$  – measured voltage,  
 $P_{abs}$  – absorbed power.

Figure 36. Impedance matching network used for the breakdown voltage measurement at 7.83 MHz.



**Circuit characteristics:**

- Resonance frequency: 10.8 MHz
- Direct voltage measurement
- Maximal voltage limited by the rating of the voltage probe to 400 V

Figure 37. Impedance matching network used for the breakdown voltage measurement at 10.8 MHz.

The operation principle of these matching networks is basically the same as described in §2.4.2. Commercially available inductors were used; the capacitors tune the resonant response of the circuit in order to adapt it to the parasitic resistance of the inductors.

The fine tuning of the circuits was done with trimmer capacitors. Once the circuit was tuned, trimmer capacitors were desoldered. Their capacitance was measured using a network analyser and they were replaced with high voltage ceramic capacitors of the same value (trimmer capacitors are rated 50 V).

The maximal voltage which could be measured using the circuits from Fig. 35 and 37 was limited by the voltage rating of the probe to approximately 400 V<sub>RMS</sub>. For the circuit from Fig. 36 a lower limit of 260 V<sub>RMS</sub> was imposed by the voltage rating of the capacitors used.

### 2.5.2.2. Results

Experimental values of the breakdown voltage as a function of pressure are presented in Fig. 38 to 40. These figures also present the applicable limits of the diffusion-driven breakdown, calculated using Eq. 23, assuming  $A_e = 0.5d$  (blue curve) and the Paschen curves which provide the values for a purely drift-driven discharge (red curves). All the experimental data are gathered in Fig. 41, where they are presented as a function of frequency.

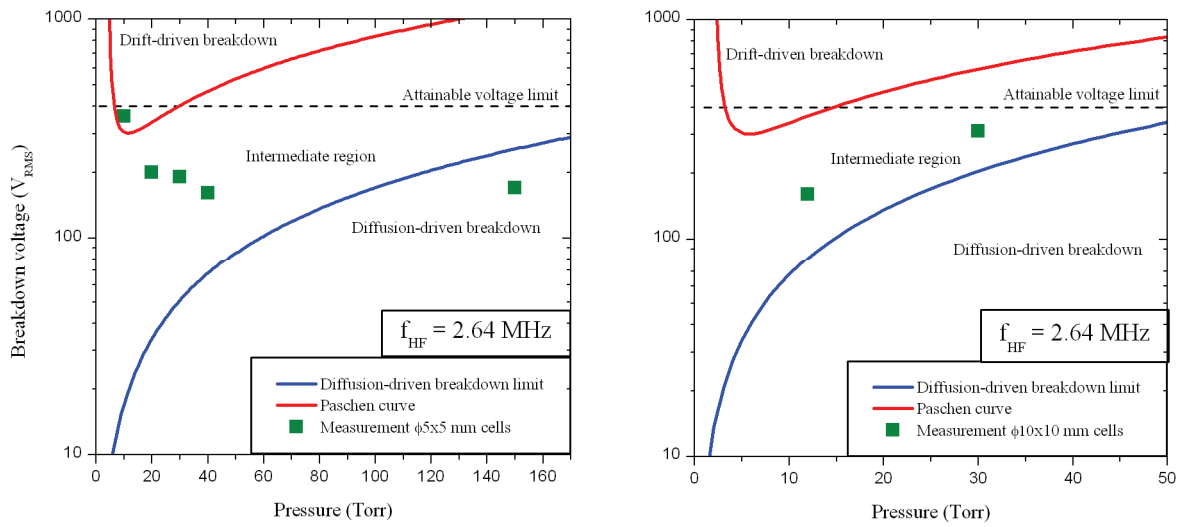


Figure 38. Experimental values of the breakdown voltage for  $\Phi 5 \times 5$  and  $\Phi 10 \times 10$  mm cells at 2.64 MHz.

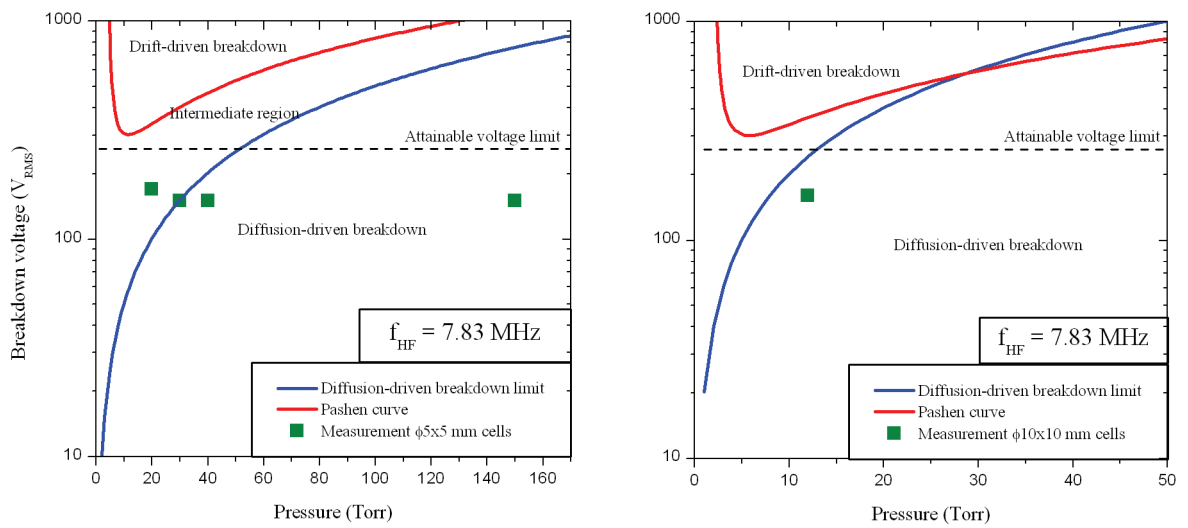


Figure 39. Experimental values of the breakdown voltage for  $\Phi 5 \times 5$  and  $\Phi 10 \times 10$  mm cells at 7.83 MHz.



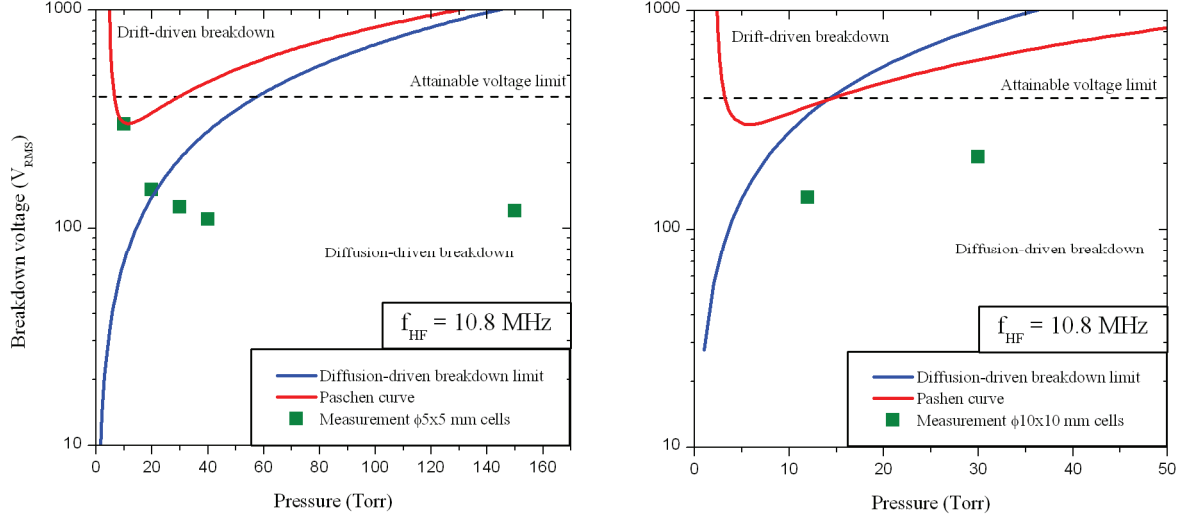


Figure 40. Experimental values of the breakdown voltage for  $\Phi 5 \times 5$  and  $\Phi 10 \times 10$  mm cells at 10.8 MHz.

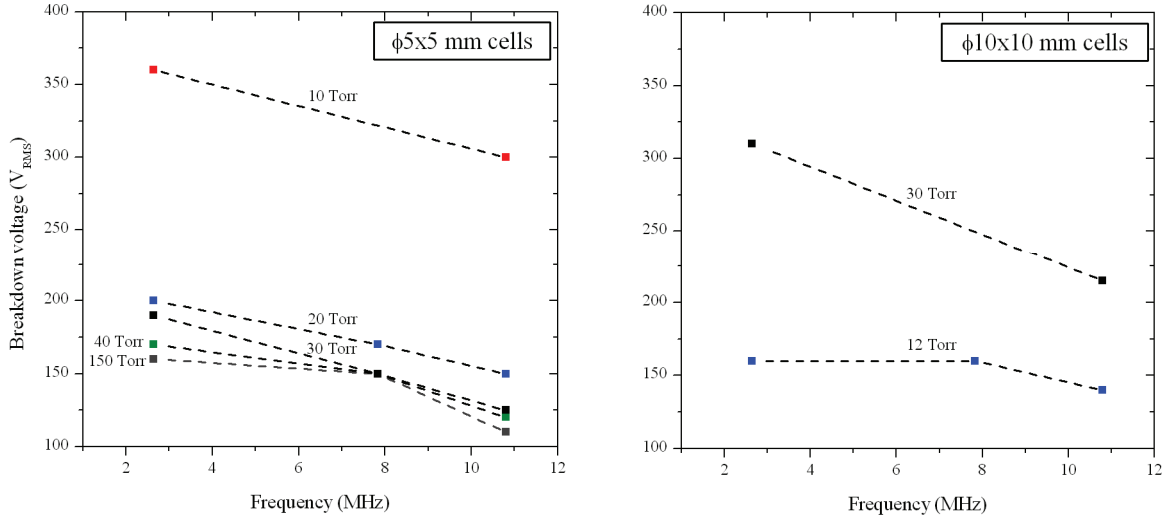


Figure 41. Experimental values of the breakdown voltage for  $\Phi 5 \times 5$  and  $\Phi 10 \times 10$  mm cells as a function of excitation signal frequency. Data points connected for clarity.

### 2.5.2.3. Conclusion

The gathered experimental data show clearly the evolution of the dominating electron loss mechanism with frequency.

The value of the breakdown voltage for  $\Phi 5 \times 5$  mm 5 Torr and  $\Phi 10 \times 10$  mm 2 Torr cells occurred higher than the maximal value which could be measured by the experimental setups (limit imposed by the voltage rating of the probe  $\sim 400$  V<sub>RMS</sub>). The ignition of a discharge in these two cells is also difficult using the matching network from Fig. 27. The power necessary to ignite the discharge is nearly an order of magnitude higher than for the rest of the cells. Consequently, this means that electron drift largely dominates diffusion and their breakdown may be approximately described by the Paschen law, similarly to the  $\Phi 5 \times 5$  mm 10 Torr cell for which  $V_B$  seems to match the Paschen curve (c.f. Fig. 38 and 40). This gives very large  $V_B$  values due to the asymptotic limit of the Paschen curves.

The ignition of a discharge below these pressures would be most probably impossible because the use of higher voltages would rather cause sparking between the electrodes around the helium cell.

The breakdown voltage can be increased by oxygen impurities, although the fraction of oxygen in helium necessary for this mechanism to have a visible influence is quite high (0.1%)[31].

The power absorbed at breakdown by the matching network which is actually used in the construction of a magnetometer (c.f. Fig. 27) is a good qualitative illustration of the impact of the described phenomena on the sensor's power consumption. It is presented in Fig. 42.

In conclusion, some limiting values of pressures may be estimated for a stable and low power operation of the discharge for the designed helium magnetometer. Taken the described characteristics, it is convenient to distinguish two such boundaries, mentioned below.

- “Absolute limit” after which the breakdown voltage starts to increase very rapidly and the ignition of a discharge becomes impossible. When approaching this limit, the power necessary for breakdown increases and the discharge becomes unstable (difficult to maintain).
- “Safe operation limit” which allows a stable and low power operation of the discharge.

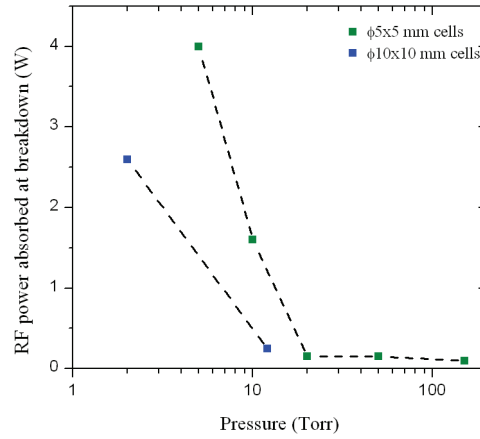


Figure 42. Power absorbed ( $P_{\text{abs}} = P_{\text{Forward}} - P_{\text{Reflected}}$ ) by the matching network of the magnetometer at breakdown ( $f_{\text{RF}} \approx 20$  MHz). Data points connected for clarity.

Such limits for the frequency range used (11-25 MHz) are presented in table 9. Those values are subject to decrease if the frequency range is increased.

Table 9. Low-pressure limits for helium magnetometer cells.

Helium cell dimensions	Absolute limit	Safe operation limit
Φ10x10 mm	6 Torr	10-12 Torr
Φ5x5 mm	10 Torr	20 Torr

## 2.6. Alfa and gamma modes and the high pressure limit

There are two distinct modes of a HF discharge which can be distinguished, based on the mechanism responsible for its maintenance. In weak current ( $\alpha$ ) mode the plasma is maintained by electrons originating from ionizing collisions whereas in the high-current ( $\gamma$ ) mode secondary emission

from the vessel's walls becomes dominant. When the voltage across the cell reaches a certain value an abrupt transition occurs which is followed by a large increase in the current consumed by the discharge (about one order of magnitude). The discharge contracts and the distribution of emitted light changes (c.f. Fig. 43).

Macroscopically this can be explained by the fact that the voltage across the capacitance of the sheaths (c.f. Fig. 25) reaches a value high enough to cause a secondary discharge in their region. The high-current mode is said to be unstable [26]. Right after the  $\alpha$  to  $\gamma$  transition the current consumed by the plasma rises by an order of magnitude.

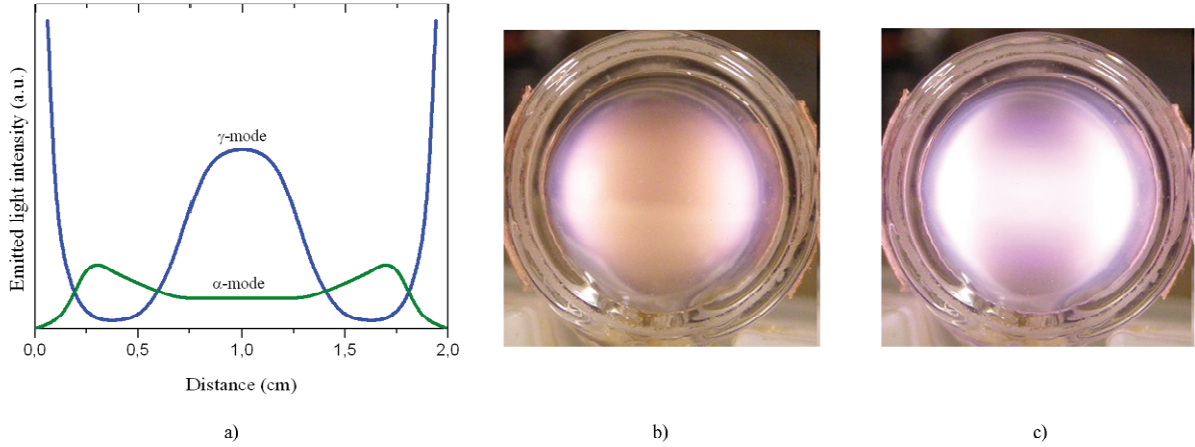


Figure 43. a) Light intensity distribution in  $\alpha$  and  $\gamma$ -modes, data from [26]. b)  $\alpha$ -mode discharge in a 12 Torr 1x1 cm cell at about 200 mW of forward HF power. c)  $\gamma$ -mode discharge in a 12 Torr 1x1 cm cell at about 600 mW of forward HF power.

Both modes were observed in miniature glassblown cells (c.f. Fig. 43b and 43c). The  $\gamma$  mode was found unstable and power consuming. Having in mind the required specifications in terms of stability and power consumption (c.f. §2.1) it is desirable to operate the discharge in the weak current ( $\alpha$ ) mode.

Literature predicts that for certain values of helium pressure and electrode separation, the ignition of the discharge in the  $\alpha$ -mode becomes impossible (c.f. Fig. 44).

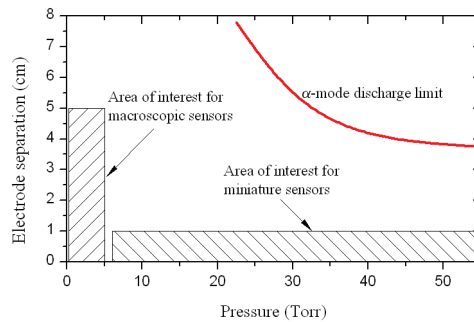


Figure 44. Boundary of the  $\alpha$ -mode discharge. Red curve taken from [26].

In order to stay in the region where the  $\alpha$ -mode is still present, proper pressure and dimension range must be chosen. The presence of  $\alpha$ -mode was confirmed in the area of interest for miniature magnetometers (c.f. Fig. 44) by visual inspection of the light emitted by the discharge in a wide power

range. The  $\gamma$ -mode was found to appear at relatively high power levels (between  $\sim 0.6$  and 2 W) in all of the cells. This leaves a wide power margin for a stable operation of the discharge in the  $\alpha$ -mode because the powers of interest in magnetometry lie near the limit of extinction of the discharge ( $\sim$  tens of mW).

## 2.7. Optimal pressure and its scaling with size

The two main parameters which influence the fundamental sensitivity limit of an atomic magnetometer are the density of magnetically sensitive species and their relaxation time. Size reduction of the active element triggers an inevitable decrease of both. In the case of alkali-vapour magnetometers these two parameters are relatively easy to predict. The species density can be estimated from the alkali vapour pressure (determined using an approximate logarithmic function [32]). By adding literature values of rate constants describing spin relaxation processes simple approximate models, describing the scaling of the maximum sensitivity with size, can be assembled. Such an analysis is more complicated when it comes to helium magnetometers since the two important parameters -  $2^3S_1$  metastable atom density and their relaxation time - are a consequence of multiple complex phenomenons taking place in the discharge. The cells used in the macroscopic version of the sensor (cf. Fig. 22) were filled to 2 Torr of high-purity helium, which was an empirically determined value. In order to maximize the sensitivity of the developed sensor while decreasing the volume of the gas cell, an optimal value of helium pressure needs to be found. In order to determine a reasonable pressure range, an approximate numerical model based on literature was assembled.

### 2.7.1. Metastable density

A very short time after the breakdown a steady state discharge is formed. The number density and physical properties of the metastable population are a result of balance between the mechanisms of their creation and destruction. Here,  $He^*$  stands for helium triplet metastable,  $He^+$  - helium ion,  $e$  - electron,  $He_2^+$  - ionized helium dimer and  $He_2^*$  - helium excimer. The three main mechanisms responsible for the creation of atoms in the metastable state are as follows.

- Electron impact collision with a fundamental state helium atom, according to:  $e+He \rightarrow e+He^*$ . The threshold for this reaction is 19.8 eV, which along with its relatively large cross section makes it the most powerful creation mechanism.
- Electron impact collision with an ionised helium dimer, according to:  $e+He_2^+ \rightarrow He+He^*$ . The influence of this mechanism rises with pressure. The presence of dimers is distinctive to high pressure discharges. The influence of this mechanism is neglected in further analysis.
- Radiative decay from the upper triplet states, the influence of this mechanism is small (relaxation time very short) and thus will be neglected in this study.

The density of metastable species is also determined by the relative influence of the mechanisms leading to the destruction of metastables, summarized below.

- Collisions with walls due to diffusion (drift has no direct influence since metastable atoms have no charge). The probability of reflection upon such collisions is small therefore in this study it will be assumed that all wall collisions destroy  $2^3S_1$  atoms.
- Loss due to collisions with electrons (stepwise ionization) according to:  $e+He^* \rightarrow 2e+He^+$ . The higher becomes the electron density, the higher is the loss. Since electron density depends

proportionally on pressure, the influence of this mechanism is subject to increase in miniature helium cells.

- Penning ionization – collisions between two metastable atoms resulting in the ionization of one of the atoms and de-excitation of the other according to:  $\text{He}^* + \text{He}^* \rightarrow \text{He} + \text{e} + \text{He}^+$ . The influence of this term also increases with pressure.
- Three body collisions [33] of a metastable atom with two atoms in the fundamental state, according to:  $2\text{He} + \text{He}^* \rightarrow \text{He}_2^* + \text{He}$ . Two body collisions are neglected, since they do not influence the triplet metastable population [34].
- Excitation to upper state due to the absorption of pumping light. As discussed in the first chapter the effect of magnetic resonance is amplified by selective optical pumping on the  $D_0$  line. The optical power used in this process is a compromise between two facts: the possibility to detect resonance with appropriate resolution and the destruction of metastables through excitation to upper states which degrades the sensitivity of the magnetometer. The influence of pumping light on metastable density is small since lifetime in the excited state is much smaller to the lifetime in the metastable state ( $\sim 10^{-7}$  s compared to  $\sim 10^{-3}$  s). Therefore this effect will be neglected in the numerical analysis.

### 2.7.1.1. Numerical description

A very reliable picture of all interrelationships in the discharge can be obtained using particle-in-cell or fluid numerical models. Nevertheless, such models, conventionally used in plasma physics, are difficult to assemble and require relatively big computational expense. Since the analysis of optimal pressure value for the sensor does not need to be that much exhaustive, it was chosen to proceed with a simplified zero-dimensional description presented in [35]. It is based on an approximate solution of partial differential equations which describe the mechanism of power dissipation in an HF discharge. It allows to estimate the electron density and temperature at the center of the cell as a function of power absorbed by the discharge. Figure 45 presents a block diagram showing the input data necessary for the calculation.

The metastable density is calculated similarly to ref. [36], although the solution of metastable balance equation is extended to account for three-body collisions.

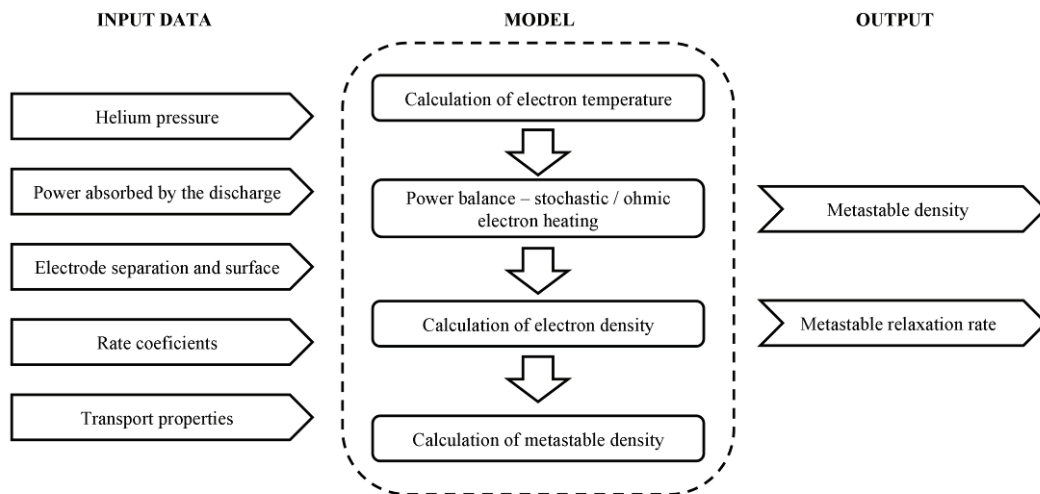


Figure 45. Block diagram presenting the input data necessary for the calculation.

## 2.7.1.1.1. Initial assumptions

- The model describes a capacitively coupled helium plasma source at a pressure range of 5 – 200 Torr. The electrode separation ( $d$ ) is between 5 and 10 mm.
- The discussed discharge is highly collisional since the condition expressed by Eq. 24 is satisfied.

$$\lambda_i \leq \left( \frac{T_i}{T_e} \right) d \quad (24)$$

where:  $\lambda_i$  – ion mean free path, defined as  $\lambda_i = 1/\sigma_{mi}n_g \approx (3.1 \cdot 10^{-5} - 8 \cdot 10^{-7} \text{ m})$  [37],

$T_i$  – ion temperature,  $T_i = 300 \text{ K} \approx 0.026 \text{ eV}$ ,

$T_e$  – electron temperature,  $T_e = (4 - 2 \text{ eV})$ ,

$d$  – electrode spacing.

- The sheaths are considered collisional [38].
- The distribution of metastable density is identical to the distribution of electron density.
- The rate constants used in the calculation are presented in table 10.

Table 10. Rate constants of reactions included in the model.  $T_e$  is in eV units.

Reaction			$k \text{ (cm}^3/\text{s)}$	Ref.
Formula	Type			
$k_{el}$	$e + \text{He} \rightarrow e + \text{He}$	Elastic	$5.02 \cdot 10^{-8} \sqrt{T_e}$	[39]
$k_1$	$e + \text{He} \rightarrow 2e + \text{He}^+$	Ionisation	$1.50 \cdot 10^{-9} T_e^{0.31} \exp(-24.56/T_e)$	[40]
$k_2$	$e + \text{He} \rightarrow e + \text{He}^*$	Excitation	$4.20 \cdot 10^{-9} T_e^{0.31} \exp(-19.80/T_e)$	[40]
$k_3$	$e + \text{He}^* \rightarrow 2e + \text{He}^+$	Stepwise ionisation	$1.28 \cdot 10^{-7} T_e^{0.6} \exp(-4.78/T_e)$	[41]
$k_6$	$\text{He}^* + \text{He}^* \rightarrow \text{He} + e + \text{He}^+$	Penning ionisation	$2.70 \cdot 10^{-10}$	[42]
$k_7$	$2\text{He} + \text{He}^* \rightarrow \text{He}_2^* + \text{He}$	Three-body	$2.00 \cdot 10^{-34} \text{ (cm}^6/\text{s)}$	[40]

The transport properties used are collected in table 11.

Table 11. Transport properties used in the calculation.  $D$  – diffusion coefficient.  $\mu$  – mobility.  $p$  – pressure in Torr.

$x$	Particle	Symbol	$D_x \text{ (m}^2/\text{s)}$	$\mu_x \text{ (m}^2/\text{Vs)}$	Reference
e	Electron	e	$1.737 \cdot 10^{-1} (T_e/17406)^{(760/p)^S}$	$1.132 \cdot 10^{-1} (760/p)$	
i	Ion	$\text{He}^+$	$5.026 \cdot 10^{-5} (760/p)$	$1.482 \cdot 10^{-3} (760/p)$	[38]
m	Metastable( $2^3\text{S}$ )	$\text{He}^*$	$4.70 \cdot 10^{-2}/p$	- (no charge)	

<sup>S</sup> $T_e$  in Kelvin units.

## 2.7.1.1.2. Solving methodology

The set of equations presented below is implemented in MATLAB<sup>®</sup>. The program uses several constant parameters taken from literature (c.f. tables 10 and 11). Apart from that, the values of the electron density at the sheath edge ( $n_s$ ) and the sheath thickness ( $d_s$ ) are necessary in order to carry out the calculation. An approach suggested in ref. [35] is used, consisting of setting an initial value of both

and iterating the solving algorithm. The number of iterations needed to obtain a steady solution (a one which does not change from one iteration to another) depends on how close the initial guess is to the real value. Using a properly chosen value, the number of iterations can be limited to four which significantly accelerates the algorithm.

The values of power at the limit of extinction of the discharge were used. Since the values of extinction power vary slightly with pressure, mean values of 5 mW and 4 mW for  $\Phi 5 \times 5$  mm and  $\Phi 10 \times 10$  mm cells respectively were used. These values take into account the 50% power transfer from the generator to the discharge (c.f. §2.4.3).

#### 2.7.1.1.3. Electron temperature

The first parameter to calculate is the electron temperature, which is a thermodynamic equivalent of the electron energy, used in plasma physics. It is expressed in electron-volt (eV) units and comprised between 4 and 1.5 eV. Electron temperature at the center of the bulk plasma can be described with Eq. 25 [35], where  $k_I$  and  $u_s$  are functions of  $T_e$ .

$$\frac{\sqrt{k_{mi}k_I}}{u_s} = \frac{\pi}{n_g l} \quad (25)$$

where:  $k_{mi}$  – ion-neutral atom collision rate coefficient,  $k_{mi} = 1 \cdot 10^{-17}$ ,  
 $k_I$  – ionization rate coefficient,  
 $n_g$  – neutral atom density,  $n_g = 3.2 \cdot 10^{22} \cdot p$  ( $m^{-3}$ ), with  $p$  – pressure in Torr.

The velocity of an ion entering the sheath ( $u_s$ ) is defined with Eq. 26. Since the sheath is considered collisional  $u_s$  will decrease strongly with pressure.

$$u_s = \sqrt{\frac{\frac{eT_e}{m_{He}}}{1 + \pi \frac{\lambda_{Ds}}{\lambda_i}}} \quad (26)$$

where:  $m_{He}$  – helium atom mass,  $m_{He} = 6.647 \cdot 10^{-27}$  kg.

The Debye length at sheath edge ( $\lambda_{Ds}$ ) is defined by Eq. 27:

$$\lambda_{Ds} = \sqrt{\frac{\epsilon_0 T_e}{en_s}} \quad (27)$$

where:  $n_s$  – electron density at sheath edge,  
 $\epsilon_0$  – vacuum permittivity.

The bulk plasma thickness ( $l$ ) is defined by Eq. 28:

$$l = d - 2d_s \quad (28)$$

where:  $d$  – electrode separation,



$d_s$  – sheath thickness.

The sheath thickness ( $d_s$ ) is expressed by Eq. 29:

$$d_s = (\lambda_{De}^2 l)^{1/3} \quad (29)$$

with  $\lambda_{De}$  being the Debye length in the bulk plasma, expressed as ( $T_e$  in eV):

$$\lambda_{De} = \sqrt{\frac{\epsilon_0 T_e}{en_e}} \quad (30)$$

where:  $n_e$  – electron density at the center of the discharge.

The above set of equations is numerically solved for  $T_e$  for given values of  $n_g l$ . As suggested in ref. [35], equations are iterated several times in order to obtain more accurate value of  $d_s$  (initial estimate of  $\sim 1$  mm).

#### 2.7.1.1.4. Electron density

Electron density is calculated from the power dissipated into the discharge. This power can be expressed approximately with Eq. 31 [35].

$$S_{abs} \approx (\bar{S}_{ohm} + 2\bar{S}_{Stoc}) \left( 1 + \frac{0.78V_s}{\epsilon_c + V_s + 2.5T_e} \right) \quad (31)$$

where:  $S_{abs}$  - density of power dissipated into the discharge,  
 $V_s$  - voltage across the sheath capacitance,  
 $\epsilon_c$  - collisional energy loss expressed with Eq. 32.

$$\epsilon_c = \frac{k_1 24.56 + k_2 19.8 + 3k_{el} T_e (m_e / m_{He})}{k_1} \quad (32)$$

$\bar{S}_{ohm}$  and  $\bar{S}_{Stoc}$  represent the two mechanisms of electron heating, respectively :

- Ohmic – heating in the bulk plasma due to collisions between electrons and neutral He atoms. It accounts for the resistive part of the discharge electrical equivalent model (c.f. Fig. 25).
- Stochastic – heating at the bulk/sheath edge, it represents the reflection of electrons from the sheath due to its large decelerating electric field (c.f. the capacitance  $C_{sh}$  in Fig. 25). This mechanism is negligible at the pressure range of interest.

Those mechanisms are expressed by Eq. 33 and 34.

$$\bar{S}_{ohm} \approx 1.73 \frac{m_e}{2e} \frac{n_s}{n_e} \epsilon_0 \omega^2 k_{el} n_g \sqrt{T_e V_s} \frac{2}{\beta} \ln[\tan(0.25(\pi + \beta l))] \quad (33)$$

where:  $\cos(\beta l/2) = n_s/n_e$ ,



$$\bar{S}_{Stoc} \approx 0.61 \sqrt{\frac{m_e}{e}} \epsilon_0 \omega^2 \sqrt{T_e} V_s \quad (34)$$

The ratio of  $n_s/n_e$  is given by Eq. 35.

$$\frac{n_s}{n_e} = \sqrt{1 + (lu_s / \pi D_a)^2} \quad (35)$$

with:  $D_a$  – ambipolar diffusion coefficient,  $D_a = \frac{\mu_i D_e + \mu_e D_i}{\mu_i + \mu_e}$

The value of  $V_s$  is evaluated numerically from Eq. 31, once the power absorbed into the discharge is known. Finally, the electron density at the center of the discharge is calculated using Eq. 36 [35].

$$n_e = \frac{S_{abs}}{2eu_s (\epsilon_c + V_s + 2.5T_e) \sqrt{1 + (lu_s / \pi D_a)^2}} \quad (36)$$

The resulting values of  $n_e$  are in the range of  $10^9$  (cm<sup>-3</sup>).

#### 2.7.1.1.5. Metastable density

The value of metastable density is a result of a balance between the processes of their creation and destruction. It is described by Eq. 37.

$$-D_m \nabla^2 n_m = k_2 n_g n_e - k_3 n_m n_e - k_6 n_m^2 - k_7 n_g^2 n_m \quad (37)$$

where:  $n_m$  – metastable density,  
 $n_g$  – fundamental-state helium atom density.

This equation is solved for  $n_m$  using a numerical algorithm presented in ref. [36]. Equation 38 is a simplified form of the numerical solution obtained.

$$n_m = \frac{1.63 \cdot 10^{17} D_m}{4.7 \cdot 10^{16} r^2 k_6 n_e} - 2.8 \cdot 10^{16} \left( \frac{n_g^2 r^2 k_7 + r^2 k_3 n_e}{4.7 \cdot 10^{16} r^2 k_6 n_e} + \sqrt{\frac{320 D_m^2 + 12 n_g^2 r^2 k_7 + 10 D_m r^2 k_3 n_e + n_g^4 r^4 k_7^2 + 1.7 n_g^2 r^4 k_3 k_7 n_e + 3.4 k_2 k_6 n_g r^4 n_e + 0.7 r^4 k_3^2 n_e^2}{4.7 \cdot 10^{16} r^2 k_6 n_e}} \right) \quad (38)$$

where:  $r$  – radius of the cell.

#### 2.7.1.2. Experimental validation

At this point it is necessary to compare the theoretical values, obtained with the previous set of equations with experimental values. Metastable atom density was measured by means of absorption spectroscopy. After a short presentation of the experimental methods, the measured values will be compared with theoretical ones, calculated using Eq. 38.

### 2.7.1.2.1. Absorption measurement – determination of the metastable density

Metastable density can be measured by means of absorption spectroscopy, where a laser beam with wavelength exactly matching the D<sub>0</sub> line (c.f. Fig. 2) is passed through the discharge ignited inside the cell (c.f. Fig. 46). In such a setup, absorption is defined as:

$$Abs = \frac{I_0 - I_T}{I_0} \quad (39)$$

where:  $I_0$  – intensity of light transmitted through the cell with the discharge “off”,  
 $I_T$  – intensity of light transmitted through the cell with the discharge “on”.

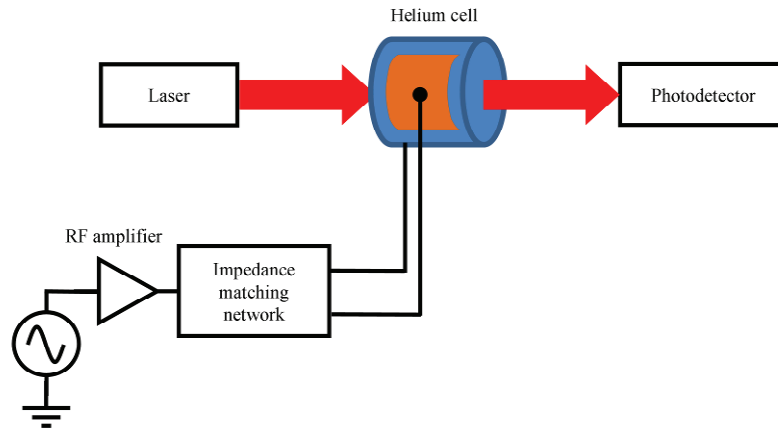


Figure 46. Absorption measurement setup.

The intensity of light transmitted through the discharge can be described by the Beer-Lambert law (c.f. Eq. 40).

$$I_T = I_0 \exp(-k_v l_{opt}) \quad (40)$$

where:  $l_{opt}$  – effective optical path,  $l_{opt} = 1.22r$  [43], with  $r$  – radius of the cell,  
 $k_v$  – absorption coefficient.

The value of the absorption coefficient ( $k_v$ ) depends on the relative detuning of wavelength of light from the value corresponding to the energy separation of interest (He D<sub>0</sub> line). This dependence is shown in Fig. 47a.

As a consequence the absorption is highly dependent on the detuning (c.f. Fig. 47b). During the measurement, the temperature of the laser diode (and thus the emitted wavelength) was adjusted to obtain a maximum of absorption. Therefore, taking into account the small linewidth of the emitted light (2 MHz), it can be considered that the absorption is always at its maximum ( $k_v = k_{max}$ ).

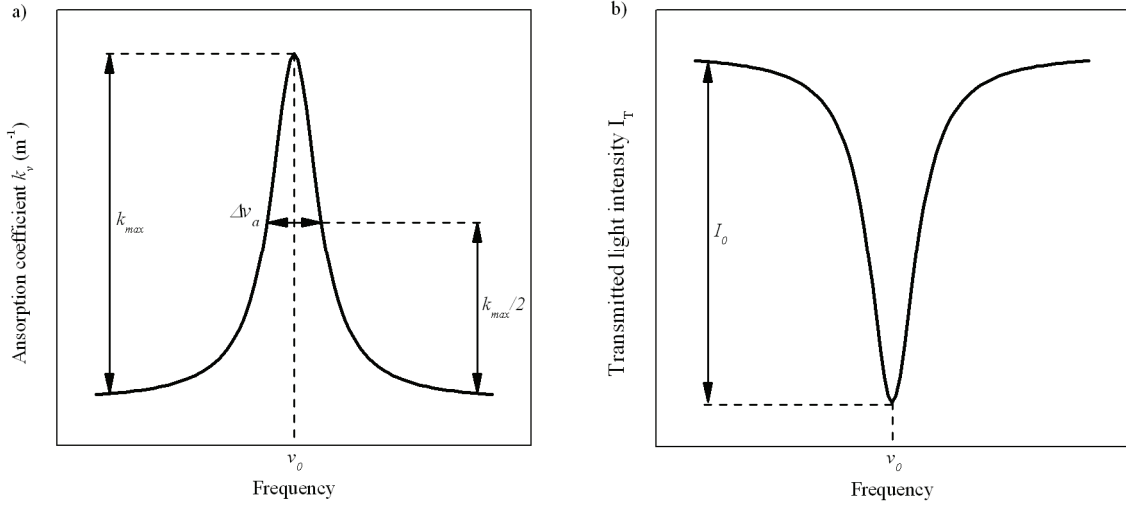


Figure 47. a) The dependence of the absorption coefficient on the frequency (wavelength) of light based on [44]. b) Transmitted light as a function of frequency (wavelength), based on [44].

In such case, under the assumption that the linewidth of the absorption is only broadened by Doppler effect, the absorption coefficient can be expressed by Eq. 41 [44].

$$k_{\max} = \frac{2}{\Delta \nu_a} \sqrt{\frac{\ln 2}{\pi}} \frac{\pi e^2 k_e}{m_e c} n_m f_T \quad (41)$$

where:  $k_e$  – Coulomb constant,  $k_e = 8.987 \cdot 10^9$  (m/F),  
 $f_T$  – oscillator strength of the transition,  $f_T = 0.06$  for the  $D_0$  transition,  
 $c$  – speed of light.

The linewidth of the absorption line ( $\Delta \nu_a$ ) can be expressed by Eq. 42 [44].

$$\Delta \nu_a = \frac{2\sqrt{2 \ln 2}}{\lambda_{D_0}} \sqrt{\frac{k_B T}{m_{He}}} = 1.71 \cdot 10^9 \text{ (Hz)} \quad (42)$$

where:  $T$  – temperature,  $T = 300$  K,  
 $\lambda_{D_0}$  – wavelength of the  $D_0$  transition,  $\lambda_{D_0} = 1083$  nm.

Therefore by rearranging Eq. 41, the following expression (Eq. 43) can be obtained, which allows to calculate the metastable atom density from the absorption measurement.

$$n_m = \frac{\Delta \nu_a}{2} \sqrt{\frac{\pi}{\ln 2}} \frac{m_e c}{\pi k_e e^2} \frac{k_{\max} l_{opt}}{f l_{opt}} = 1.15 \cdot 10^{12} \frac{k_{\max} l_{opt}}{l_{opt}} \quad (43)$$

The parameter  $k_{\max} l_{opt}$  can be determined from the Ladenbourg-Reiche curve as a function of absorption. Such curves are plotted using the  $\alpha$  parameter, which is the ratio of the linewidth of the optical source used to the linewidth of the absorption curve. Since a laser diode is used it may be considered that  $\alpha = 0$ . The curve is presented in Fig. 48.

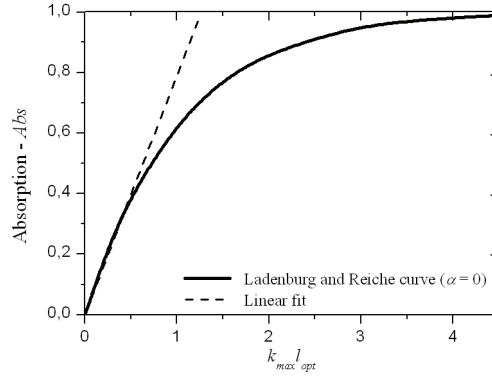


Figure 48. Ladenburg and Reiche curve and a linear fit.

The linear fit from Fig. 48 allows to express Eq. 43 directly in terms of absorption ( $Abs$ ) with Eq. 44, which will be valid in the range of absorption from 0 to 40%.

$$n_m = 1.15 \cdot 10^{12} \frac{k_{\max} l_{opt}}{l_{opt}} \approx 1.15 \cdot 10^{12} \frac{Abs}{0.79 l_{opt}} \quad (44)$$

For higher values of absorption the Ladenburg-Reiche curve has to be used.

#### 2.7.1.2.2. Absorption measurement – results

Optical absorption of the discharge was measured using the setup presented in Fig. 46, and the impedance matching network from the SWARM project (c.f. Fig. 26). The absorbed power is measured with a bidirectional power meter at the input of the matching network. As discussed in §2.4.2 and §2.4.3, the power actually dissipated into the discharge is approximately 25% of power measured in this configuration.

Figure 49a presents the results of the absorption measurement as a function of total absorbed power for  $\Phi 5 \times 5$  mm cells.

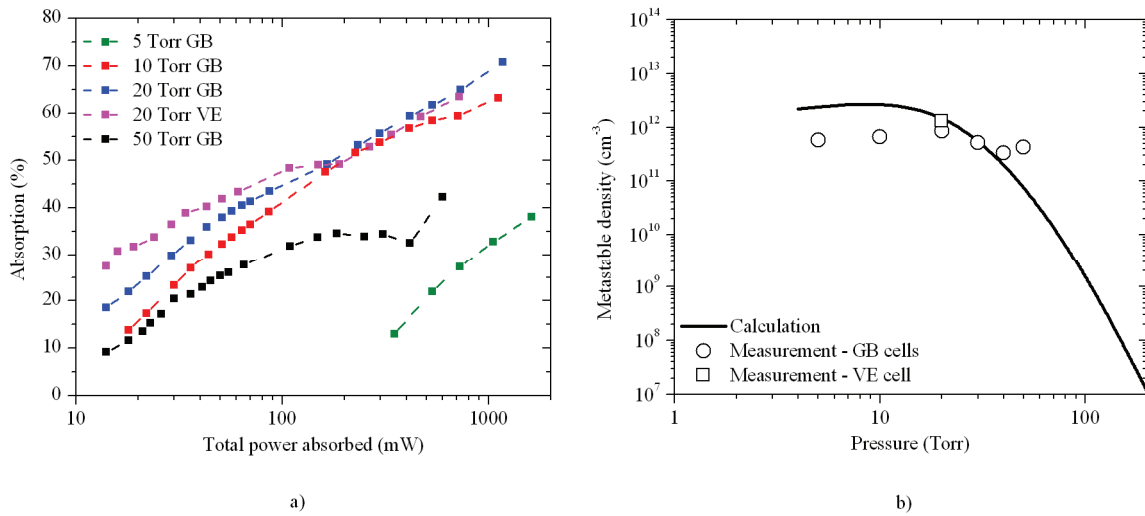


Figure 49. Absorption measurement results  $\Phi 5 \times 5$  mm cells. a) Absorption as a function of power absorbed by the discharge. Data points connected for clarity. b) Values of metastable density at the extinction limit as a function of pressure. Solid curve – issued from the previously described model for 5 mW of power dissipated into the discharge.

The metastable densities were calculated from the values of absorption at the limit of extinction of the cells (the area of actual interest in magnetometry) using Eq. 44. Results are presented in Fig. 49b. The solid curve is issued from the previously described numerical model (c.f. §2.7.1.1). The same set of results for  $\Phi 10 \times 10$  mm cells is presented in Fig. 50a and 50b.

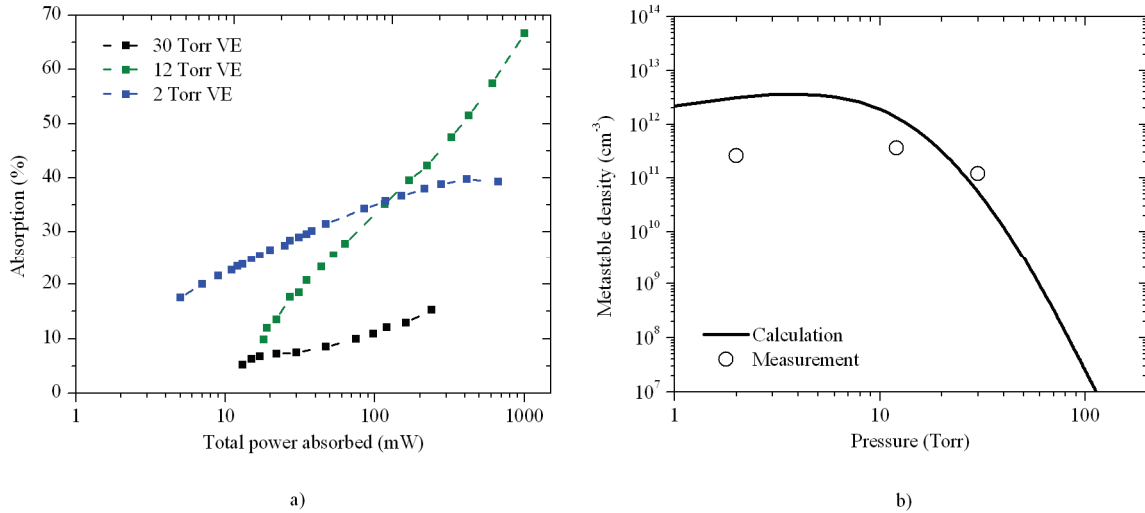


Figure 50. Absorption measurement results  $\Phi 10 \times 10$  mm cells. a) Absorption as a function of power absorbed by the discharge. Data points connected for clarity. b) Values of metastable density at the extinction limit as a function of pressure. Solid curve – issued from the previously described model for 4 mW of power dissipated into the discharge.

The numerical values of the metastable density measured at the limit of extinction are presented in table 12.

Table 12. Numerical values of the metastable densities calculated from absorption measurements.

Dimensions	Helium pressure (Torr)	Supplier	Absorption (%)	Metastable density (cm <sup>-3</sup> )
$\phi 10 \times 10$ mm	2	VE	11	$2.6 \times 10^{11}$
$\phi 10 \times 10$ mm	12	VE	15	$3.6 \times 10^{11}$
$\phi 10 \times 10$ mm	30	VE	5	$1.2 \times 10^{10}$
$\phi 5 \times 5$ mm	5	GB	12	$5.7 \times 10^{11}$
$\phi 5 \times 5$ mm	10	GB	14	$6.7 \times 10^{11}$
$\phi 5 \times 5$ mm	20	GB	18	$8.6 \times 10^{11}$
$\phi 5 \times 5$ mm	30	GB	11	$5.2 \times 10^{11}$
$\phi 5 \times 5$ mm	40	GB	7	$3.3 \times 10^{11}$
$\phi 5 \times 5$ mm	50	GB	9	$4.3 \times 10^{11}$
$\phi 5 \times 5$ mm	20	VE	27	$1.3 \times 10^{12}$

### 2.7.1.3. Distribution of metastable atoms

The decrease in metastable density above 20 Torr for 5 mm cells and above 10 Torr for 10 mm cells (see Fig. 49b and 50b respectively) predicted by the theoretical model is related with the electron temperature in the discharge which decreases with pressure. Unfortunately the theoretical model,

which describes the center of the discharge, is not capable to fully reflect the complexity of the problem, since electron temperature has in fact a spatial distribution. It generally reaches the highest value at the sheath-bulk boundary [45], where the majority of ionization and excitation occurs. Metastable density exhibits similar behavior after certain values of pressure and electrode separation. Figure 51 presents such a behavior for a He/O<sub>2</sub>/N<sub>2</sub> plasma at atmospheric pressure (780 Torr) [45].

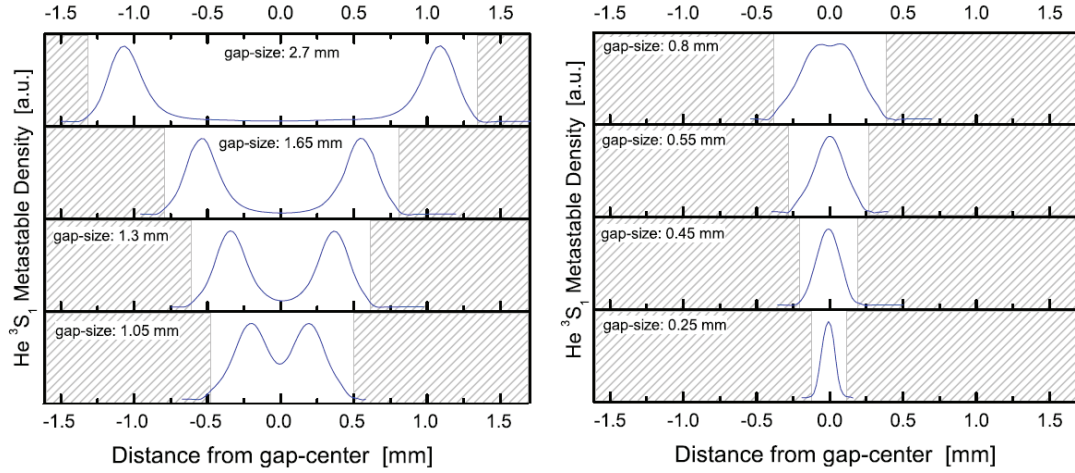


Figure 51. Metastable density distribution in an atmospheric pressure He/O<sub>2</sub>/N<sub>2</sub> plasma for various electrode separation (gap-size) values [45].

In order to inspect the metastable density distribution, the profile of optical absorption on the D<sub>0</sub> line was measured. The principle of measurement is presented in Fig. 52.

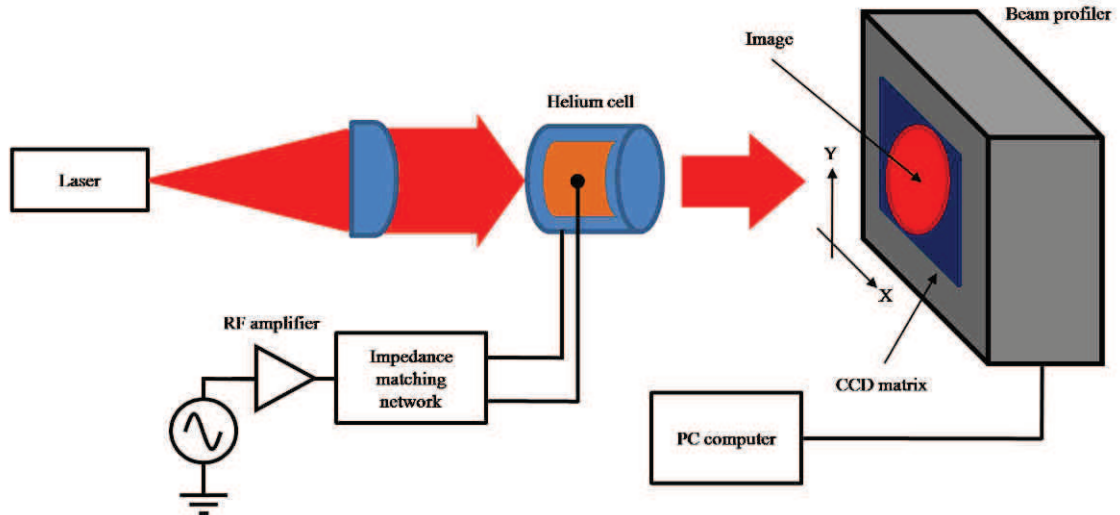


Figure 52. Metastable density profile measurement setup.

A laser beam profiler (Thorlabs BC106-VIS) is used in order to measure the profile. Profiles of the beam with and without the discharge were captured and processed under Matlab to give absorption profiles (c.f. Eq. 39).

The obtained profiles are quite noisy due to the noise of the CCD matrix used in the beam profiler, therefore they were filtered with a Savitzky-Golay filter. The resulting characteristics are presented in Fig. 53.

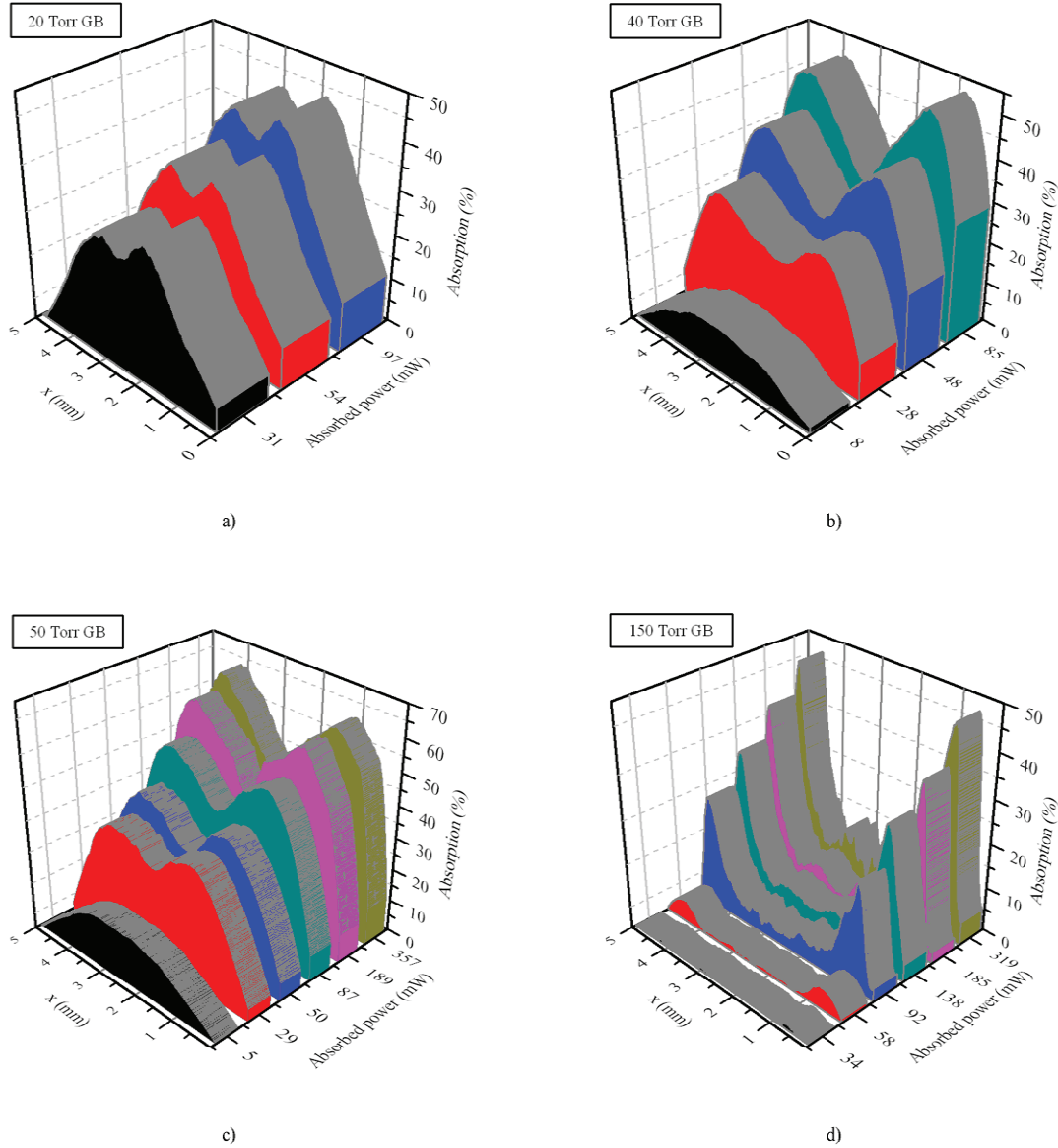


Figure 53. Measured metastable density profiles for a  $\Phi 5 \times 5$  mm GB cells. a) 20 Torr. b) 40 Torr. c) 50 Torr. d) 150 Torr.

A similar tendency to the one suggested by the state of the art (c.f. Fig. 51) is clearly visible. The metastable density profile seems to change with the applied HF power while maintaining its maximum at the center for powers close to the extinction limit of the cell (which is not the case for the 150 Torr cell in the detection limit).



#### 2.7.1.4. Comparison between the distribution of metastable atoms and emitted light intensity

The distribution of light, emitted by the discharge was found to change in a manner similar to the previously described metastable density. For higher values of pressure (or power) the emitted light is more intense near the electrodes. This situation is much more clearly visible in larger cells. It is presented in Fig. 54 for the case of the  $\Phi 10 \times 10$  mm 12 Torr cell.

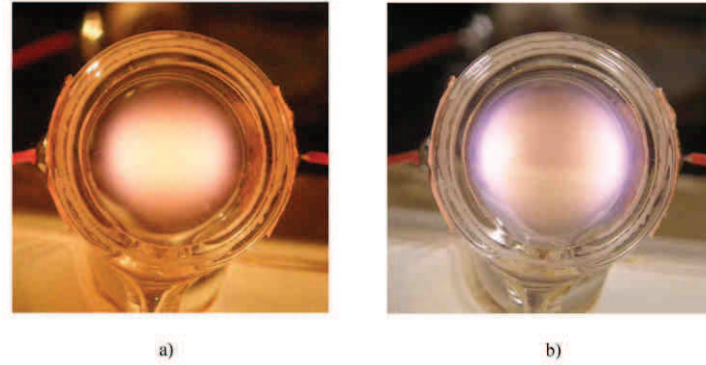


Figure 54. Discharge ignited in a  $\Phi 10 \times 10$  mm 12 Torr helium cell. a) Near the extinction limit ( $\sim 20$  mW of forward power). b) At about 150 mW of forward power.

Since the measurement described in §2.7.1.3 was impossible for  $\Phi 10 \times 10$  mm cells due to the small aperture of the beam profiler, it was chosen to study the relationship between the two distributions (absorption at the  $D_0$  line and distribution of light emitted by the discharge) at the example of the  $\Phi 5 \times 5$  mm 40 Torr cell. For this purpose the emitted light intensity needs to be measured. Because of the small dimensions of the cell, it was chosen to recover the intensity distribution from a high-resolution photograph of the discharge rather than developing a dedicated measurement setup (focusing optics). This procedure is presented in Fig. 55.

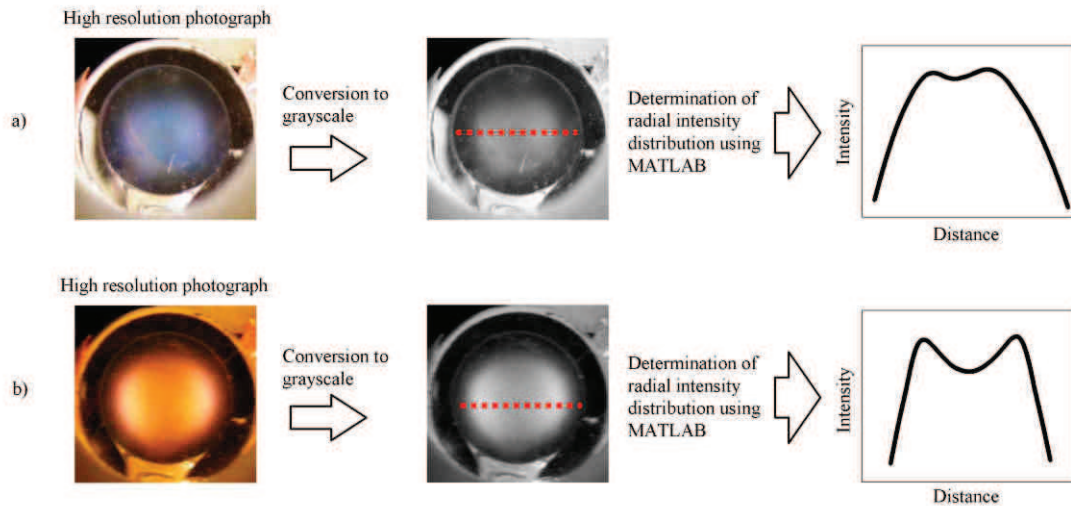


Figure 55. The procedure used to determine the distribution of intensity of light emitted by the discharge. a) discharge maintained in a  $\Phi 5 \times 5$  mm 40 Torr cell with 8 mW of absorbed power. b) The same discharge at 85 mW of absorbed power.

The results of the comparison of these distributions with the absorption profiles (c.f. Fig. 53) are presented in Fig. 56. A clear relationship is visible between the two, which leads to suggest that a



visual inspection of the discharge (of the emitted light intensity distribution) may provide some information on the metastable population distribution inside the cell.

This comparison is not intended to draw any far-reaching physical conclusions, since those would require more precise experimental methods. It provides a simple method of approximate determination of the topology of the metastable population inside the cell.

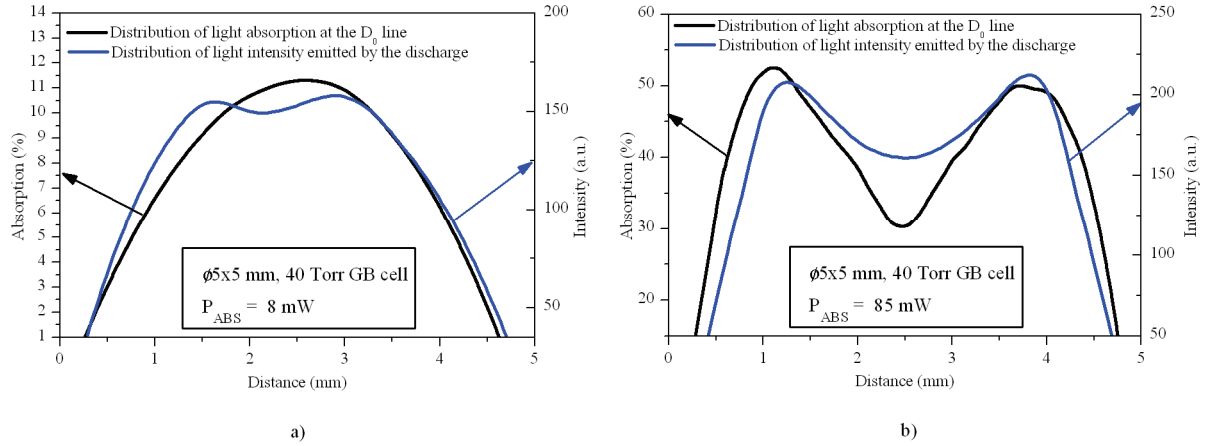


Figure 56. Comparison between the profile of metastable density and the distribution of light emitted by the discharge for a  $\phi 5 \times 5$  mm 40 Torr cell. a) 8 mW of absorbed power. b) 85 mW of absorbed power.

### 2.7.1.5. Conclusion

A numerical description of metastable density as a function of helium cell dimensions, pressure and power dissipated into the discharge has been presented. The agreement between the theoretical description and experiment is quite good. The predicted pressure ranges in which the metastable density starts to decrease correspond fairly well to the gathered data. However the decrease predicted theoretically is much sharper to the one given by experiment. This can be attributed to the changing profile of the metastable atom distribution. For higher values of pressure the metastable density becomes higher near the electrodes and decreases towards the center of the discharge.

The metastable densities obtained at the limit of extinction for two  $\phi 5 \times 5$  mm 20 Torr cells provided by different suppliers show quite different values. For the GB the metastable density is approximately 30 % lower as compared to the VE cell. This is attributed to the oxygen impurity resulting from the filling process (c.f. §2.3).

### 2.7.2. Metastable relaxation

The relaxation time of metastable atoms is the second most important parameter, resulting from the physics of the discharge, which directly influences the sensitivity of helium magnetometers. This section is dedicated to its analytical description, which will be backed by experimental measurements.

### 2.7.2.1. Collisional and transverse relaxation times

Collisional relaxation time describes the lifetime of helium atoms in the metastable state. Therefore it is a sum over all processes leading to its destruction, which take place in the plasma. It includes three fundamental mechanisms.

- Diffusion loss – related to the gradient of concentration and collisions with the walls of the glass cell.
- Loss due to collisions with other species present in the plasma, like electrons, fundamental state helium atoms and other metastable atoms.
- Quenching by impurities – this mechanism is very difficult to describe analytically since their exact composition and concentration is unknown. It will not be taken into account by the theoretical description although its influence will be illustrated in the experimental part of this section.

Given the above definition, the collisional relaxation time of  $2^3S_1$  metastable helium-4 atoms can be described by Eq. 45.

$$\frac{1}{\tau_R} = D_m \Lambda^{-2} + k_3 n_e + k_6 n_m + k_7 n_g^2 \quad (45)$$

The transverse relaxation time  $\tau_2$  of actual interest in magnetometry describes the spin relaxation processes. It is related with the collisional relaxation time with Eq. 46.

$$\frac{1}{\tau_2} = \frac{1}{\tau_R} + \Phi_{in} Q_{B2} \exp(Abs) = \frac{1}{\tau_R} + \Phi_{in} Q_{B2} \exp(n_m Q_A r) \quad (46)$$

Where:  $\Phi_{in}$  – incident photon flux,

$Q_A$  – absorption cross section,  $Q_A \approx 8.4 \cdot 10^{-13} \text{ (cm}^2\text{)}$  in the domain of validity of Eq. 44,

$r$  – radius of the cell.

The second term in Eq. 46 accounts for the influence of pumping light on the resonance linewidth. The light broadening cross section ( $Q_{B2}$ ) can be expressed with Eq. 47. for the pumping conditions of interest (pumping on the  $D_0$  line with linearly polarized light,  $\vec{B}_0 \perp \vec{E}_0$ ) [46][7][6].

$$Q_{B2} = \frac{2}{3} \frac{\sqrt{\pi^3} (2.5312ea_0)^2}{\hbar \sqrt{\frac{2k_B T}{m_{He}}}} \approx 1.3 \cdot 10^{-12} \text{ (cm}^2\text{)} \quad (47)$$

Where:  $a_0$  – Bohr radius.

### 2.7.2.2. Collisional relaxation time measurement

Literature [5][33] suggests a measurement scheme consisting of a “pulsed discharge”, where the HF signal driving the plasma is amplitude modulated with a square thus giving a discharge which is ignited and extinguished alternately. Using this method the measurement cannot be done for powers smaller than the value of power required for the ignition of the discharge. The powers of practical interest for magnetometry lie close to the smallest power necessary to maintain the plasma (which is in general a lot smaller than the breakdown power). For that reason a modified measurement procedure

was adopted. Its principle is presented in Fig. 57. It uses an amplified HF signal to ignite and maintain a stable discharge in the helium cell. Once all the parameters are fixed the oscilloscope is set into single sequence mode. When the signal is cut off with the use of a relay switch, a rising curve is caught by the oscilloscope (c.f. Fig. 57). The method of cutting off the signal is quite important in this case, since it must allow a fast and repetitive disconnection of the circuit so as not to introduce additional errors to the measurement. The simplest solution consists of cutting off the signal with the use of an electrically operated relay. Moreover, these devices suffer from a phenomenon called “contact bounce”. Due to elastic force, disconnected contacts bounce back and forth short after they have been disconnected. This may produce a distortion in the output signal. Such distortions were found in the electrical signal measured directly after the relay switch yet no noticeable influence was found on the photodiode signal.

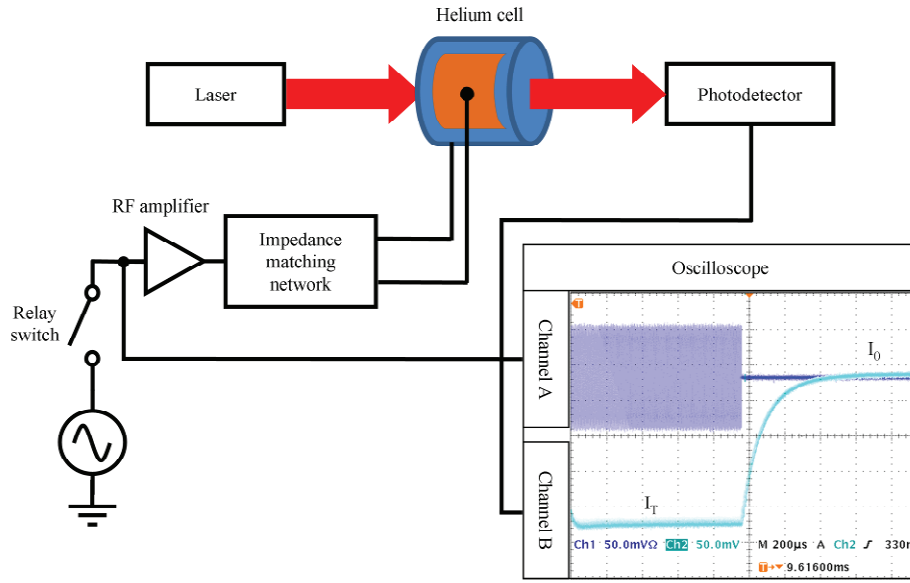


Figure 57. Measurement setup. Measurement of collisional relaxation time in the afterglow of a helium discharge.

In the afterglow of the discharge, the evolution of the metastable density can be described with Eq. 48.

$$n_m(t) = n_{m0} \exp(-t / \tau_R) \quad (48)$$

where:  $n_{m0}$  – initial metastable density (at  $t = 0$ ).

In the domain of validity of Eq. 44, it can be expressed in terms of absorption using Eq. 49.

$$Abs(t) = Abs_0 \exp(-t / \tau_R) \quad (49)$$

where:  $Abs_0$  – initial value of absorption density (at  $t = 0$ ).

The experimental curves, measured in the setup from Fig. 57, represent the evolution of light intensity with time. They were recalculated using Eq. 39 to give absorption evolution profiles. These profiles were fitted with Eq. 49 in order to determine the values of  $\tau_R$ . This procedure is presented in Fig. 58.

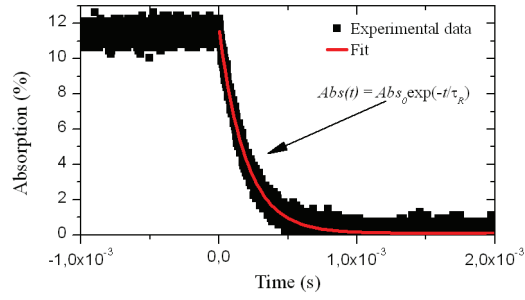


Figure 58. The measured evolution of absorption in the afterglow of a helium discharge and fitted function.

The collisional relaxation time measurements, gathered for several values of initial HF power (before cut off) are presented in Fig. 59a and 60a for  $\Phi 10 \times 10$  mm and  $\Phi 5 \times 5$  mm cells respectively.

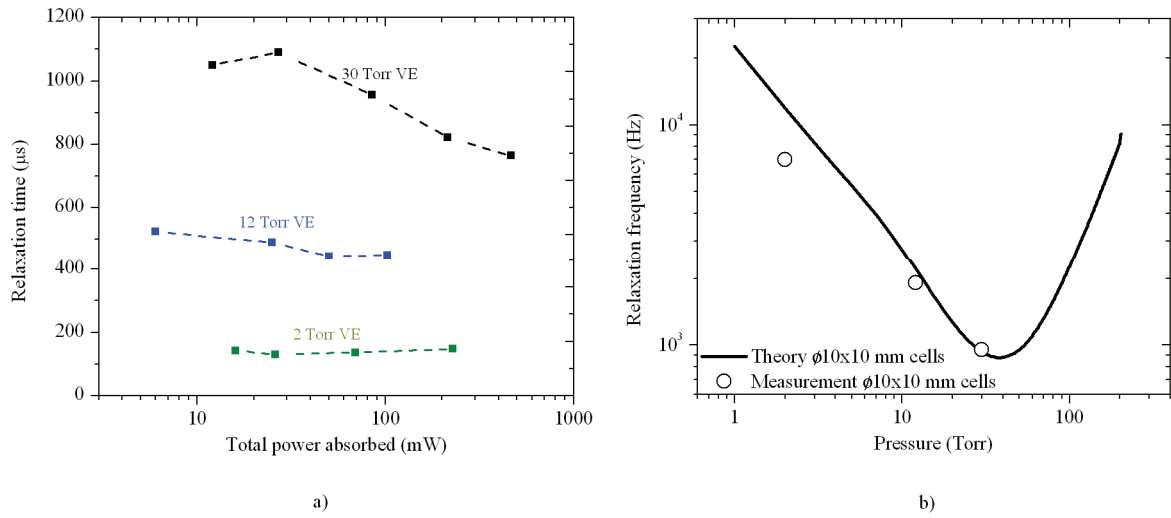


Figure 59. a) Relaxation time measured in the afterglow of discharges in three  $\Phi 10 \times 10$  mm VE cells. Data points connected for clarity. b) Values of relaxation frequency at the extinction limit as a function of pressure. Solid curve – issued from the previously described model for 4 mW of power dissipated into the discharge.

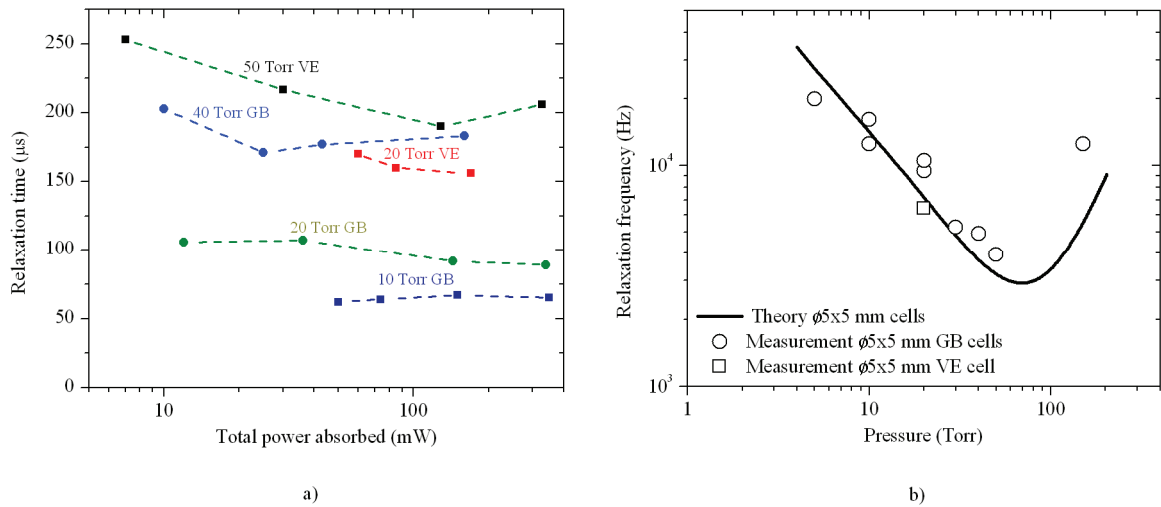


Figure 60. a) Relaxation time measured in the afterglow of discharges in  $\Phi 5 \times 5$  mm cells. Data points connected for clarity. b) Values of relaxation frequency at the extinction limit as a function of pressure. Solid curve – issued from the previously described model for 5 mW of power dissipated into the discharge.

A comparison between values measured at the extinction limit and ones calculated with the numerical model using Eq. 45 are presented in Fig. 59b and 60b for  $\Phi 10 \times 10$  mm and  $\Phi 5 \times 5$  mm cells respectively.

The contributions of the four metastable atom destruction mechanisms (c.f. Eq. 45) to the value of collision frequency calculated by the numerical model are presented for  $\Phi 5 \times 5$  mm and  $\Phi 10 \times 10$  mm cells in Fig. 61a and 61b respectively.

Two main mechanisms responsible for the destruction of metastable atoms can be identified. Namely the diffusion and quenching to the walls, which is dominant at low pressures and three-body collisions with neutral helium atoms at higher values of pressure. The influence of other terms seems less pronounced.

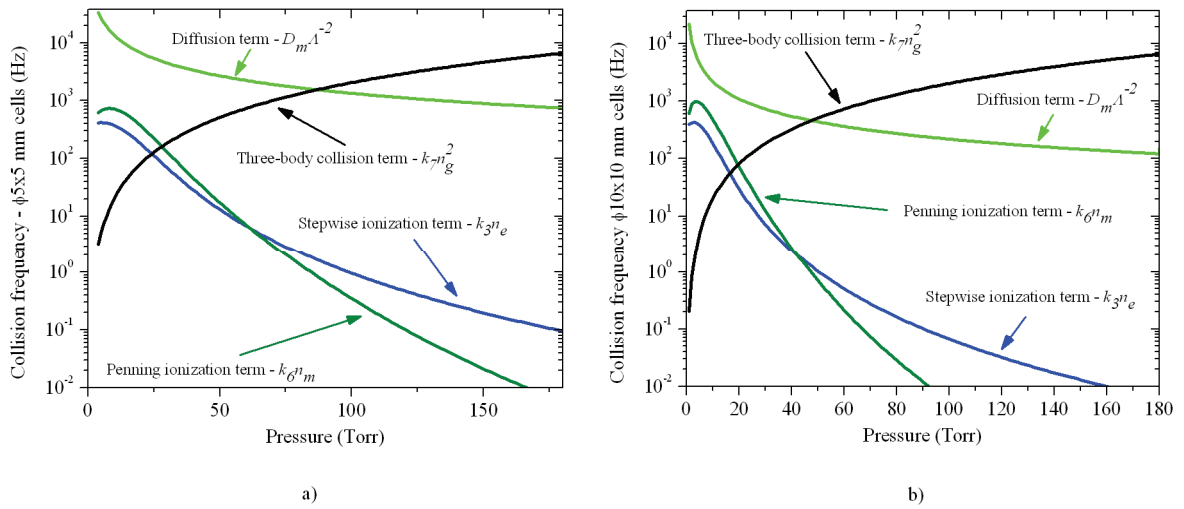


Figure 61. Contributions of four metastable atom destruction mechanisms to the value of the collisional relaxation time calculated by the numerical model. a)  $\Phi 5 \times 5$  mm cells. b)  $\Phi 10 \times 10$  mm cells.

### 2.7.2.3. Transverse relaxation time measurement

The transverse relaxation times were calculated from the width of the resonance curve. The measurement of the width of the resonance curves was carried out in an arrangement presented in Fig. 62 and 63.

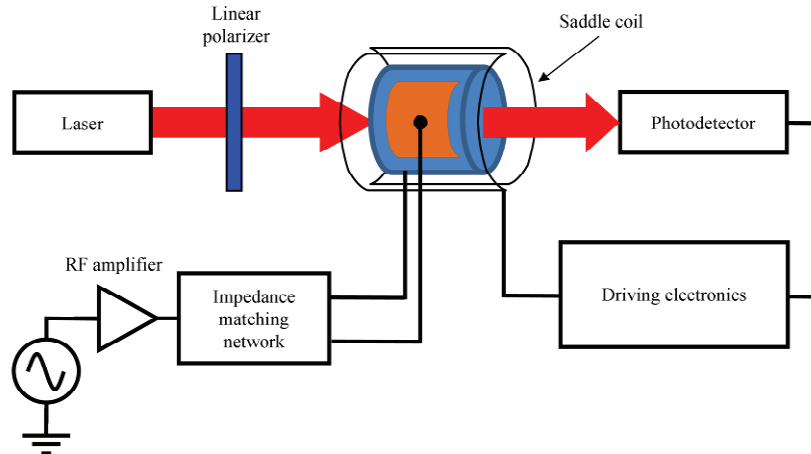


Figure 62. Block scheme of the experimental setup used to measure the width of the resonance lines.

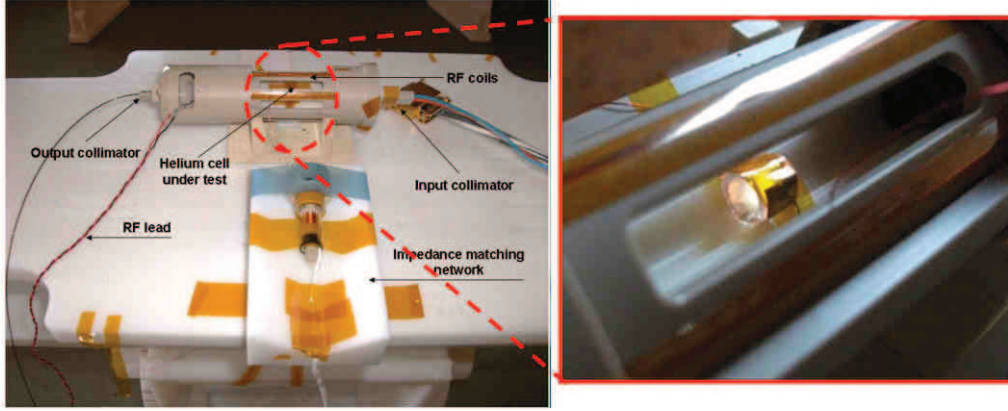


Figure 63. The setup used to measure the width of the resonance lines.

Since magnetic field gradients broaden the resonance curve, this measurement has been carried out in a magnetically clean environment at the CEA-LETI magnetic measurement facilities in Herbeys (wooden cabins). A sample resonance curve for a 20 Torr  $\Phi 5 \times 5$  mm VE cell, obtained by sweeping the frequency of the RF magnetic field, is presented in Fig. 64.

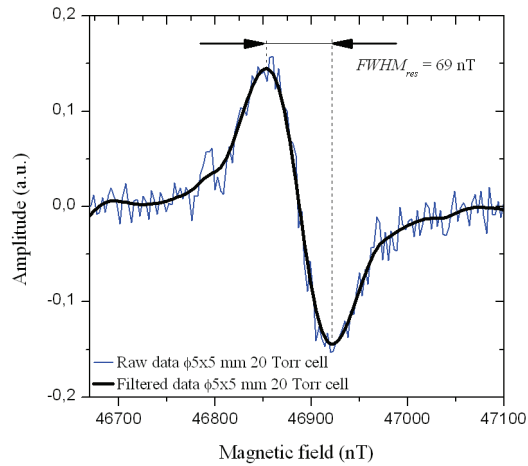


Figure 64. Sample resonance curve for the 20 Torr  $\Phi 5 \times 5$  mm VE cell.

In order to decrease the influence of the pumping light on the measured resonance linewidth, its power was set to an absolute minimum ( $P_{opt} = 200 \mu\text{W}$ , which gives  $\sim 100 \mu\text{W}$  after passing through the linear polarizer) allowing a reliable measurement.

The influence of the RF ( $B_I$ ) field provided by the saddle coils was eliminated by applying a measurement scheme presented in ref. [5]. It consists of measuring the resonance linewidth ( $FWHM_{res}$ ) for multiple, small values of  $B_I$ . The resulting data sets are interpolated to obtain the value of  $FWHM_{res}$  at  $B_I = 0$  (c.f. Fig. 65a). The transverse relaxation time is calculated using Eq. 50.

$$\tau_2 = \frac{1}{\pi FWHM_{res}} \quad (50)$$

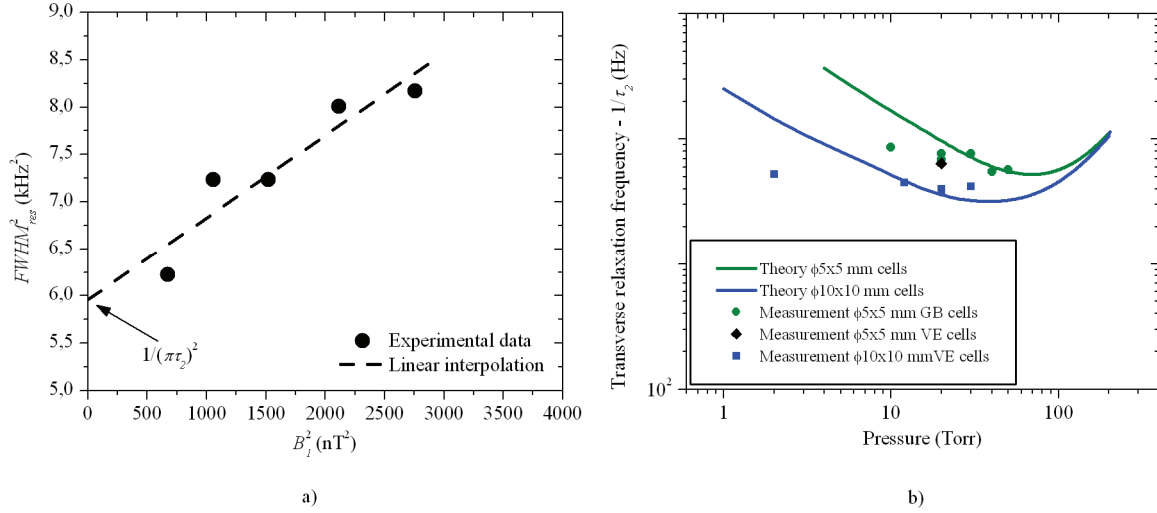


Figure 65. a) Example of a linear interpolation of the measured resonance linewidths. φ5x5 mm 30 Torr cell from GB. b) Transverse relaxation frequencies, compared with theory.

The resulting transverse relaxation frequencies, calculated apart from the measurements of resonance linewidth are presented in Fig. 65b, compared with values obtained theoretically from Eq. 46. A comparison between the measured values of transverse and collisional frequencies is presented in Fig. 66.

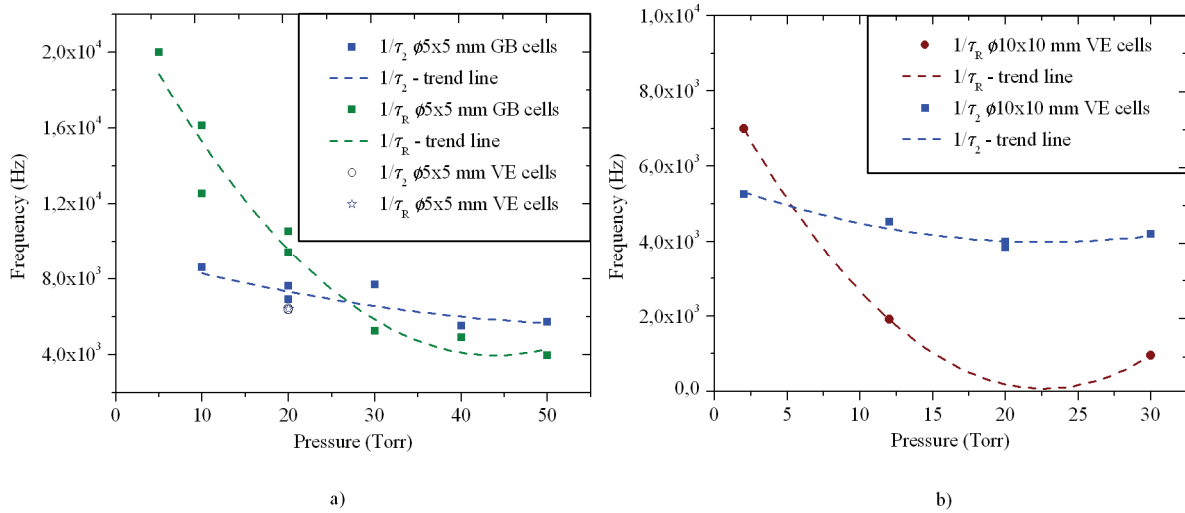


Figure 66. Comparison of transverse and collisional relaxation frequencies. a) φ5x5 mm cells. b) φ10x10 mm cells.

The comparison of experimental values of collisional and transverse relaxation times (c.f. Fig. 66) reveals a significant deviation from theory. Transverse relaxation time was expected to be smaller than the collisional relaxation time, which is not the case at low pressure values. This deviation seems to be more pronounced for smaller helium cells. Its exact physical origin is unclear at the moment.

### 2.7.3. Optimal pressure

The fundamental physical sensitivity of atomic magnetometers is related with spin projection noise. It can be expressed with Eq. 51 [47].

$$\delta B = \frac{1}{\gamma \sqrt{n_m V \tau_2}} \quad (51)$$

where:  $V$  – volume inside the cell irradiated with pumping light.

The optimal value of pressure, for the designed helium magnetometer is the one which maximizes its sensitivity and provides an optimum between the maximums of  $n_m$  and  $\tau_2$ . This value can be found by numerical evaluation of Eq. 51 (c.f. Fig. 67).

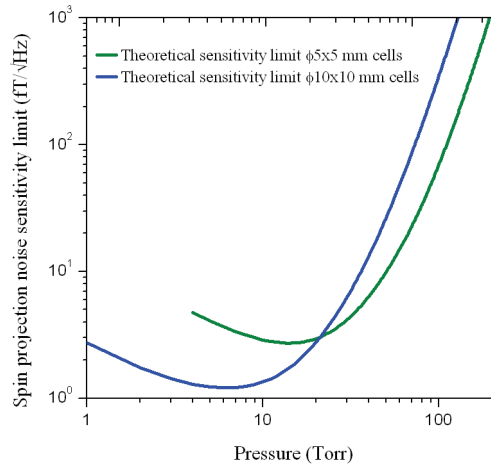


Figure 67. The maximal theoretical values of sensitivity, limited by spin projection noise, for two types of helium cells.

The optimal value of pressure, determined using Eq. 51 was found to be around 10 and 20 Torr for  $\Phi 10 \times 10$  mm and  $\Phi 5 \times 5$  mm helium cells respectively (c.f. Fig. 67). The corresponding sensitivity limits presented in Fig. 67 are purely theoretical values which do not include various degradation mechanisms like magnetic field gradients, laser and electronics noise, which will be discussed in the subsequent chapters. In practice the maximal sensitivities, which were obtained were around 8 and 3.5 pT/√Hz for  $\Phi 5 \times 5$  mm and  $\Phi 10 \times 10$  mm cells respectively. These results are presented in Fig. 68.

The tests of sensitivity, conducted for all the available cells, revealed an unfavourable phenomenon which occurs only in the GB cells. The maximal sensitivity which can be obtained with those cells fluctuates in time. It reaches its maximum after a certain “warm-up” period which consists of maintaining a very intense discharge for a short time. This phenomenon is most probably related with the presence of impurities in the cells due to a different filling procedure used by the American manufacturer, although its exact physical origin is unclear. This phenomenon is unacceptable which means that these cells cannot be used in the construction of a high resolution magnetometer.



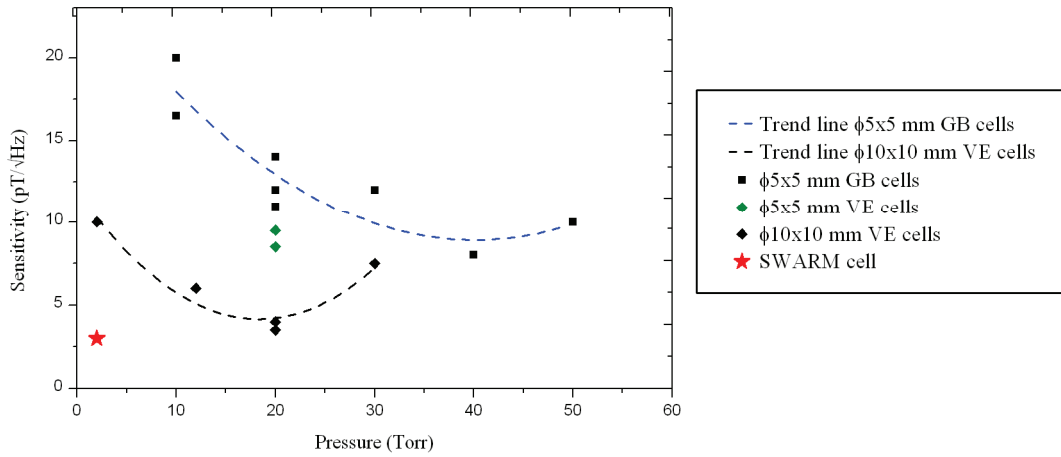


Figure 68. Results of sensitivity measurements. Datapoints connected for clarity.

## 2.8. Conclusion

The resistive part of the discharge impedance was experimentally determined to be in the range of tens of kilo ohms, which seems a reasonable value since along with the sheath and the cell capacitance this gives a load resistance in the order of  $\sim 100 \Omega$ . The efficiency of the matching network used with the miniature magnetometer is estimated to about 50%, which is a sufficiently good result.

The value of pressure with which the magnetometer's cells are filled is limited from the low side by the physics behind the breakdown process. Below a certain limit, the ignition of a discharge becomes very difficult or impossible. This limit value increases inversely to the characteristic size of the helium cell (electrode separation) and the frequency of the HF field. The limits for  $\Phi 5 \times 5$  mm and  $\Phi 10 \times 10$  mm cells are experimentally found to be around 10 and 6 Torr respectively.

Experimental values of metastable density are lower than the ones predicted theoretically (c.f. Fig. 49 and 50). This is likely to be caused by the fact that the numerical model calculates the value of metastable density at the center of the discharge and therefore neglects the spatial distribution of all of the computed parameters.

The values of collisional relaxation frequency measured in the afterglow of the discharge (c.f. §2.7.2.2) seem to follow the theoretical curves fairly well. At small values of pressure the dominant metastable atom destruction mechanism is found to be diffusion and quenching on the walls of the cell (c.f. Fig. 61). In this pressure range the destruction of metastables by electron collisions (stepwise ionization) and collisions between pairs of metastable atoms (Penning ionization) reach their maximum but are never the main contributor. At higher values of pressure the metastables are rather destroyed by three-body collisions. This the increasing number of neutral helium atoms is also the major cause of the sharp metastable density decrease at higher pressures.

The transverse relaxation frequencies show a significant deviation from theoretical predictions at lower pressures. The origin of this deviation is quite difficult to identify. It could be related with the presence of impurities or the influence of selective optical pumping on the cross sections of the considered collisions, both of which were not addressed by the numerical model.

The experimentally determined optimal values of helium pressure for  $\Phi 5 \times 5$  mm and  $\Phi 10 \times 10$  mm cells are 40 and 20 Torr respectively, with corresponding maximal values of sensitivity of 8 and 3.5 pT/√Hz. The optimal values of pressure determined by the developed numerical model are slightly

smaller. This could be due to the fact that its zero-dimensional character fails to accurately reflect all the phenomena in the discharge. In order to address this problem, an attempt was made to assemble a one-dimensional fluid model of the discharge (using Comsol Multiphysics), which would provide a better description. This model consisted of a set of drift-diffusion equations solved for all of the species present in the plasma and the energy of electrons. These equations were coupled with Poisson's equation to account for the distribution of electric field inside the plasma and solved in a one-dimensional geometry with appropriate boundary conditions. Unfortunately due to several problems with the numerical implementation of the highly nonlinear electron energy balance equation, this solution was abandoned.



# Chapter 3: The architecture of the sensor

---

---

3.1.	Desired specifications	89
3.2.	Magnetically vs. optically driven spin precession mode	89
3.2.1.	Optically driven Spin Precession (OSP)	90
3.2.2.	Conclusion	92
3.3.	Optical architecture	92
3.3.1.	Optical source – laser	92
3.3.2.	Light collimation	100
3.4.	HF electrode geometry	102
3.5.	Isotropy of measurement and the liquid crystal polarization rotator	103
3.5.1.	State-of-the-art polarization rotation techniques	103
3.5.2.	Operating principle and construction of the liquid crystal polarization rotator	105
3.5.3.	Performance of the LC polarization rotator	106
3.6.	System architecture	108
3.7.	Conclusion	109

---

---

## Chapter highlights

- The application of a commercial DFB laser diode with an optical isolator as pumping source poses significant problems due to the temporal instability of its noise characteristics. During a stable period it allows to obtain similar sensitivity as the SWARM's fiber laser, nevertheless it is not suitable for magnetometry applications.
- A batch of VCSEL lasers operating at the wavelength of helium D<sub>0</sub> transition is developed and characterized.
- A liquid crystal polarization rotator is found to be an optimal replacement for the piezoelectric motor, allowing easy miniaturization and integration with other sensor's components.
- Sample structures of liquid crystal polarization rotators are developed, characterizations show that they are compatible with magnetometry applications.
- A system architecture of an isotropic helium-4 magnetometer is proposed.



### 3. The architecture of the sensor

The miniaturization of the designed helium magnetometer imposes significant modifications in the architecture of the sensor as compared with the macroscopic version. Some of these modifications may be considered as application-specific, e.g. the change of excitation mode from the resonance induced by a RF magnetic field (MSP) to an all-optical scheme (OSP) which is very favourable in applications requiring array operation (e.g. detection of unexploded ordnance - UXO), where the MSP architecture may suffer from crosstalk. Other modifications are rather technology-related, since some of the components become an obstacle to miniaturization at a certain level (e.g. the piezoelectric motor used to provide isotropy to the measurement).

This chapter presents an analysis of the miniaturization potential of the key elements of the magnetometer. It shows some problems associated with the scaling-down process and several possible solutions. Finally, an optimal system architecture of the sensor is presented.

#### 3.1. Desired specifications

The main requirements which can be stated for the architecture of a miniature, isotropic helium-4 magnetometer can be summarized in the following points.

- Large miniaturization potential – the solutions chosen to be developed at this stage should still allow further miniaturization in the future.
- Relatively low cost – from the economical point of view, miniaturization of the sensor can be justified if it reduces its unit cost. Therefore ideally, most of the elements of the sensor should be compatible with batch processing.
- Non-magnetic construction – all the elements of the sensor head should be free of any ferromagnetic materials (as discussed in §1.1.4.4). Their operation should not perturb the measurement.
- Isotropy of measurement – the architecture must allow for an isotropic measurement of magnetic field

#### 3.2. Magnetically vs. optically driven spin precession mode

As discussed earlier in §1.2, magnetic resonance can also be induced by optical excitation through modulated optical pumping (intensity, frequency or polarization). Those so called Bell-Bloom magnetometers are said to reach performances similar to those of their RF-excited counterparts [48]. One big advantage of this solution is the elimination of RF coils in the construction of the sensor, which is particularly important for array operation (crosstalk). What is more it simplifies the whole system since only the alignment of polarization is necessary, if an isotropy-providing system similar to the one described in §1.1.5 is to be used. Therefore the alignment of  $\theta_{RF}$  at  $90^\circ$ , specific to the MSP scheme, can be eliminated.

Optically excited helium-4 magnetometers have different angular behavior than sensors using RF magnetic field. In order to apply the isotropy-providing mechanism developed for the SWARM magnetometer to an all-optical helium-4 magnetometer, a configuration (similar to the one presented in Fig. 9) would have to be found in which one of the resonance signals becomes extinct (error signal for the alignment of pump beam polarization) while another allows the measurement.

A part of this section concerning the experimental results obtained in the OSP mode as well as some conclusions on the architecture of an isotropic all-optical helium-4 magnetometer have been removed from the manuscript. This is imposed by a patenting procedure which is currently under progress. This part will be inserted to the manuscript once the procedure comes to an end. This fact does not affect the integrity and overall understanding of the text since this was only a preliminary study and a detailed characterization of the sensitivity and heading errors present in the OSP mode will be carried out in the future.

### 3.2.1. Optically driven Spin Precession (OSP)

This method of resonance excitation was first described by W. Bell and A. Bloom [49]. It consists of passing a frequency, intensity or polarization modulated optical beam through an atomic media. In what follows, OSP mechanism is explained [49], [50].

- If the light is not modulated, the overall polarization is near-zero and individual atoms precess with random phases.
- Modulation takes place at Larmor frequency therefore atoms are pumped at the exact moment of completing a precession resulting from the previous cycle.
- The modulation of the beam causes the phases to “synchronise” and atoms to precess coherently since they are pumped simultaneously.

#### 3.2.1.1. Intensity modulation (IM OSP)

Intensity Modulation (IM) consists of varying the optical power of the signal. It is realized with an external intensity modulator according to Eq. 52.

$$I(t) = I_0 [1 + \varepsilon_{\text{mod}} \sin(\omega_{\text{mod}} t)] \quad (52)$$

where:  $I_0$  – intensity of an unmodulated beam

$\omega_{\text{mod}}$  – modulation frequency (Larmor frequency or one of its harmonics)

$\varepsilon_{\text{mod}}$  – modulation depth

In the simplest description, we can consider a square modulation of the optical signal at Larmor frequency (c.f. Fig. 69). Then, there are two states, during one pumping cycle:

- pumping “on” state, during which the atoms are pumped simultaneously,
- pumping “off” state, during which the spins carry out one precession.

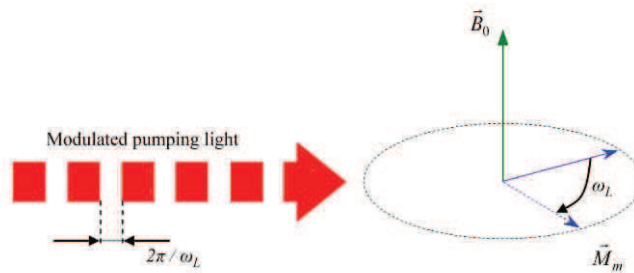


Figure 69. The principle of the IM OSP scheme, based on [50].

Spins are always pumped in the same direction, inducing phase coherence.

It should be noted that a practical realization of this modulation requires an intensity modulator. If an operation of several magnetometers in an array arrangement is envisaged, this means that one modulator is necessary for each node (each separate magnetometer). What is more the magnetic signature and size of the modulator are subject to impose its separation from the sensor head.

### 3.2.1.2. Frequency modulation (FM OSP)

This method of resonance excitation consists of modulating the wavelength (frequency) of the pumping light. Equation 53 expresses the frequency of the resulting optical signal.

$$\nu(t) = \nu_0 + \Delta\nu_s + \frac{\Delta\nu_{mod}}{2} \cos(2\pi f_m t) \quad (53)$$

where:  $\nu_0$  – frequency at the center of the absorption line (corresponding to the  $D_0$  transition)  
 $\Delta\nu_s$  – separation between the carrier frequency of the optical signal and  $\nu_0$   
 $\Delta\nu_{mod}$  – modulation depth  
 $f_m$  – modulation frequency,  $f_m \rightarrow f_L$  (with  $f_L$  – Larmor frequency)

When the modulation depth is larger than half of the width of the  $D_0$  absorption line ( $\Delta\nu_a$ ), resonance is clearly detectable as a modulation in the transmitted beam.

Based on the value of frequency separation ( $\Delta\nu_s$ ) between the carrier and  $\nu_0$ , two FM excitation schemes can be distinguished.

- Half Larmor Frequency (HLF) – for which the carrier is centered on the absorption line ( $\Delta\nu_s = 0$ ) (c.f. Fig. 70). In this scheme the laser frequency passes the entire absorption line width two times per cycle ( $1/f_m$ ) and the modulation frequency is half the Larmor Frequency ( $f_m = f_L/2$ ).

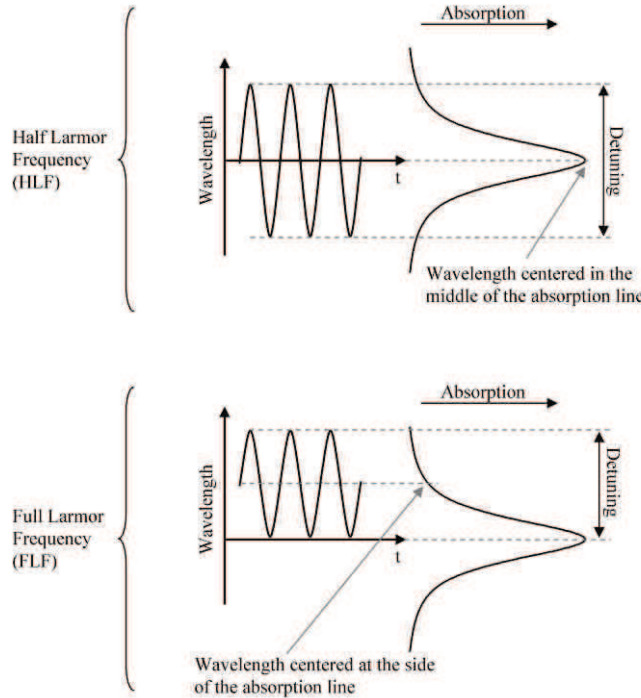


Figure 70. Frequency modulation schemes - Half Larmor Frequency and Full Larmor Frequency. Based on [24].



- Full Larmor Frequency (FLF) – for which the carrier is centered on the side of the absorption line (c.f. Fig. 70) and modulation depth adjusted in order for the laser frequency to pass through the center of the absorption line one time per cycle ( $2\pi/\omega_L$ ). The modulation frequency is equal to the larmor frequency.

The advantage of this method lies in the fact that no additional optical elements are necessary (like an intensity modulator), since the frequency (wavelength) of light emitted by a laser diode can be modulated by adding an AC component to its injection current.

### 3.2.2. Conclusion

The modulation of polarization, which is another optical mean to induce resonance in the atomic media, was excluded from this study. Its practical implementation would need the incorporation of a polarization modulator very close to the sensitive element which is not possible due to its large magnetic signature and big size.

At this stage it was chosen to proceed with the miniaturization of the sensor using the “classical” MSP mode. The technological solutions developed during this process are compatible with both MSP and OSP modes. This approach allows to concentrate solely on the scaling of the sensor, since all the electronics constraints and isotropy characteristics of the MSP mode are well known.

## 3.3. Optical architecture

This section describes all the elements present in the optical path of the developed sensor. Chapter 1.2 provided several state of the art technological solutions, applied in the construction of miniaturized alkali-based atomic magnetometers. In order to obtain a compact and easily manufacturable sensor head, several aspects specific to  $^4\text{He}$  magnetometers have to be taken into account. At the end of the section, some conclusions are made on the global architecture of the designed isotropic helium-4 magnetometer.

### 3.3.1. Optical source – laser

Early constructions of helium-4 magnetometers used electrodeless discharge lamps as optical source. This solution had several disadvantages, apart from its large dimensions, lamp pumping excites all three transitions ( $D_0$ ,  $D_1$  and  $D_2$ ), which is an inefficient way of pumping since  $D_2$  line tends to polarize the atoms in the opposite direction than  $D_0$  and  $D_1$  [46].

The advent of lasers emitting at the wavelength of the  $D_0$  transition significantly improved the efficiency of pumping and thus the sensitivity. First lasers of this type used diode-pumped LNA crystals and a selective optical filter [51] which proved this principle. The first 1083 nm diode lasers were developed by General Optronics Corp. in 1988 as a result of a SBIR project. Such lasers were later commercialized by Spectra Diode Labs Inc. and widely used in helium optical pumping.

The SWARM project uses a specially developed, low-noise fiber laser, based on a diode-pumped Ytterbium-doped optical fiber [52]. The reason behind this is that at the time the project begun no applicable commercial 1083 nm diode lasers were available. This solution is quite bulky, expensive and impossible to implement in mass production. The cost of the optical source used in the

construction of a miniature helium-4 magnetometer is of key importance, especially if array operation is to be considered (in case of FM Bell-Bloom magnetometers this means one laser per array node). Thus the most convenient solution would consist of applying a single mode semiconductor diode operating at 1083 nm. Two types of such diodes were tested: an edge-emitting DFB diode (manufactured by Eagleyard Photonics GmbH) and a VCSEL laser specially developed at the CEA-LETI's optronics department.

### 3.3.1.1. Intensity noise in semiconductor lasers

The intensity noise of light emitted by semiconductor lasers is one of the key factors which limit the performance of atomic magnetometers. This noise is a result of several phenomena related with the construction of the laser and its operating conditions. There are various origins of intensity noise in semiconductor lasers. Most important ones will be presented in this section.

Relative intensity noise (RIN) is a measure of instability of optical power generated by a laser. In the simplest case it can be measured with an arrangement presented in Fig. 71.

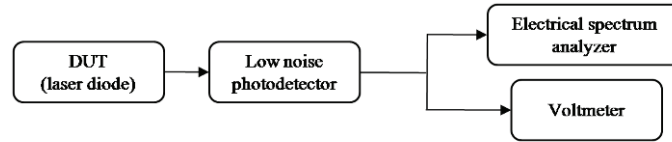


Figure 71. RIN measurement. DUT – Device Under Test.

The value of RIN is determined as the signal to noise ratio of power emitted by the diode, which may be also expressed in terms of voltage measured by the spectrum analyser (c.f. Eq. 54).

$$RIN[dB] = 10 \log \left( \frac{P_{Noise}}{P_{Laser}} \right) = U_N - 20 \log(U_V) \quad (54)$$

where:  $P_{Laser}$  – power emitted by the laser,  
 $P_{Noise}$  – power of noise present in the optical signal,  
 $U_V$  – voltage measured by the voltmeter,  
 $U_N$  – noise voltage measured by the spectrum analyser.

#### 3.3.1.1.1. Shot noise

Shot noise is a fundamental quantum noise related to the discrete character of electrons and photons. The RIN due to shot noise in the laser light is indistinguishable from the shot noise of the photodiode. It can be described by Eq. 55.

$$N_s = \sqrt{P_{avg} h \nu_L} \quad (55)$$

Where:  $h$  – Planck constant,  
 $\nu_L$  – laser frequency,  
 $P_{avg}$  – average light power.

Shot noise is frequency independent. In general the noise of semiconductor lasers is much larger than the shot noise value.

### 3.3.1.1.2. Injection current noise

The noise of current supplies used with laser diodes is directly translated to RIN present in the emitted light. This noise has to be characterized in order to exclude it as a limiting factor. This can be done by connecting the current source to a spectrum analyzer through a shunt resistor. For the available current sources it is typically below the noise of laser diodes used (not the case for LDD200 at HF). Figure 72 presents the injection current noise for three commercially available current supplies at low (c.f. Fig. 72a) and high (c.f. Fig. 72b) frequencies which correspond to the detection of resonance using the  $LA_0$  (continuous) and  $LA_2$  (at  $2\omega_L$ ) signals respectively.

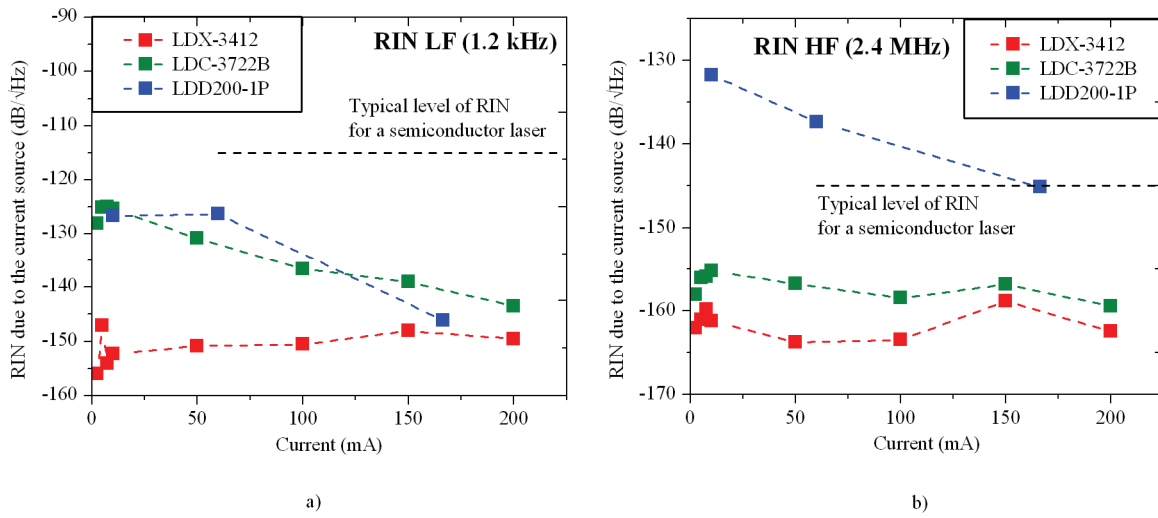


Figure 72. Injection current noise of three commercially available laser current supplies. Data points connected for clarity.

Since the LDX-3412 laser current supply shows the best noise characteristics, it was used throughout the rest of the measurements.

### 3.3.1.1.3. Mode hopping

The length of a laser cavity allows the presence of multiple longitudinal modes. The lasing mode is the one closest to the maximum of cavity gain curve. The wavelength of light emitted by a semiconductor diode is determined by its temperature in two ways.

- By shifting the modes wavelengths due to the change of refractive index and thermal expansion of the cavity. This shift is of about  $0.06 \text{ nm/K}^5$ .
- By shifting the maximum of gain due to a slight change in bandgap of the semiconductor material. This shift is of about  $0.25 \text{ nm/K}^5$ .

The tuning curve (wavelength vs. temperature) of a semiconductor diode is shown in Fig. 73a. Its stepwise character is caused by the separation of different modes.

<sup>5</sup> Values for AlGaAs lasers [53]. 1083 nm lasers described later are based on GaAs for which those values may be slightly different.

Mode hopping occurs when the temperature is fixed at a point where the maximum of gain occurs between two different modes (c.f. Fig. 73b). Those wavelength “hops” are followed by very small intensity fluctuations. Emitted wavelength switches back and forth between two stable values corresponding to the two modes. At the moment of switching RIN rises abruptly for a very short moment.

Mode hopping significantly degrades the performance of the designed sensor therefore attention should be paid to the specifications provided by the manufacturer. The diode used in this study is specified to be “mode-hopping free”.

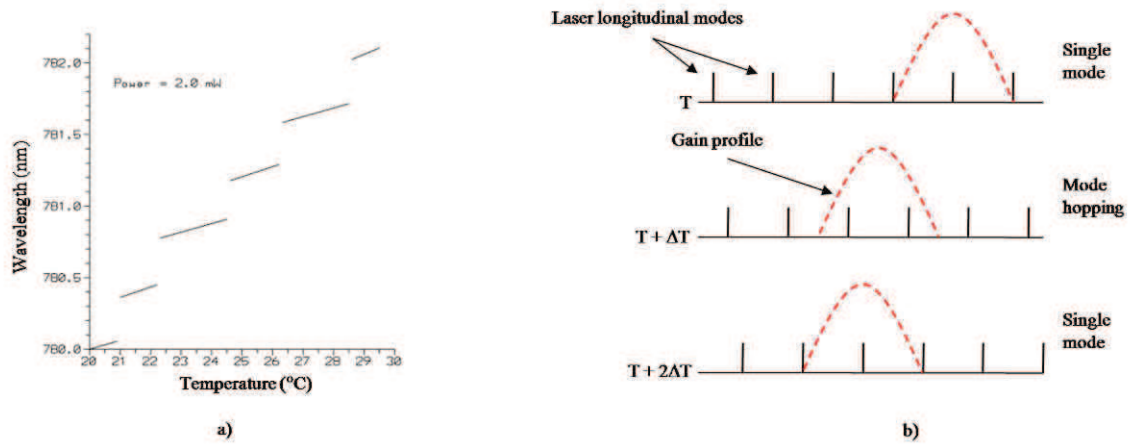


Figure 73. a) Tuning curve of a semiconductor laser [43]. b) Mode hopping mechanism, based on [43].

#### 3.3.1.1.4. Optical feedback

Semiconductor lasers are particularly sensitive to light fed back into their active region. Such feedback is generally caused by back reflections from optical elements including optical fibers used to pigtail laser diodes.

The influence of optical feedback manifests itself as instability of the emitted wavelength. This instability increases with the value of optical power fed back to the diode [54], with an extreme case called “coherence collapse” where the emitted linewidth becomes drastically broadened.

A proper use of a semiconductor diode as applied to magnetometry should consist of application of an optical isolator to suppress the feedback. An alternative solution would be to characterize the feedback effects for the diode of interest and control rigorously feedback in the optical chain (e. g. anti-reflection coating, the use of PM fibers, etc.). The second solution is very difficult to realize in practice.

#### 3.3.1.2. Fiber laser developed for the SWARM magnetometer

The SWARM magnetometer uses a custom-designed, high performance space-qualified fiber laser. A block diagram presenting its construction is presented in Fig. 74.

Its operating principle is based on an Ytterbium-doped optical fiber, pumped by a 980 nm laser diode. Bragg gratings diffused along the fiber form the laser’s cavity. The wavelength is tuned by piezoelectric actuators which induce strain in the fiber and thus finely tune the cavity mode. A part of the output light (20%) is used by the custom-designed noise reduction feedback system, which lowers the effective value of RIN by adding a correction signal to the pumping diode’s current.

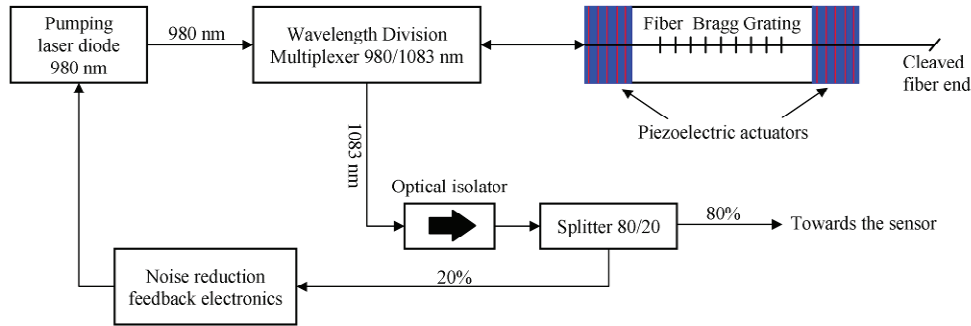


Figure 74. Fiber laser developed for the SWARM project.

One big advantage of this system is that wavelength and output light power are independent parameters, which can be controlled electrically, which is not the case in diode lasers.

As said before, this solution is impossible to miniaturize and implement in large-scale production. Nevertheless its high-performance makes it a very good reference pumping source, which will be used throughout the thesis.

### 3.3.1.3. Edge-emitting DFB laser – EagleYard photonics GmbH

Edge-emitting Distributed Feedback (DFB) diodes are relatively simple to produce at small quantities, which makes them commercially available at the wavelength of interest (1083 nm – the  $D_0$  line). The tested diodes were manufactured by Eagleyard Photonics GmbH under the serial number EYP-DFB-1083.

#### 3.3.1.3.1. RIN characteristics

The RIN was measured on a laboratory testbench, in the arrangement from Fig. 71. The results are presented in Fig. 75a for two frequency ranges of interest.

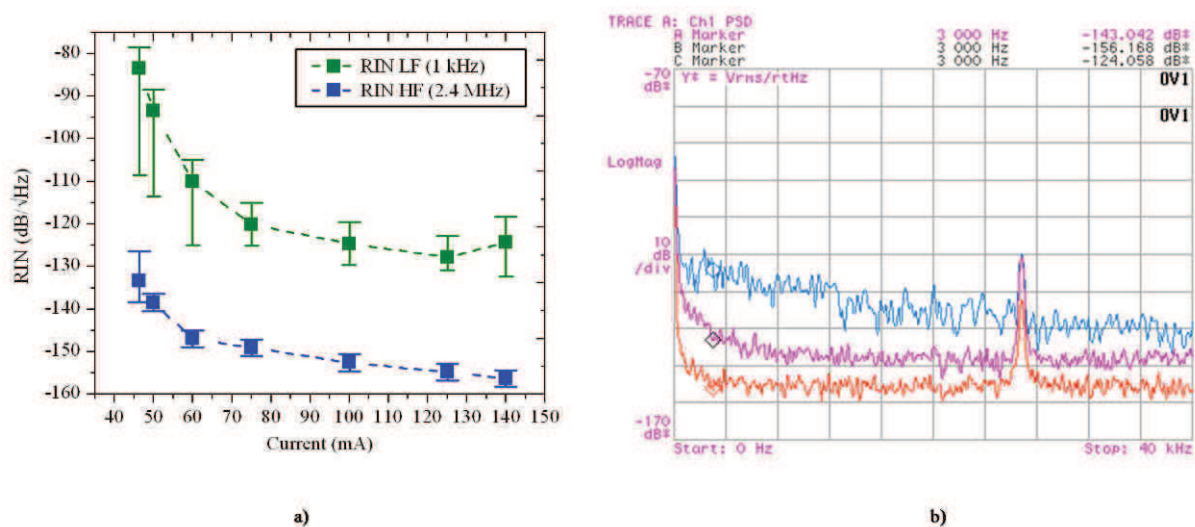


Figure 75. a) RIN noise as a function of current during a stable period. Diode EYP-DFB-1083, S/N: 645. b) Noise characteristics measured with a spectrum analyzer in the arrangement from Fig. 71 without an optical isolator (pink curve). The “jump” in the characteristic - blue curve. The orange curve is the noise of the measurement chain.

The diode was tuned to the  $D_0$  transition for every injection current value by adjusting its temperature.

Noise “jumps” were identified in the RIN characteristic of all of the tested diodes. It manifested itself as a sudden “jump” of the noise spectral characteristic, measured on an electrical spectrum analyser, towards higher values. Figure 75b presents this behaviour. The pink curve represents the RIN of the diode. The “jump” of the characteristic is presented by the blue curve. The frequency of this phenomenon was completely random. It varied from one per 10 seconds to one per minute.

### 3.3.1.3.2. The influence of optical feedback on the performance of the diode

In order to characterize the influence of the optical noise on the performance of the sensor the diode was used as a pumping source in the arrangement from Fig. 76.

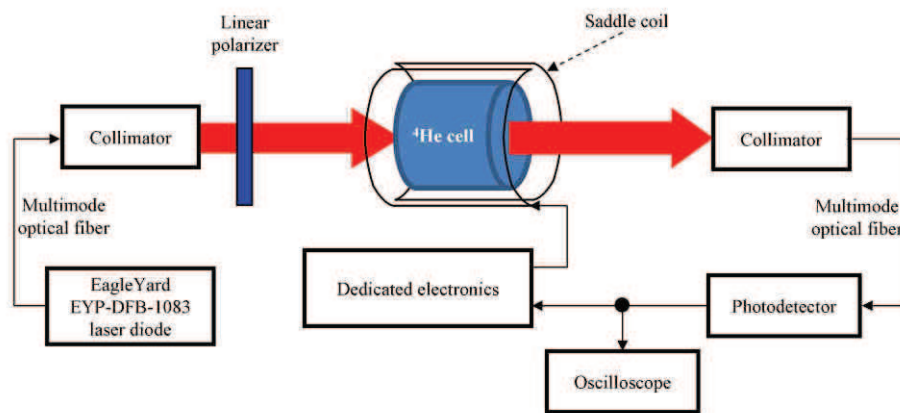


Figure 76. Measurement of sensitivity of a diode-pumped magnetometer.

The sensitivity of the sensor obtained in this arrangement was limited to  $1 \text{ nT}/\sqrt{\text{Hz}}$ , mainly due to laser noise. The signal observed at the oscilloscope (c.f. Fig. 77a) showed significant intensity noise.

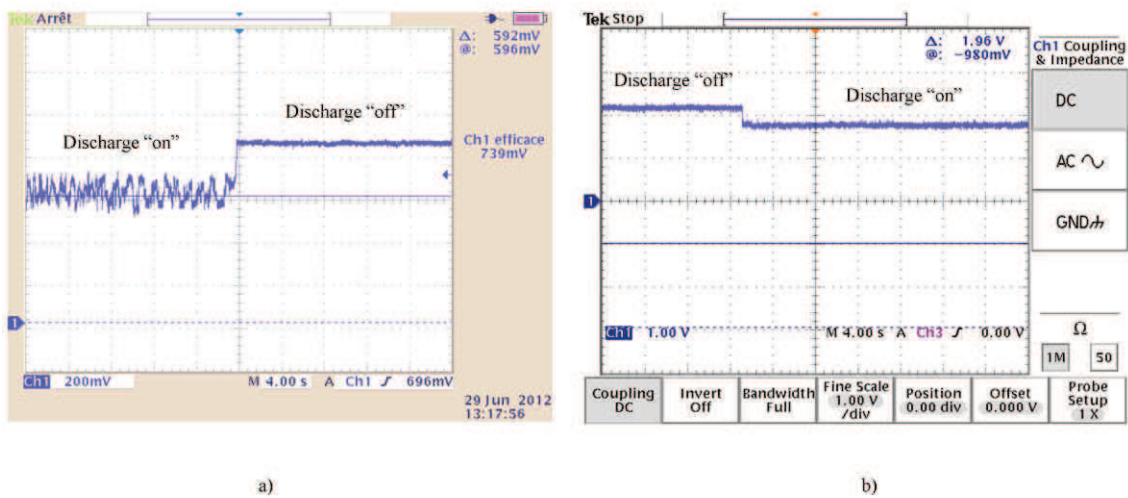


Figure 77. Noise in the output optical signal observed with an oscilloscope. a) without an optical isolator, b) with an optical isolator.



The noise is much more pronounced when the discharge is “on”. This can be explained by the fact that the discharge behaves as an extremely selective bandpass optical filter and the laser emission line broadening, due to wavelength instabilities, becomes clearly visible as intensity noise. This behaviour is attributed to the feedback caused by back reflections from the interfaces present in the optical chain.

The incorporation of an optical isolator increased the sensitivity of the magnetometer and decreased significantly the intensity noise in the output signal (c.f. Fig. 77b). A comparison of noise spectral density of the setup with the use of the described Eagleyard DFB diode with an optical isolator and a fiber laser developed for the SWARM project is presented in Fig. 78 for two different helium cells.

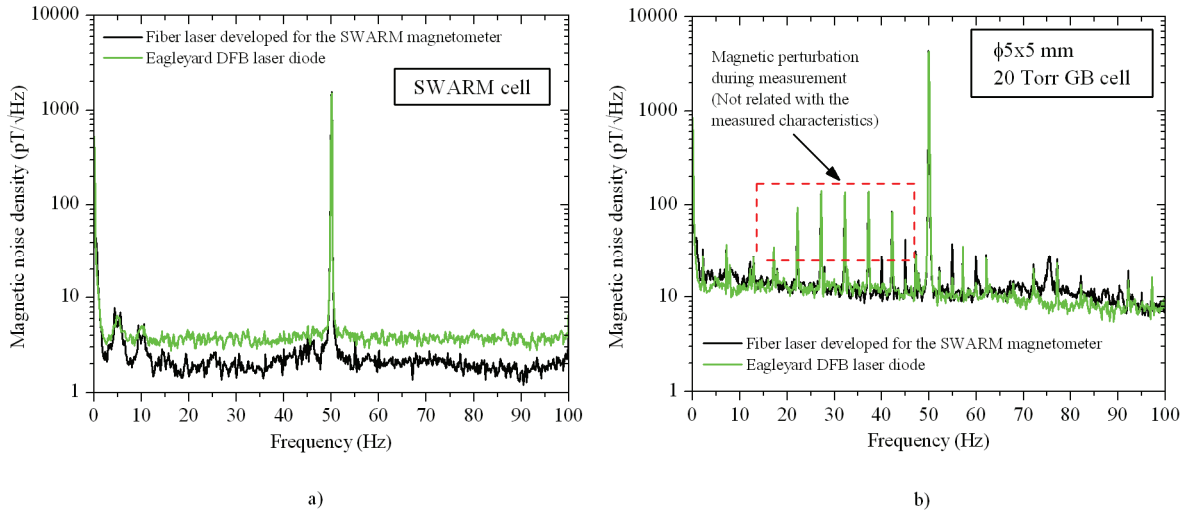


Figure 78. Comparison of noise spectral density of a diode-pumped and fiber laser-pumped magnetometer. a) Measurement done with the SWARM helium cell. b) Measurement done with the  $\Phi 5 \times 5$  mm 20 Torr GB cell.

Similar sensitivity was obtained using both laser sources which means that the incorporation of an optical isolator decreased significantly the noise of the diode laser. Nevertheless, some noise “jumps” are still present in its output. The characteristics presented in Fig. 78 were measured during a period when the laser noise level was stable. During the sudden “jump” the sensitivity becomes degraded by 10-15 pT/√Hz. This suggests that a small part of this noise is intrinsic to the diode, most probably due to feedback caused by pigtailling.

In conclusion, the presented DFB diode does not seem suitable for magnetometry applications “as is”. Its application would require the development of a mean (optical or electronic) to improve its noise characteristics.

#### 3.3.1.4. VCSEL laser

Vertical cavity surface emitting lasers (VCSELs) have several advantages over edge emitting lasers, especially when it comes to low unit cost during mass production. Most important ones are mentioned below.

- Low supply current and small dimensions result in small magnetic signature and allow the laser to be placed close to the sensitive element.

- Because of their vertical construction such lasers can be tested after each fabrication step, contrary to edge emitting diodes which can be only tested after dicing.
- The circular profile of the output beam makes its shaping (and pigtailling) relatively easy.
- Vertical emission allows wafer level optics integration and automatized packaging.
- Low power consumption.
- Much smaller sensitivity to optical feedback as compared to DFB diodes due to smaller size of the laser cavity.

The lower unit cost is particularly important for array operation of the magnetometer, where Bell-Bloom type resonance excitation is preferred because of crosstalk between adjacent excitation coils. In such a system one diode is needed per sensor therefore the laser cost becomes a limiting factor for its development.

Two batches of 1083 nm VCSELS was designed and realized by the CEA-LETI's optronics department (DOPT) in the course of the MiniMag project. Delivered VCSEL structures were characterized by the system integration department (DSIS).

#### 3.3.1.4.1. Fabricated VCSELS

Two batches of VCSELS were developed. The first was a test run. It served to verify whether the structure lases at the proper wavelength (1083 nm) with an output power higher than 1 mW. These two specifications were fulfilled. The output power varied between 1 and 5 mW, depending on the diameter of the active zone and injection current. The VCSELS emitted light at wavelengths comprised between 1080 and 1083 nm, which confirms that quantum dots present in the active region are well designed and that the laser cavity is properly tuned. Nevertheless lasers issued from the first batch were multimode (c.f. Fig 79a).

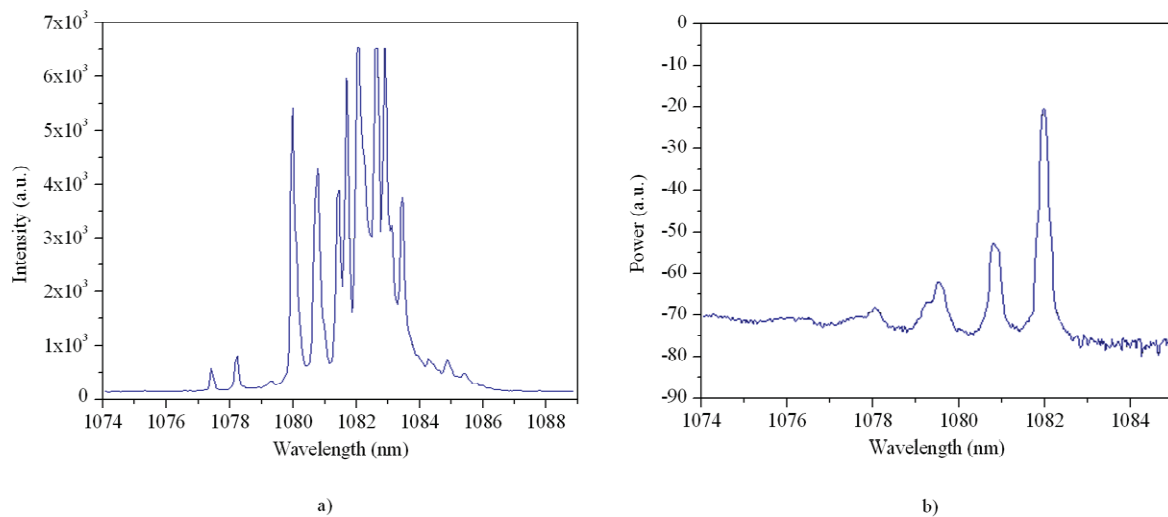


Figure 79. Emission spectra of the developed VCSELS. a) First batch. b) Second batch.

In order to make them single mode, their top Bragg reflectors were micro-structured in the second batch. The micro-structure acts as a photonic crystal, giving a photonic bandgap. Several different patterns of the micro-structure were tested. One of them is presented in Fig. 80a. VCSELS of several



different diameters of the active region were made. The structures were tested on an optics bench (c.f. Fig. 80b).

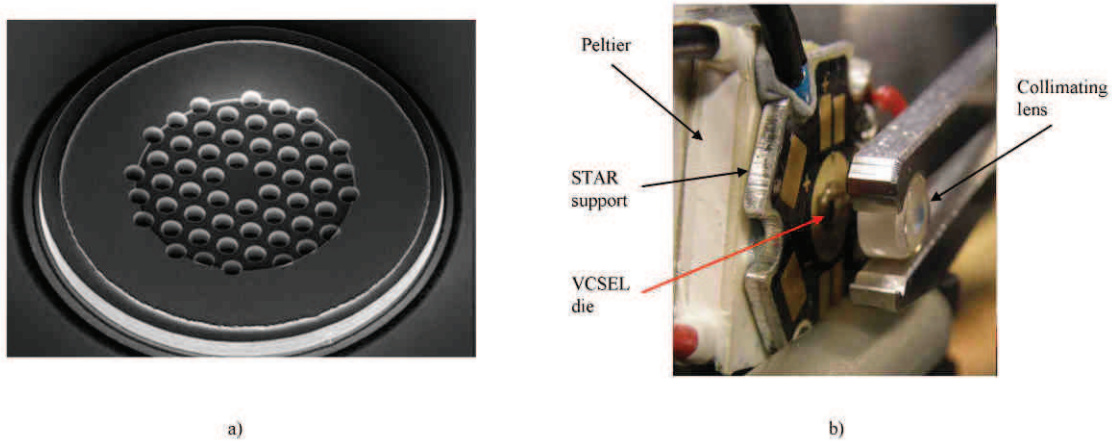


Figure 80. Developed VCSEL laser from the second batch. a) Structure; b) Chip mounted on an optical bench.

#### 3.3.1.4.2. Performance of the developed VCSELs

A first proof of concept of a VCSEL emitting at 1083 nm has been obtained. Ten structures issued from the second batch were conformant with the desired specifications, mentioned below.

- Side Mode Suppression Ratio (SMSR) of 30 dB was obtained.
- No sudden increases of RIN have been found in the noise characteristics.
- Output power was superior to 1 mW.
- RIN of about 100 dB/ $\sqrt{\text{Hz}}$ . In order to obtain the desired magnetometer sensitivity, a noise reduction feedback circuit, as for the SWARM's fiber laser, would have to be added (to decrease the RIN to the desired 140 dB/ $\sqrt{\text{Hz}}$ ).
- Threshold current was smaller than 1 mA.
- Stable linear output polarization was obtained.

In conclusion, it was found that square and hexagonal micro-structure types gave statistically better results than circular ones and that the SMSR increased with decreasing size of the VCSEL structure.

Nevertheless several problems with pigtailling have been identified. The backscattering from the face of the pigtailling fiber caused the VCSEL's to become multimode (optical feedback). What is more, it was not possible to pigtail the VCSEL with polarization-maintaining (PM) fibers due to the poor optical coupling after polymerization of glue. In order to test the VCSELs as a laser source for the developed atomic magnetometer, these problems need to be resolved.

### 3.3.2. Light collimation

The collimation of the pumping beam is very important for the final performance of the sensor, since it determines the optical loss and thus the obtained signal amplitude. There are several requirements for a beam-shaping system, mentioned below.

- Good collimation of light passing through the cell.
- No aberrations in the beam (ideally a perfectly Gaussian shape of the wavefront).
- Good optical coupling.
- Compact and easy to manipulate assembly.
- Non-magnetic construction – since the optics assembly is in proximity of the sensing element.

In practice, very few commercially available collimators fulfill all these requirements. For that reason a custom-made solution was developed. Collimators developed for miniature glassblown cells use a concave + convex lens tandem. Figure 81 presents a computer simulation of the system.

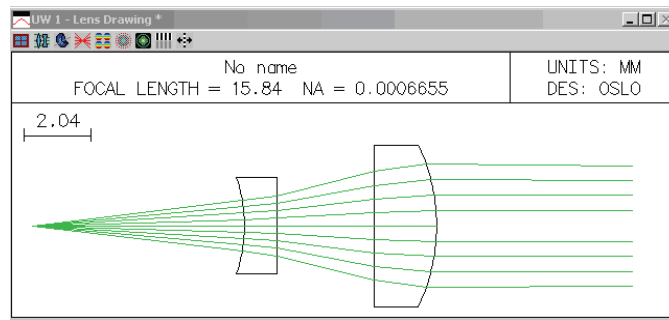


Figure 81. Computer simulation of the lens system used in the construction of a collimator dedicated for miniature glassblown cells.

The concave lens is used in order to spread the beam before it enters the convex lens and becomes collimated. This way the collimator can be made shorter at an expense of small additional insertion loss. The whole assembly is presented in Fig. 82.

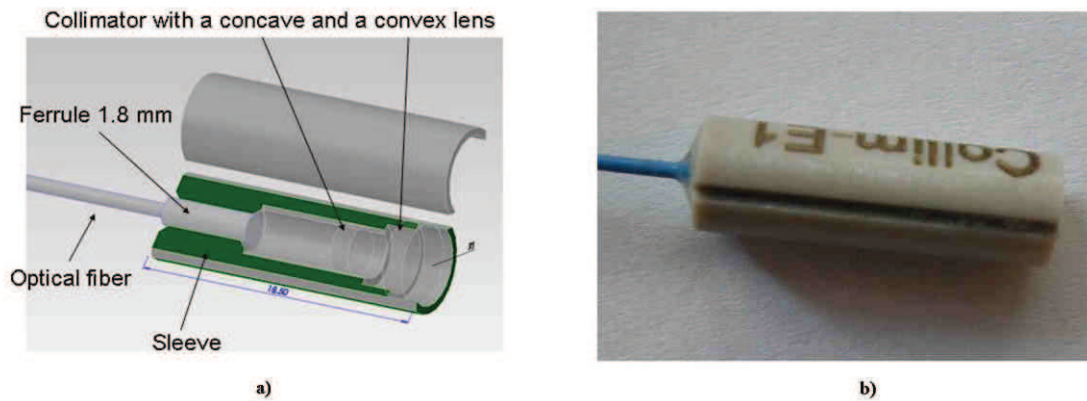


Figure 82. Collimator. a) 3D drawing of the assembly. b) Assembled component.

The structure consists of a pigtailed ferrule and both lenses mounted in a PEEK sleeve. After adjustment of the optical system, all elements are fixed by a UV curable adhesive. The overall length of the collimator is 18.5 mm, it produces a beam of  $\sim 4$  mm in diameter.

### 3.4. HF electrode geometry

The optical pumping is done by passing the laser beam through the majority of the cell diameter (c.f. Fig. 83a).

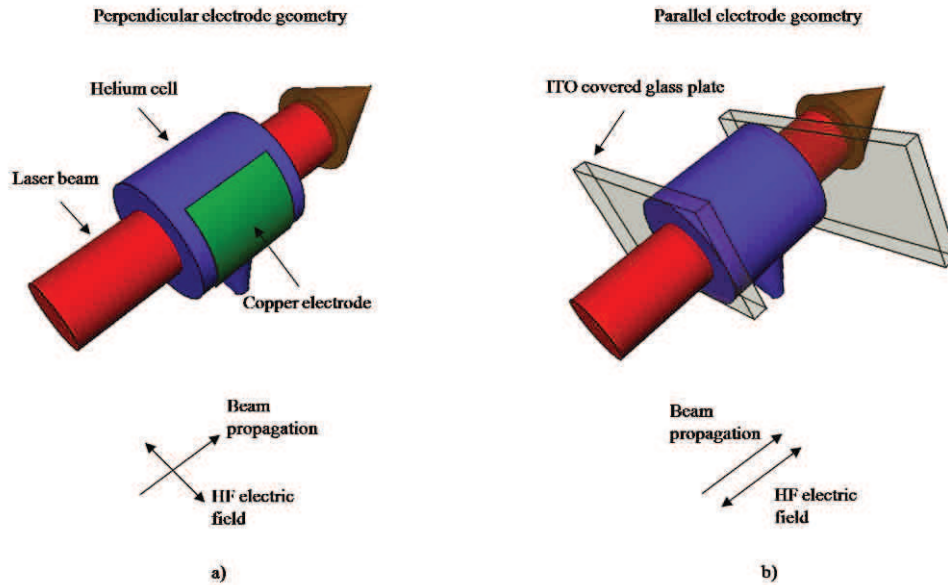


Figure 83. Two possible electrode geometries. a) The “classical” geometry where the pumping beam propagation is perpendicular to the HF electric field maintaining the discharge. b) Modified geometry used to determine the influence of the metastable atom distribution on the performance of the sensor.

Therefore the amplitude of the obtained signal is an average over the metastable atom distribution. Taking into account that the pumping beam has a Gaussian profile, it can be assumed that this is a weighted average. This distribution was found to vary along with the value of helium pressure and power absorbed by the discharge (c.f. §2.7.1.3). This leads to suggest that a simple change in the geometry of the system, consisting of passing the laser beam in parallel with the electric field maintaining the discharge could slightly change the sensor’s characteristics at higher helium pressures and possibly increase the overall sensitivity.

The easiest way to a practical realization of such a geometry is to use transparent electrodes. Figure 83b presents this approach. Two Indium-Tin-Oxide (ITO) glass sheets were used to ignite and maintain the discharge in the cell and the pumping light was passed through them. The rest of the experimental setup is identical to the one presented earlier (c.f. Fig. 62 and 63). The optimal values of sensitivity for two  $\Phi 5 \times 5$  mm helium cells, using the two described electrode geometries are presented in Fig. 84. No significant difference, neither in sensitivity nor in other characteristics of the sensor was found between the two approaches.

This leads to a conclusion that both geometries can be successfully used in this pressure and power range. Consequently, the much simpler perpendicular electrode geometry from Fig. 83a will be used in the architecture of the miniature sensor, using glassblown helium cells.

Nevertheless the parallel configuration seems a very good solution, when it comes to further miniaturization of the sensor, since it is fully compatible with semiconductor batch processing technologies and allows vertical integration (ITO deposition on glass). This solution will be used to demonstrate a proof of principle of a microfabricated helium cell towards the end of the thesis.

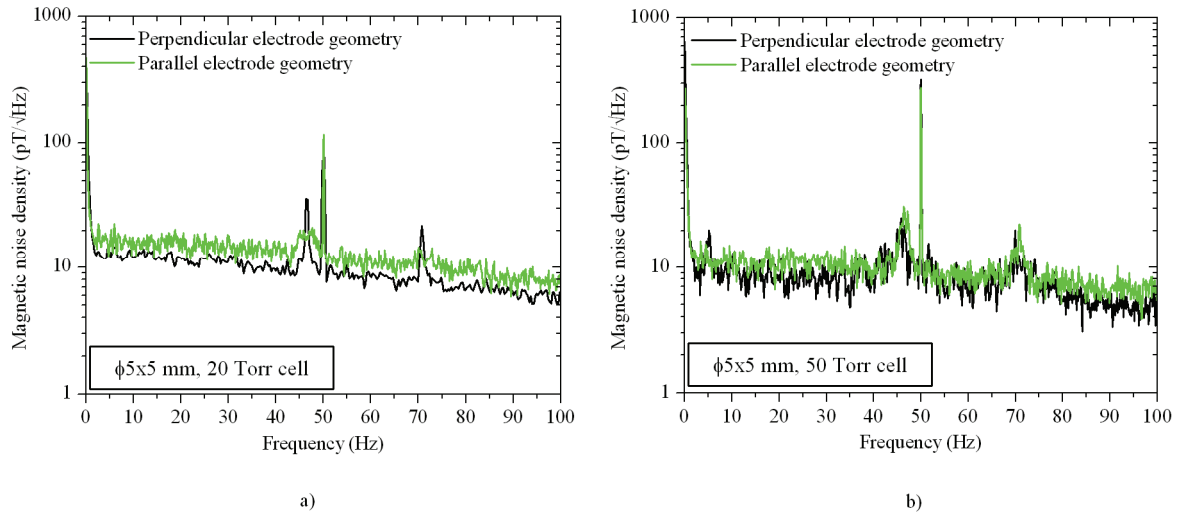


Figure 84. Noise spectral density curves obtained using different electrode geometries. a) 20 Torr  $\Phi 5 \times 5$  mm GB cell. b) 50 Torr  $\Phi 5 \times 5$  mm GB cell.

### 3.5. Isotropy of measurement and the liquid crystal polarization rotator

Most of the applications aimed at by the miniaturization of the present sensor (mobile and space applications) require the measurement to be isotropic. The solution developed by LETI up to date (presented in 1.1.5) has limited scaling-down potential (piezoelectric motor) and is not perfectly non-magnetic. A different solution had to be adopted instead which would allow easy integration with the rest of the miniature sensor's components.

#### 3.5.1. State-of-the-art polarization rotation techniques

In order to find a suitable polarization rotation technique, a brief literature study was carried out. Several commercial solutions have been identified. Table 13 provides a summary of the study.

Table 13. Identified polarization rotation solutions.

Polarization rotation solution	Physical mechanism	Driving	Integration potential	Remarks	Ref.
Mechanical rotation	Mechanical rotation of a polarizer	Electro-mechanical	Limited	Already in use (the SWARM magnetometer). Not perfectly non-magnetic.	[55]
Faraday rotator	Faraday rotation	Magnetic	None	Not applicable in the construction of a magnetometer. Enormous magnetic signature.	-

Table 13. Continued.

<b>Polarization rotation solution</b>	<b>Physical mechanism</b>	<b>Driving</b>	<b>Integration potential</b>	<b>Remarks</b>	<b>Ref.</b>
Fiber squeezer	Mechanical strain of an optical fiber using a piezoelectric	Electrical – DC (0~70 V)	Limited	Fiber-optic solution driven by DC voltages. Potentially large magnetic signature.	[56]
Ferroelectric ceramic rotator	Electro-optic effect in PLZT ceramics	Electrical – DC (0~180 V)	Good	High DC Voltage, output beam divergence. Potentially large magnetic signature.	[57]
Electro-optic rotator	Electro-optic effect in lithium niobate crystal	Electrical – DC (0~30 V)	Excellent	Complicated driving, high cost. Magnetic signature unknown.	[58]
Liquid crystal polarization rotator	Variation of birefringence of liquid crystals.	Electrical - AC (1~10 kHz, 0~10 V <sub>RMS</sub> )	Excellent	Slight drift of dynamic characteristics with temperature. Very small magnetic signature.	[59]

Ideally, the solution applied in a helium magnetometer should allow a free-space (rather than fiber-optic) operation. This is related with the fact that the Polarization Extinction Ratio (PER) decreases significantly when the beam passes through an optical fiber, with an extreme case of elliptical polarization at the end. As such, this system should be placed very close to the active element, which consequently imposes very strict requirements on its magnetic compatibility.

Only a polarization rotator based on liquid crystals fulfills all the required specifications reasonably well. What is more it has several important advantages compared to the piezoelectric servomechanism used in the SWARM magnetometer. These advantages include:

- large miniaturization potential,
- full compatibility with semiconductor processing,
- no magnetic materials,
- no moving parts,
- no mechanical vibrations induced during operation (important for space applications where they are difficult to damp).

As a result, the liquid crystal polarization was chosen as the replacement of a piezoelectric motor in the isotropy-providing system of the miniature version of the magnetometer. This solution is subject of a patent (FR1262014).

This section covers the operating principle of a Liquid Crystal (LC) polarization rotator. It describes a construction of this type, designed and realized in cooperation with the CEA-LETI's optronics department. Static and dynamic characteristics of the developed rotator are presented at the end of this section.

### 3.5.2. Operating principle and construction of the liquid crystal polarization rotator

The operating principle is schematically presented in Fig. 85. The liquid crystal layer is sandwiched between two quarter-wave plates and a linear polarizer. The polarization rotation is determined by the birefringence of the LC layer which is varied by applying an AC square signal ( $0.5-5 V_{\text{RMS}}$ ) whose frequency ( $1-10 \text{ kHz}$ ) does not interfere with the detection electronics (for the  $LA_0$  signal a modulation at  $1 \text{ kHz}$  is used). Its amplitude causes the LC molecules to change their position and thus the phase retardation of the system.

The developed polarization rotator is designed to operate at the wavelength of helium  $D_0$  transition ( $1083 \text{ nm}$ ).

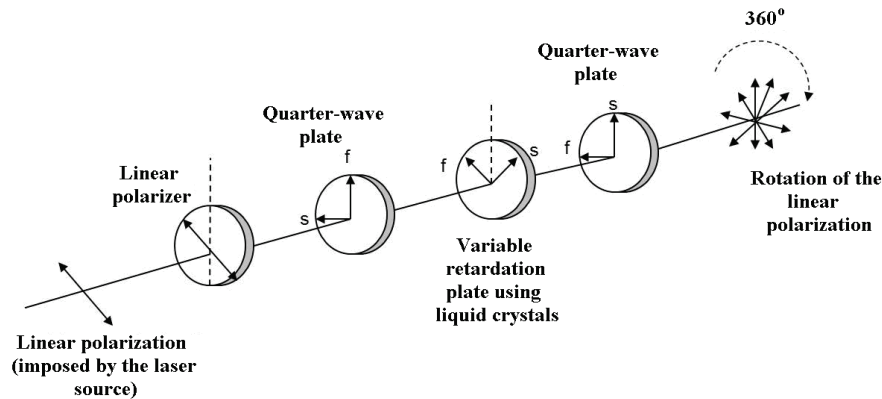


Figure 85. LC polarization rotator operating principle.

LC rotators are made using well known technologies issued from the LCD industry. Two indium-tin-oxide (ITO) coated glass wafers are spin-coated with a polyimide (PI) alignment layer (SE7492 diluted with 2M solvent). The PI layer is rubbed in order to assure proper LC anchoring. Both wafers are bonded with a screen printed adhesive. Substrates are laser-cut into separate LC sells. They are filled with LC material (MLC 2062) and sealed hermetically. The structure of the rotator (c.f. Fig. 86a) consists of two LC cells assembled in series.

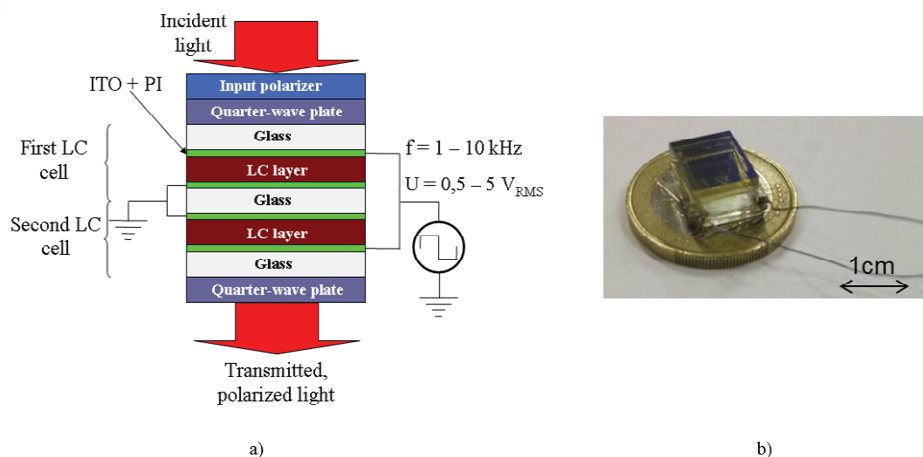


Figure 86. a) The LC polarization rotator structure and electrical driving scheme. b) Sample structure.

The thickness of the LC layer determines the range of polarization rotation which can be obtained with the rotator. However the increase of thickness reduces the response time of the device. An optimal



solution consists of the use of two LC cells in series, this allows to increase the rotation range while maintaining a fast response of the rotator. Fast response is of key importance in portable applications (rapidly changing directions of the magnetic field). The two LC cells, the quarter-wave plates and a linear polarizer are assembled together using optical bonding. Angular precision with which the elements are positioned during bonding is crucial since it determines the polarization quality at the output of the rotator. The solution developed to realize this alignment is the subject of a patent application.

The dimensions of the assembled structure are:  $10 \times 10 \times 7 \text{ mm}^3$ . It is shown in Fig. 86b. Its optical aperture is of 50% of the surface and can still be optimized, while further miniaturization is possible and relatively simple.

### 3.5.3. Performance of the LC polarization rotator

Polarization rotation versus applied voltage transfer function has been measured using a laboratory optical bench. The state of polarization is analyzed by the polarizer/analyzer technique (c.f. Fig. 87a).

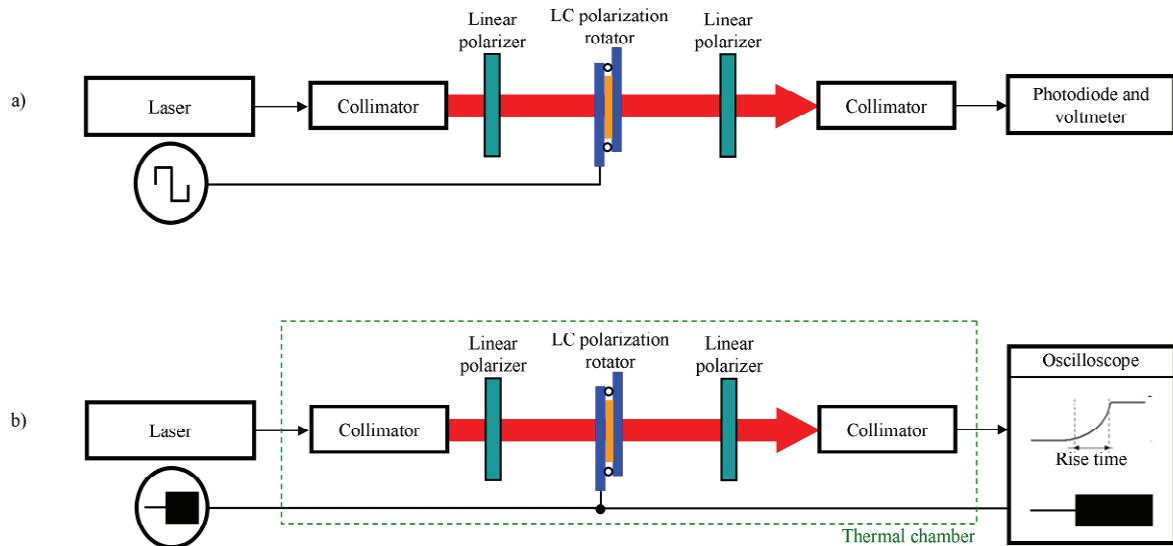


Figure 87. Setup used during the characterisation of the LC rotator. a) PER and angle/voltage characteristic measurement. b) Rise time measurement consisting of observation of the response of the rotator during a “switch on” of the driving signal.

Polarization Extinction Ratio (PER) is an essential parameter when it comes to the reduction of heading errors. Measured characteristics are presented in Fig. 88a. PER of about 20 dB was obtained in a polarization rotation range of more than  $300^\circ$ . These results are temperature independent in the measured range of temperatures ( $10\text{--}40^\circ\text{C}$ ).

Dynamic measurements carried out using the setup presented in Fig. 87b, have shown that the response times are relatively short. Figure 88b presents the temperature dependence of rise time for rotation steps of  $5^\circ$  for three initial positions of the polarization (response times depend on the initial voltage applied across the liquid crystal). Fall times had similar values and temperature behaviour.

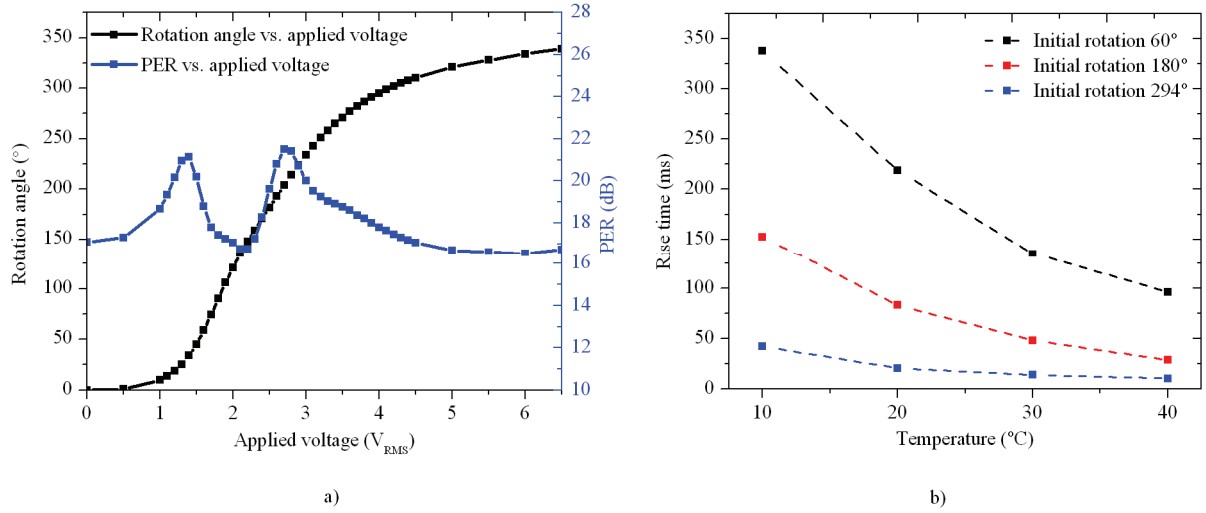


Figure 88. Characteristics of the LC polarization rotator. a) Polarization rotation angle and PER as a function of the applied voltage for a driving frequency of 10 kHz at room temperature. b) Temperature dependence of the rise time for rotation steps of 5°. Driving signal at 10 kHz. Datapoints connected for clarity.

For larger rotation steps of 180° there appears a difference between rise and fall times (c.f. Fig. 89a and 89b), which is inversely proportional to temperature. This fact is related with the changing viscosity of the liquid crystal solution.

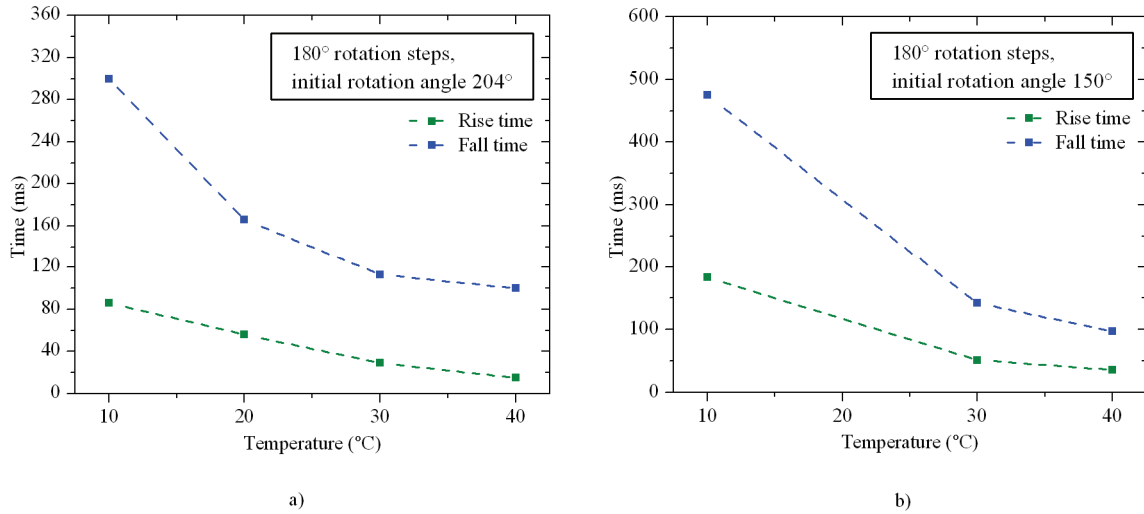


Figure 89. a) Temperature dependence of the rise and fall times for rotation steps of 180°. Driving signal at 10 kHz. Initial rotation of 204°. b) Temperature dependence of the rise and fall times for rotation steps of 180°. Driving signal at 10 kHz. Initial rotation of 150°. Datapoints in both figures connected for clarity.

The static magnetic signature of the rotator has been measured using the macroscopic SWARM magnetometer. The LC rotator and its electrical driving were found to be non-magnetic which enables a positioning very close to the  $^4\text{He}$  cell.

All the conducted characterizations show that the developed liquid crystal polarization rotator is fully compatible with the application in an atomic magnetometer.



### 3.6. System architecture

The basic idea behind the system architecture of the developed miniature isotropic helium-4 magnetometer is similar to the one presented in 1.1.5, although the specific driving scheme and characteristics of the LC polarization rotator impose some modifications. The described system is a subject of a patent (FR1262014). Some issues, like the discontinuity of polarization rotation (once the maximal value is reached a return to the initial value is necessary), are still to be addressed. Therefore the presented explanation is only a general description of the system, while many of its building blocks would still require some development.

The architecture is schematically presented in Fig. 90. It consists of three separate feedback loops. The first is the RF frequency adjust feedback (marked green), which locks itself on the Larmor frequency.

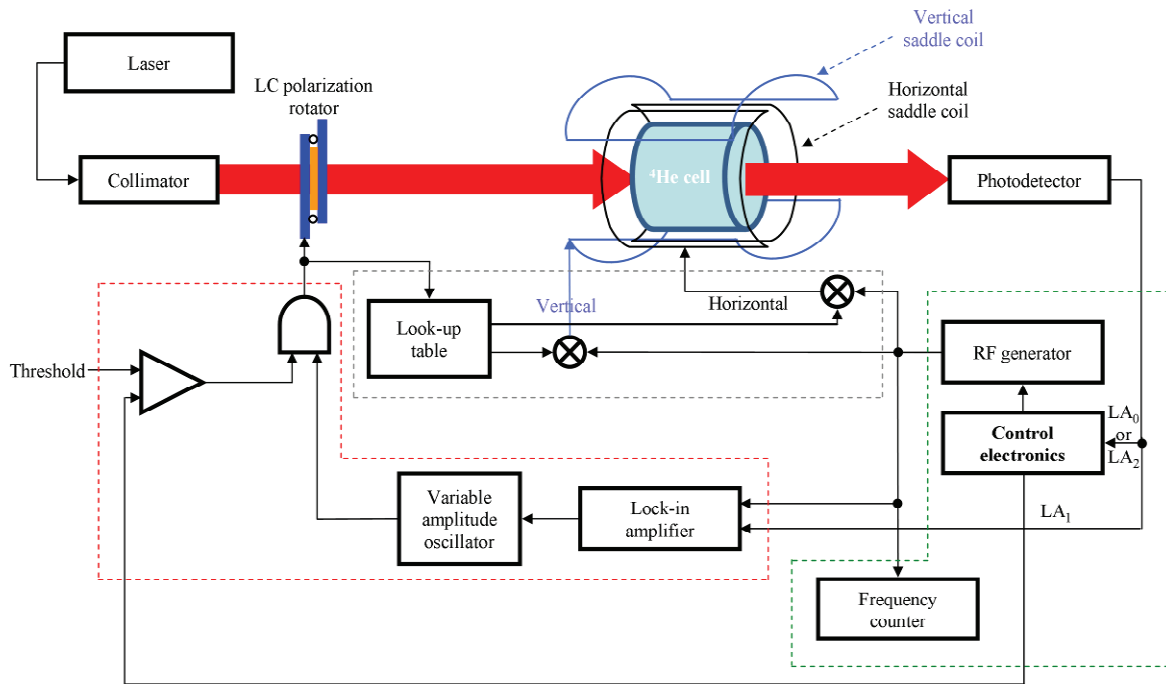


Figure 90. Block scheme of the isotropy-providing system.

The second is the polarization tuning loop (marked red), which fixes the polarization at  $90^\circ$  with respect to the ambient magnetic field  $B_0$ . The third, marked grey, is used to set the RF excitation field parallel with the polarization vector so as to fix the direction of the radio-frequency field at right angle with the external magnetic field.

The polarization angle is maintained at  $90^\circ$  with respect to the ambient magnetic field. In such a configuration the amplitude of  $LA_1$  signal is null (c.f. Fig. 9). Therefore it is used as error signal to set the polarization angle.  $LA_0$  or  $LA_2$  signals are used to measure the magnetic field. A logic circuit consisting of a comparator and a gate is used to prevent the loop from locking on 0 or  $55^\circ$  (two other minimums in the angular characteristics – c.f. Fig. 9). If the value of the measured  $LA_0$  or  $LA_2$  signals are higher than the given threshold value, the voltage issued from the variable amplitude oscillator is validated. Simultaneously, the angle of the RF excitation field imposed on the  $^4\text{He}$  cell is maintained parallel to the polarization vector. This is realized with a look-up table which contains calibration

curves of the rotator (angle/voltage) and corresponding coefficients to apply to the multipliers. This way different RF amplitudes are applied to two separate Helmholtz coils orthogonally mounted around the cell.

This electronic servomechanism still needs to be carefully designed, realized and tested. During preliminary characterisations, presented in the next chapter, both the polarization rotation and the angle of the RF field are tuned manually.

### 3.7. Conclusion

A study on applicability of different components and solutions in the construction of a miniature isotropic helium-4 magnetometer has been presented. It allows to define a functional architecture, which will be used in the final demonstrator, with the following points.

- Resonance induced in the atomic media by application of a RF magnetic field (the MSP scheme).
- $\Phi 5 \times 5$  or  $\Phi 10 \times 10$  mm glassblown helium cell.
- Fiber laser (c.f. §3.3.1.2) used as optical pumping source.
- Liquid crystal polarization rotator used to fix the angle of polarization of pumping light at right angle with the external magnetic field (the voltage applied to the rotator adjusted manually).
- Control electronics dedicated to the macroscopic version of the sensor.

In a future perspective, the work on dedicated VCSEL lasers will be continued in order to overcome the identified problems with packaging. Some attention will be also dedicated to the possibility of stabilization of noise characteristics of the tested commercial DFB lasers.

Further development will concentrate on the implementation of the polarization control architecture (c.f. Fig. 90). A dedicated electronic system will be developed in this purpose.

Depending on the future application fields, addressed by the sensor, the all-optical architecture will be studied in more detail. Possibly a new polarization driving scheme and control electronics will be developed as well.



# Chapter 4: First demonstrator of an isotropic miniature scalar magnetometer

---

4.1.	First results obtained with glassblown cells	113
4.1.1.	Results obtained with the $\Phi 10 \times 10$ mm 20 Torr VE cell	114
4.1.2.	Results obtained with the $\Phi 5 \times 5$ mm 20 Torr VE cell	114
4.1.3.	Results obtained with the $\Phi 5 \times 5$ mm 20 Torr GB cell	115
4.1.4.	Results obtained with the $\Phi 5 \times 5$ mm 40 and 50 Torr GB cell	116
4.1.5.	Conclusion – VE versus GB cells	116
4.2.	Packaging and system architecture of the final demonstrator	117
4.3.	Performance of the demonstrator	118
4.4.	Perspectives: first steps towards a chip scale helium magnetometer	119
4.4.1.	The study on technological solutions for a chip-scale helium magnetometer	119
4.4.2.	Microfabricated helium cells	122
4.4.3.	Concept of a chip scale helium magnetometer	128
4.5.	Conclusion	130

---

## Chapter highlights

- Optimal results obtained with  $\Phi 10 \times 10$  and  $\Phi 5 \times 5$  mm cells are presented in detail. GB cells are found to obtain poor results in term of long term stability of signal, which is attributed to the presence of oxygen impurities.
- The presence developed liquid crystal polarization rotator as well as its electrical driving do not change the sensitivity of the magnetometer.
- A demonstrator of a miniature isotropic helium magnetometer, using a liquid crystal polarization rotator is presented. This system obtains a sensitivity of  $10 \text{ pT}/\sqrt{\text{Hz}}$ .
- Magnetic properties of key components, envisaged in the construction of a chip-scale helium magnetometer were measured. Most of the components are applicable in magnetometry.
- A proof-of-concept of helium confinement in a microfabricated glass-silicon-glass cell is given.



## 4. First demonstrator of an isotropic miniature scalar magnetometer

This chapter describes the final results obtained during the thesis. It presents the optimal results obtained with selected glassblown helium cells and concludes on differences between two cell manufacturers. All measurements presented in this chapter were carried out in a magnetically “clean” environment at the CEA-LETI’s magnetic test facility at Herbeys.

The developed demonstrator of a miniature isotropic helium-4 magnetometer is presented. After a brief description of the mechanical part of the sensor, a detailed characterization is done. The demonstrator uses a liquid crystal polarization rotator which fixes the axis of linear polarization of pumping light at right angle with the ambient magnetic field and thus provides isotropy to the measurement. The demonstrator uses a  $\Phi 5 \times 5$  mm glassblown helium cell.

The last part of the chapter presents further perspectives of miniaturization. It presents first results obtained with microfabricated helium cells, developed in cooperation with FEMTO-ST. Moreover it presents an experimental evaluation of magnetic compatibility of several possible materials and solutions which can be applied in the future development of a chip-scale helium atomic magnetometer.

### 4.1. First results obtained with glassblown cells

At the design stage of the demonstrator, performances which could be obtained with all available helium cells were characterized. This allowed to determine the optimal size and pressure value for the final demonstrator of a miniature isotropic helium-4 magnetometer. The results of this study were already partially presented in §2.7.3, this section presents the best results in more detail and concludes on the optimal solutions.

A prototype demonstrator was developed for the needs of this study (c.f. Fig. 91). It is a convenient measurement platform allowing easy handling of different helium cells and eliminating the need to adjust the optical system each time a cell is replaced.

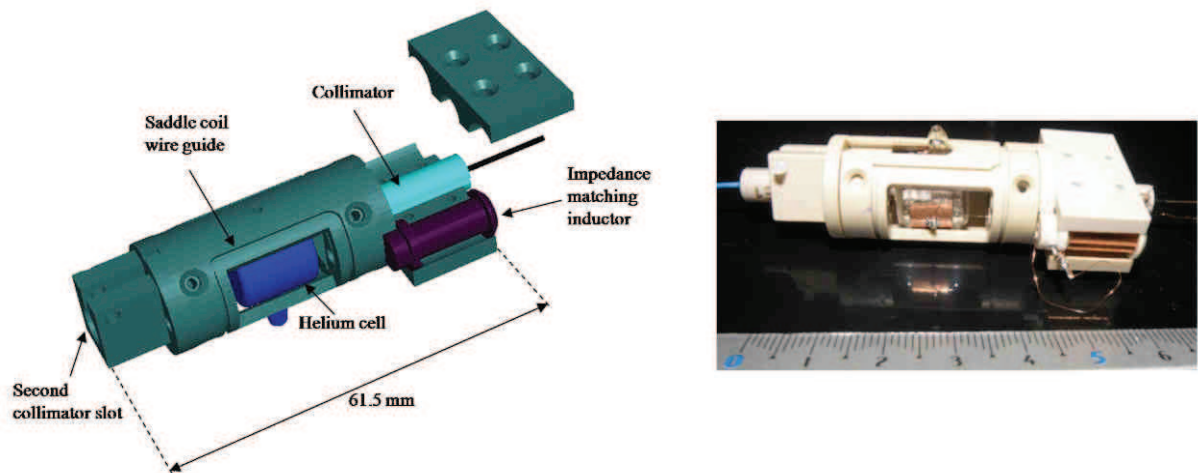


Figure 91. Prototype demonstrator used to determine the optimal size and pressure of helium cells for the final demonstrator.

Two parameters of key importance for the final demonstrator, which are characterized, are the sensitivity and long term stability of measurement. The latter is measured in the gradiometer configuration. This is realized using two reference NMR magnetometers (c.f. Fig. 92).

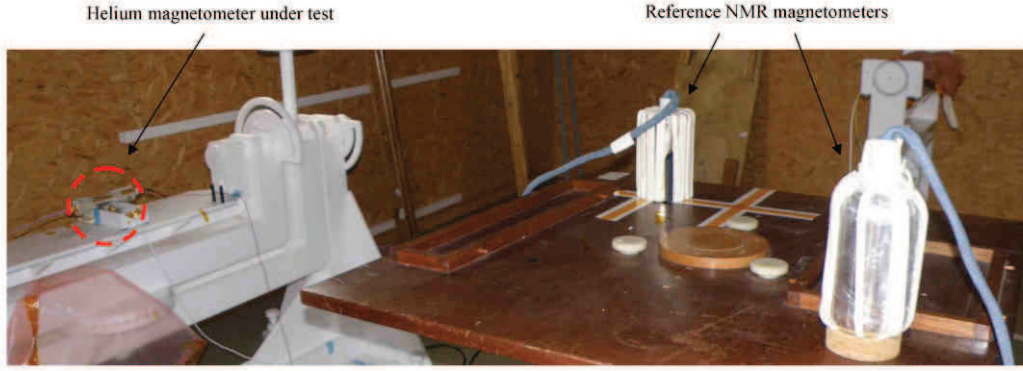


Figure 92. The gradiometer setup used to study the long term stability of measurement.

The results obtained with the reference NMR magnetometers are subtracted from the ones obtained with the helium magnetometer. This way the common mode Earth's fields variations are rejected and soely the measurement stability, intrinsic to the helium sensor is observed.

#### 4.1.1. Results obtained with the $\Phi 10 \times 10$ mm 20 Torr VE cell

The maximal value of sensitivity obtained with the  $\Phi 10 \times 10$  20 Torr VE cell was around  $4 \text{ pT}/\sqrt{\text{Hz}}$  (c.f. Fig. 93a). This value is very close to the one obtained with the macroscopic cell used by the SWARM magnetometer ( $\sim 1 \text{ pT}/\sqrt{\text{Hz}}$ ).

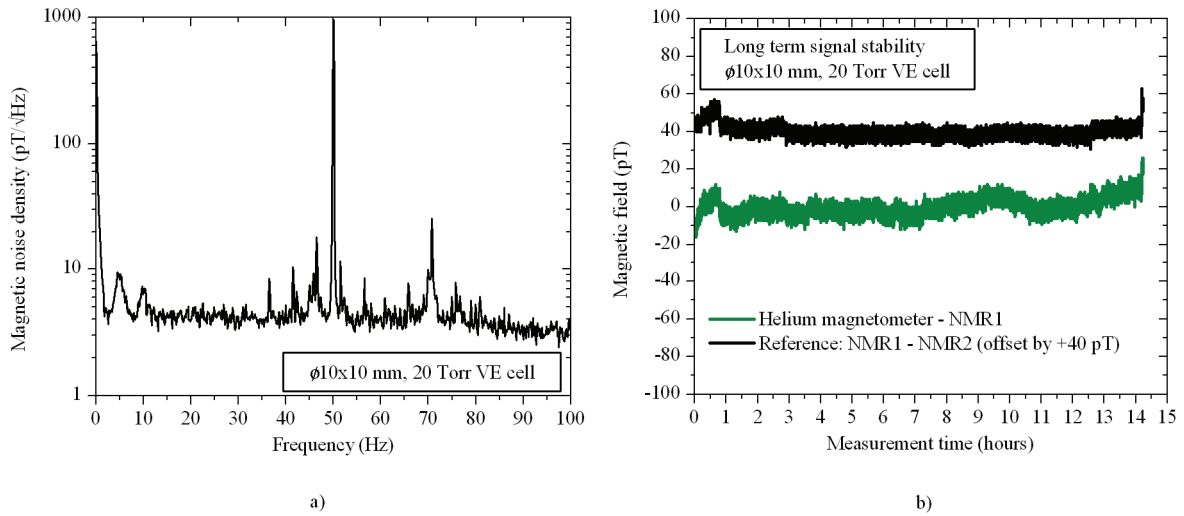


Figure 93. Results obtained with the  $\Phi 10 \times 10$  mm 20 Torr VE cell. a) Magnetic noise density. b) Long term stability.

The long term measurements, conducted with this cell (c.f. Fig. 93b) gave excellent results. The signal is very stable over 14 hours. It exhibits variations of  $\pm 10 \text{ pT}$  over long periods.

#### 4.1.2. Results obtained with the $\Phi 5 \times 5$ mm 20 Torr VE cell

The best value of sensitivity obtained with the  $\Phi 5 \times 5$  20 Torr VE cell is in the order of  $8 \text{ pT}/\sqrt{\text{Hz}}$  (c.f. Fig. 94a). Long term measurements (c.f. Fig. 94b) seem to have similar stability as for the previously described  $\Phi 10 \times 10$  20 Torr VE cell.

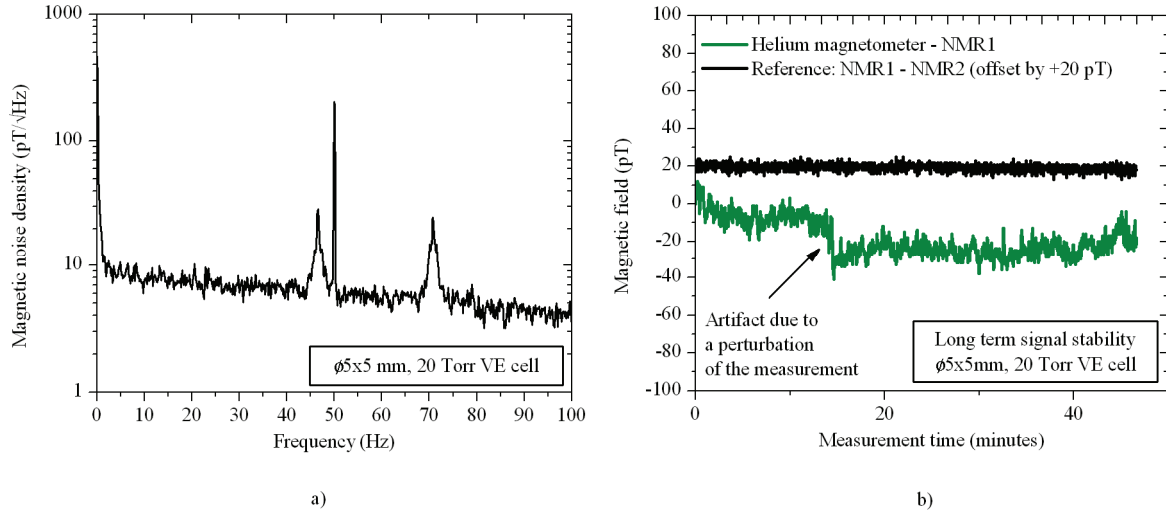


Figure 94. Results obtained with the  $\Phi 5 \times 5$  mm 20 Torr VE cell. a) Magnetic noise density. b) Long term stability.

The steep fall marked in Fig. 94b is caused by the HF discharge electrodes which slightly changed their position during the measurement. This is related with the geometry of the cell, which is not perfectly cylindrical and therefore makes it easy for the glued copper electrodes to come off.

#### 4.1.3. Results obtained with the $\Phi 5 \times 5$ mm 20 Torr GB cell

Maximal value of sensitivity obtained with the  $\Phi 5 \times 5$  20 Torr GB was around  $10 \text{ pT}/\sqrt{\text{Hz}}$  (c.f. Fig. 95a). Long term measurements (c.f. Fig. 95b) showed significant instabilities compared to its VE counterpart.

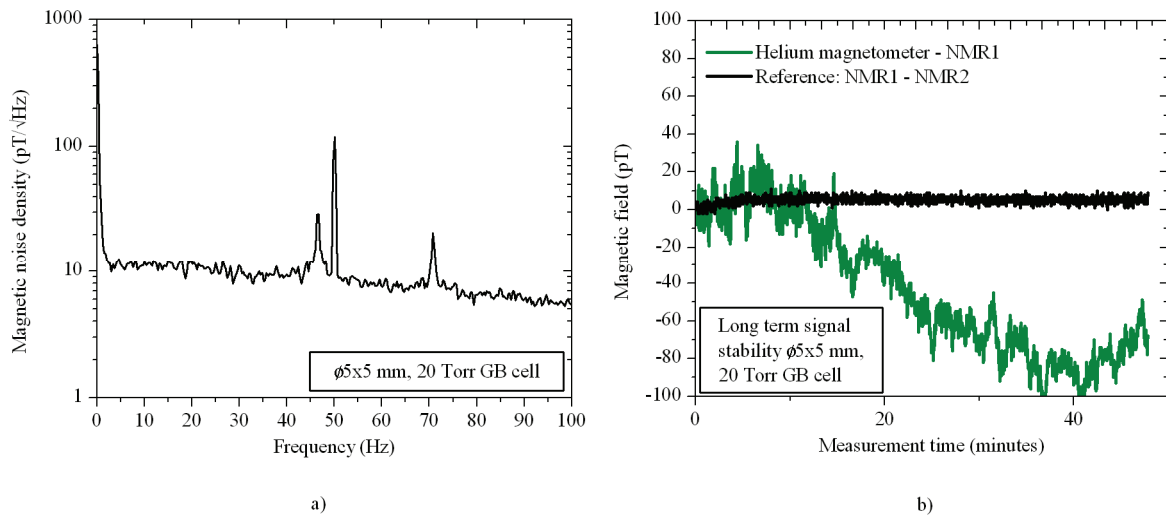


Figure 95. Results obtained with the  $\Phi 5 \times 5$  mm 20 Torr GB cell. a) Magnetic noise density. b) Long term stability.

These instabilities are attributed to the presence of oxygen impurities in the internal atmosphere of the GB cells.



#### 4.1.4. Results obtained with the $\Phi 5 \times 5$ mm 40 and 50 Torr GB cell

The long term measurement for the  $\Phi 5 \times 5$  40 and 50 Torr GB cells was very unstable. The maximal sensitivity obtained with these cells was around 8 and 10  $\text{pT}/\sqrt{\text{Hz}}$ . An influence of a “warm-up” step on the sensitivity has been identified (c.f. Fig. 96).

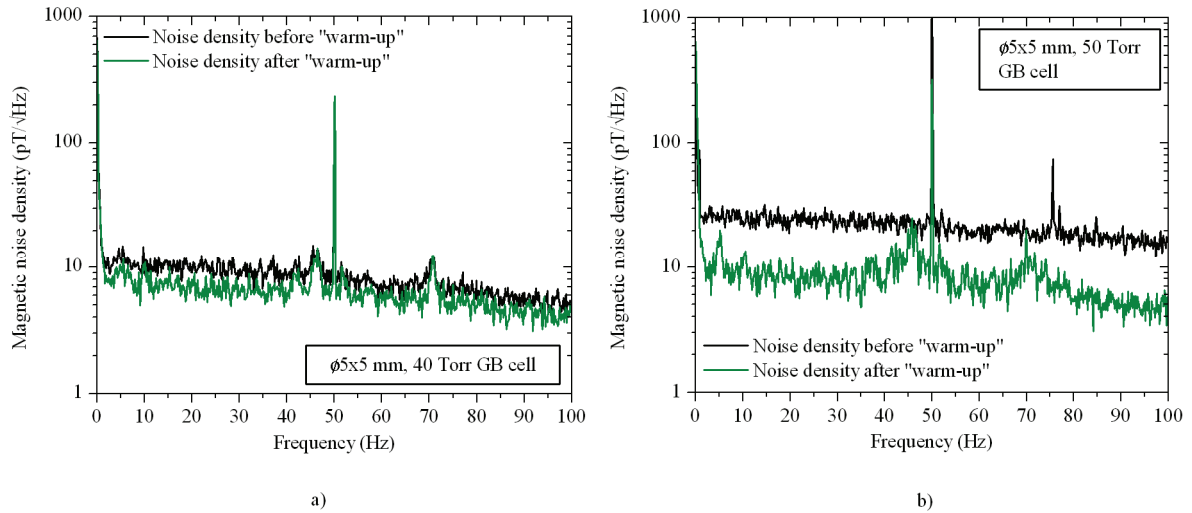


Figure 96. Sensitivity results obtained with the  $\Phi 5 \times 5$  mm 40 Torr GB cell, presenting the influence of the “warm-up”.

This “warm-up” consists of maintaining a high-intensity (in terms of absorbed power) discharge in the cell for some period of time. After this period the HF discharge power is decreased to the extinction limit (area of power generally used in magnetometry). After this procedure the sensitivity is increased although it slowly degrades back with time. This problem seems to be more pronounced for cells filled at higher pressures, e.g. for the 50 Torr cell the difference in sensitivity reached as much as 15-25  $\text{pT}/\sqrt{\text{Hz}}$  (c.f. Fig. 96b compared to Fig. 96a).

#### 4.1.5. Conclusion – VE versus GB cells

Problems with long term stability are identified as a common feature of GB cells. VE cells showed largely better characteristics in this matter.

A short term increase in sensitivity in GB cells after a high-power “warm-up” was found, which seems to be more pronounced at higher pressures.

The exact physical origin of these two phenomena is unclear. It is attributed to the presence of oxygen impurities in the GB cells. As such these cells are not applicable in magnetometry. Nevertheless they allow to make some conclusions on the dependence of maximal sensitivity of the sensor with pressure. Given their largely lower price, much more experimental points can be verified, thus providing a better experimental estimate of the optimal value of pressure for the magnetometer.

Due to the fact that VE cells were not available at the moment of preparation of the final demonstrator, it was decided to use the  $\Phi 5 \times 5$  20 Torr GB cell in its construction. Potentially the performance of the demonstrator could be increased by the use of a 40 Torr  $\Phi 5 \times 5$  mm VE cell, which will be fabricated in the future.

## 4.2. Packaging and system architecture of the final demonstrator

The mechanical packaging of the final demonstrator was designed using the guidelines for the global architecture of the sensor, presented in the previous chapter (c.f. §3). The final packaging of the demonstrator is presented in Fig. 97.

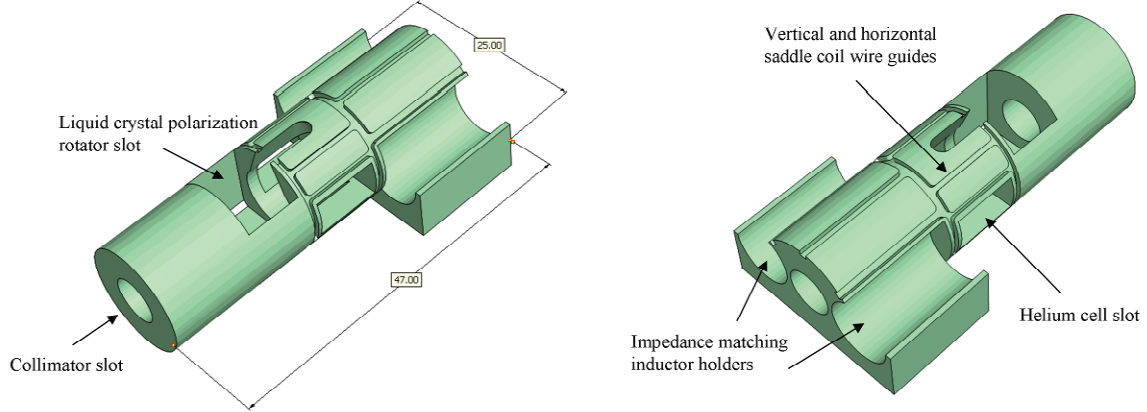


Figure 97. Mechanical packaging of the demonstrator.

As discussed in §1.1.4.4, special attention was paid to the magnetic compatibility of the mechanical parts of the sensor head. The packaging was fabricated by stereolithography. The structural material is a semi-transparent epoxy. The saddle coils are wound manually and fixed using epoxy glue inside the wire guides.

The architecture of the demonstrator is presented in Fig. 98. The pumping light originating from the fiber laser (c.f. §3.3.1.2) is passed by a single mode optical fiber, ending with a pigtailed collimator (c.f. §3.3.2) fixed inside the collimator slot.

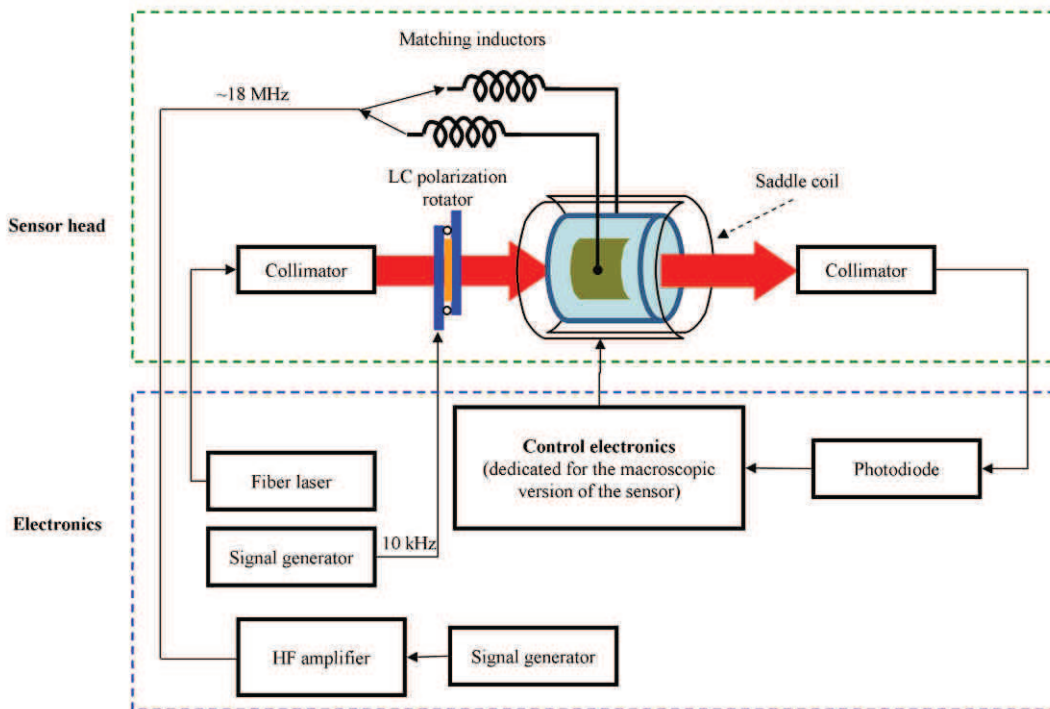


Figure 98. System architecture of the demonstrator.

After passing through the liquid crystal polarization rotator (c.f. §3.5) and the helium cell, the light is collected by another pigtailed collimator and passed on the photodetector. The optical pumping is done in the “single-pass” configuration, which means that the sensor head has collimators and optical fibers on both sides. This solution is rather inconvenient in many applications (e.g. array operation), nevertheless it is the most straightforward way to provide a reliable proof of principle.

The developed sensor itself is presented in Fig. 99, compared to the SWARM sensor. The volume of the sensor head was decreased by more than an order of magnitude.

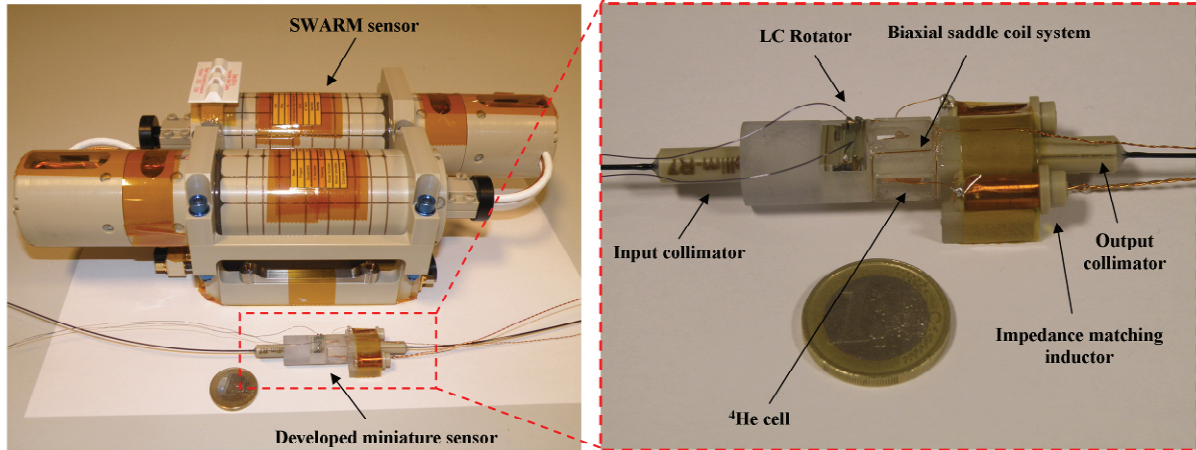


Figure 99. The developed demonstrator compared to the SWARM sensor.

### 4.3. Performance of the demonstrator

The tests were carried out in the configuration presented in Fig. 98.  $LA_2$  signal was used to measure the magnetic field whereas  $LA_1$  served as an error signal in order to manually tune the polarization angle. The amplitude of signal applied across the LC cell is adjusted manually, knowing the direction of the ambient magnetic field  $B_0$  and the LC rotator calibration curve.

The demonstrator attained a sensitivity of  $10 \text{ pT}/\sqrt{\text{Hz}}$  in the frequency range from DC to 100 Hz. The sensitivity of the sensor was also measured without the polarization rotator by manually tuning a linear polarizer (c.f. Fig. 100).

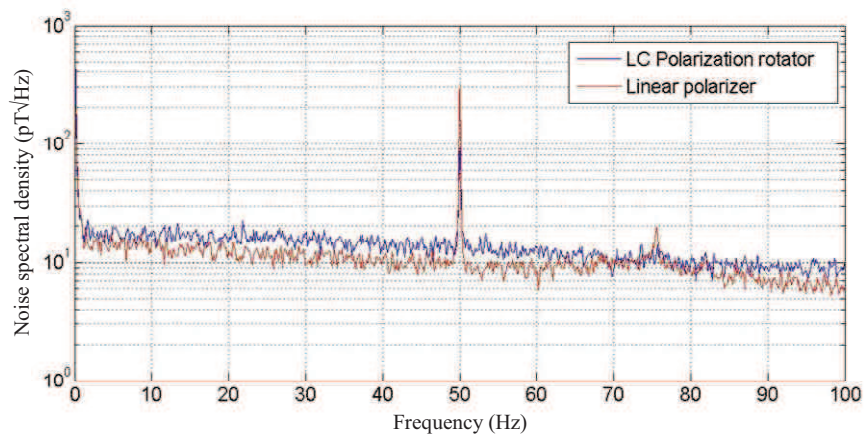


Figure 100. Noise spectral density of the sensor with the LC polarization rotator and with a linear polarizer.

Both measurements gave similar results, which leads to a conclusion that the presence of the polarization rotator does not influence the sensor noise level. These results were obtained with a digital processing unit dedicated to the macroscopic sensor and can be further optimized by developing dedicated electronics, which was out of the scope of this thesis. The performance can possibly be also improved by the use of a 40 Torr  $\Phi 5 \times 5$  mm VE cell.

#### 4.4. Perspectives: first steps towards a chip scale helium magnetometer

The study on further miniaturisation of a helium magnetometer was performed in the course of the European project on miniaturisation of atomic clocks (MAC-TFC - a FP7 project). The key elements of a helium magnetometer are identical, in principle, to those of an atomic clock. This section presents a study on the applicability of certain technological solutions used by the MAC-TFC atomic clock to the future development of a chip-scale helium-4 atomic magnetometer.

Cooperation with FEMTO-ST institute has been established in order to fabricate a glass-silicon-glass microfabricated helium cell structure and validate its applicability for the construction of a miniature helium magnetometer. The key challenge of this study is to verify the possibility of confinement of high-purity helium in a microfabricated structure.

##### 4.4.1. The study on technological solutions for a chip-scale helium magnetometer

Experimental characterization of magnetic properties has been carried out on five key elements used in the construction of a MEMS atomic clock. It provides some conclusions on the possibility of their application in the construction of a chip-scale helium-4 magnetometer. The tested samples, provided by the MAC-TFC consortium, are presented in table 14 along with a brief description.

Table 14. Components characterized in the study. Samples provided by the MAC-TFC consortium.

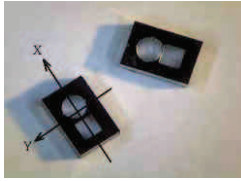
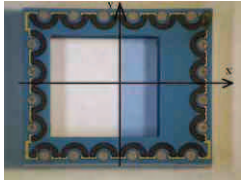
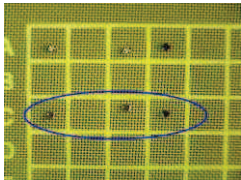
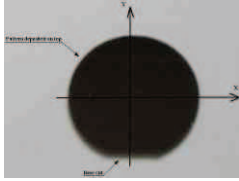
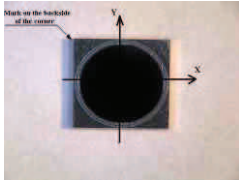
Name	Photo	Number of samples	Description
Microfabricated cells		2	The physics package - glass-silicon-glass vapour cells
LTCC package		1	Packaging solution.
VCSEL lasers		2	Two types of VCSEL laser dies, with different amounts of chromium in the bondpad metallization.

Table 14. Continued.

Name	Photo	Number of samples	Description
Getter film		1	Silicon wafer with a deposited layer of getter material. Getters are used to improve the internal atmosphere purity inside the cells.
Photodiode		1	Silicon photodetector.

#### 4.4.1.1. Measurement

The aim of the magnetic characterization of a component is to quantify its minimal separation from the sensing element within which it does not cause significant perturbations to the measurement. The components are positioned as close to the magnetometer as possible ( $\sim 2$  mm in practice). Scalar sensor measures the projection of the field emitted by the sample onto the Earth's magnetic field. By repeating the measurement in several orthogonal positions, three components of the sample's magnetic moment can be determined. Given the small size of the samples, it was chosen to carry out the measurement with the use of the  $\Phi 5 \times 5$  mm 20 Torr GB cell.

The Earth's magnetic field (close to  $50 \mu\text{T}$  in France) can vary up to a few tens of nT in ten minutes. This variation is much higher than the accuracy required for this characterization. To reject these magnetic field variations, it was chosen to use a differential mode of measurement: the gradiometer configuration (c.f. Fig. 101). Both magnetometers see the same Earth's field variation whereas only one of them measures the magnetic field produced by the component.

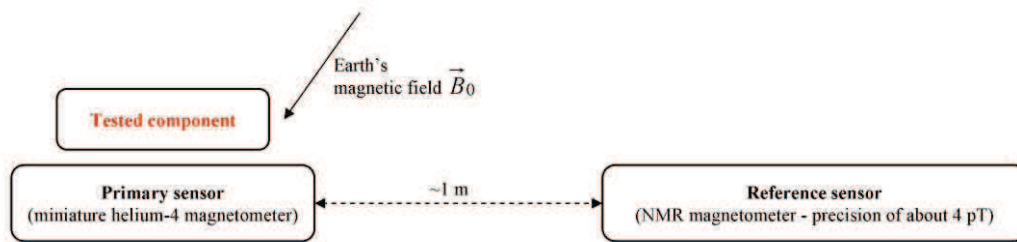


Figure 101. The gradiometer configuration used during the measurement.

The assembled setup used for the measurement is presented in Fig. 102. It consists of a non-magnetic support containing RF coils, two collimators (c.f. §3.3.2), a resonant discharge circuit with an impedance adapting transformer (c.f. Fig. 26) and a non-magnetic sample mount. It is a bench-top setup which allows to place the samples very close to the helium cell. The samples to be measured were placed at the tip of wooden tweezers attached to the sample mount and were approached as close to the helium cell as possible. In practice a distance of about 2 mm was used.



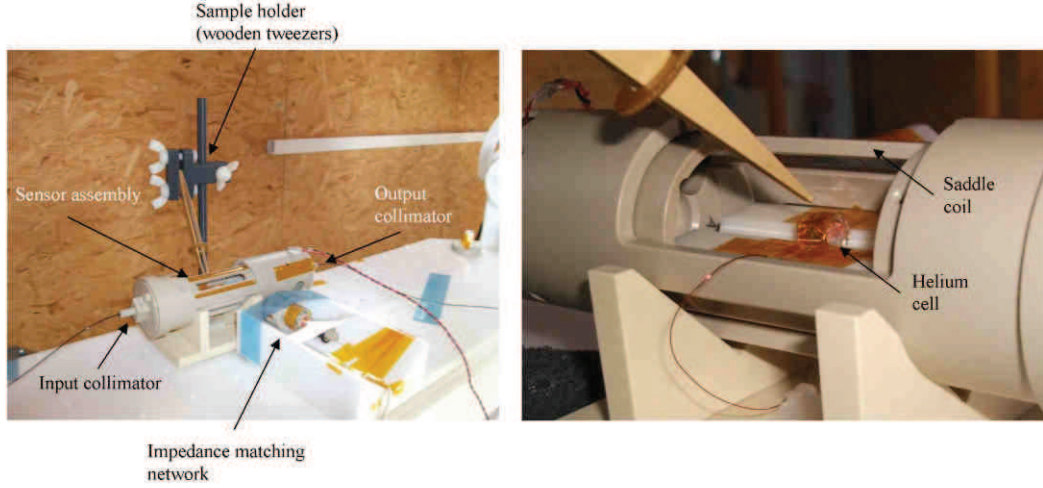


Figure 102. Setup used to characterize the magnetic properties of components.

This distance is imposed by the fact that conductive objects placed closer to the cell caused the discharge to extinguish (due to a short circuit between the electrodes).

#### 4.4.1.2. Results

The constraints on magnetic properties of the solutions applied for atomic magnetometers are much stricter compared to those for atomic clocks. Any magnetic default of a component applied in the construction of a magnetometer can lead to degradation of accuracy. Therefore to achieve the specified accuracy of 50 pT, the choice of materials at the conception stage is mandatory. Its practical realization needs a detailed characterization of the available solutions. The actual confidence interval obtained in this measurement was limited to 20 pT. This value is sufficient to allow some preliminary conclusions and to define a general architecture for the chip-scale sensor.

The results of measurements, carried out on the samples are presented in table 15. The corresponding minimal spacing of the components, allowing to obtain a value of magnetic fields inferior to 20 pT at the sensing element is presented in Fig. 103.

Table 15. Measurement results

Component	$ \vec{B} $ at 2 mm (pT)
Microfabricated cell	< 20
LTCC package	< 20
VCSEL die (600 $\mu\text{m}$ thick Ni layer in the bondpad metallization)	210
VCSEL die (250 $\mu\text{m}$ thick Ni layer in the bondpad metallization)	< 20
Getter film	50
Photodiode	110

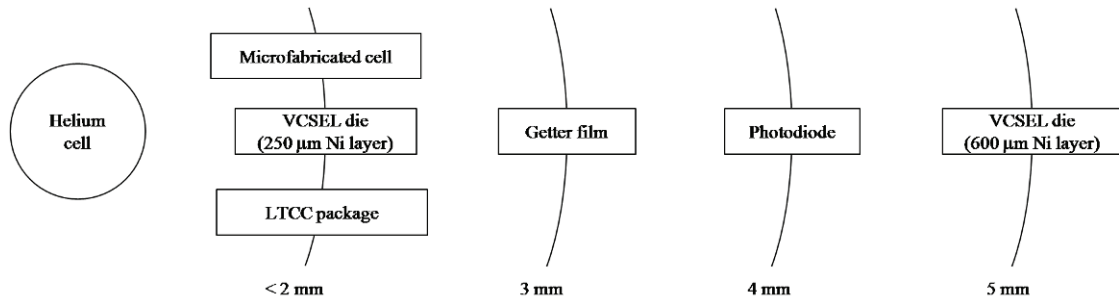


Figure 103. Minimal spacing of the components of the MAC-TFC atomic clock as applied in the construction of a magnetometer.

#### 4.4.1.3. Conclusion – applicability in the construction of a micro-scale helium-4 magnetometer

The results obtained in this section give some preliminary conclusions on the general architecture of a micro-scale helium-4 magnetometer and clearly show some directions for further development.

The microfabricated glass-silicon-glass cells tested in the study were demonstrated to be completely non-magnetic, which along with other advantages like compatibility with batch processing makes them a good candidate for a replacement of traditional glassblown helium cells. This solution will be studied further in the next section.

The magnetic properties of VCSEL dies strongly depend on the content of ferromagnetic materials in its structure. Even though the actual size of the dies is very small compared to the dimensions of the helium cell used during the measurement, the influence of nickel is clearly visible. The VCSELs were characterized statically i.e. without passing electrical current through the structure. This current (typically tens of mA DC) can have a significant influence on the measurement. Along with the fact that the characterized photodetector also has a non-negligible magnetic signature, it seems reasonable to separate the laser source and the photodetector from the sensor head. This solution is employed in most of the state of the art constructions (c.f. §1.2). It is mandatory if the measurement accuracy is an important factor in a given application.

The relatively small magnetic signature of the getter film is most probably related with the large dimensions of the sample, which consisted of a whole silicon wafer with the getter deposited on top. The amount practically used in the construction of a physics package shouldn't cause significant magnetic perturbations.

As for the packaging solution, used by the MAC-TFC atomic clock, LTCC seems to be very well adapted also for the needs of a helium magnetometer. The characterized sample had a negligible magnetic signature. Taking into account the fact that this technology is cheap and very well adapted to small and medium-scale production, it seems a very good candidate for a micro-scale packaging solution for the future version of the sensor.

#### 4.4.2. Microfabricated helium cells

Microfabricated glass-silicon-glass helium cells have been prepared in cooperation with FEMTO-ST institute. Their application in the construction of a miniature helium magnetometer will be verified experimentally. The key challenge of this study is to validate the possibility of confinement of high-purity helium in a microfabricated structure.

#### 4.4.2.1. Disadvantages of miniature glassblown cells

Apart from the high cost of production and limited miniaturization potential, miniature glassblown cells suffer from several technological problems, which make their practical use somewhat more difficult than macroscopic ones. The first problem arises during the packaging of the sensor. The glass tip, which is left after cutting off the cells from the vacuum system (c.f. Fig. 104a), has a random geometry. This imposes a custom design of packaging, in order to adapt it to each individual cell.

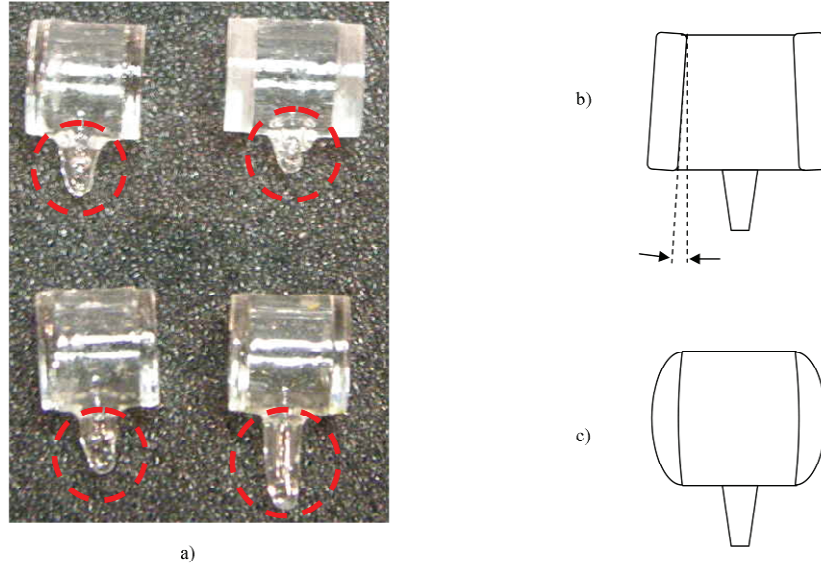


Figure 104. a) Four sample  $\Phi 5 \times 5$  mm helium cells, presenting different geometries of the tip (marked red). b) Angular misalignment between the optical faces of the cell. c) Distortion of the optical faces.

The second very important problem is related with the coupling of pumping light into the cell. There are several types of defects, which often occur in the optical faces of the cells, like angular misalignment (c.f. Fig. 104b) or distortion of the whole face (c.f. Fig. 104c). Another type of defect, identified in some of the cells is related with gas bubbles trapped inside the glass (c.f. Fig. 105).

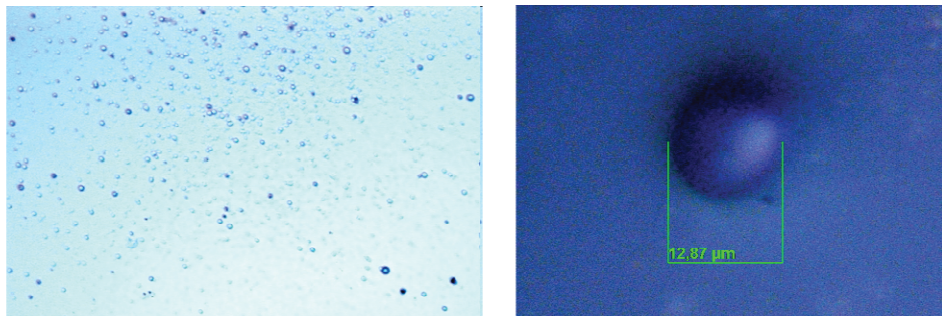


Figure 105. Gas bubbles trapped inside the glass of the optical face of the  $\Phi 5 \times 5$  mm 20 Torr VE cell.

All of these defects degrade the light transmission through the cell and therefore increase the optical power necessary at the input in order to obtain appropriate signal amplitude.

The disadvantages presented above are inherently related with the manual character of the fabrication of cells. What is more, the smaller the dimensions of the cell, the more time-consuming, laborious and uncertain the outcome of the fabrication process becomes. An ideal solution to this



problem consists of applying batch processing techniques issued from the semiconductor industry. These techniques allow a predictable yield and perfect repeatability of the fabrication process.

#### 4.4.2.2. Fabrication procedure

A batch of microfabricated glass-silicon-glass helium-filled cells has been fabricated. The technology of their fabrication is identical to the one developed and presented by the FEMTO-ST institute [60][61]. It is presented schematically in Fig. 106.

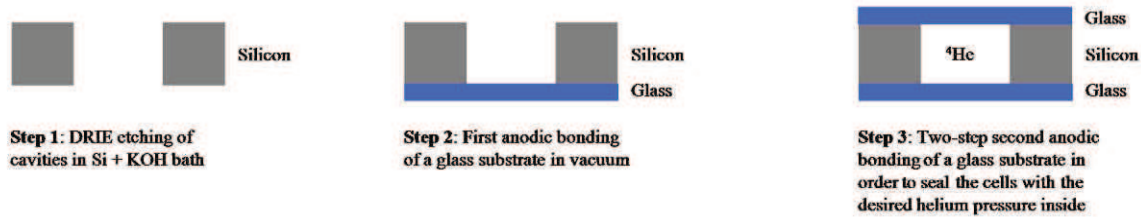


Figure 106. Processing steps used to prepare the microfabricated helium cells.

In the first step, through-wafer cavities of 2 mm in diameter are dry etched in a 1.3 mm thick, 4'' (100)-oriented silicon substrate. In order to eliminate the defects and fluorocarbon deposits left on the sidewalls of the structure after the DRIE process, the substrate is immersed in an aqueous KOH solution for 30 min [61].

After cleaning, this silicon wafer is anodically bonded to a first 500  $\mu\text{m}$  borosilicate substrate in the second step.

In the final step the cells are filled with helium-4 at the desired pressure and sealed hermetically with a second borosilicate substrate. Due to a relatively small breakdown voltage inside the vacuum chamber filled with helium, this step is rather complex [61]. Its process flow is presented in table 16.

Table 16. Process flow of the hermetic sealing step, based on [61].

Order	Process
1	Annealing of wafers (350°C, in vacuum)
2	Cooling to room temperature
3	Introduction of gas at the appropriate pressure (helium-4)
4	Removal of separation flags – the second glass substrate is brought into direct contact with the glass-silicon perform.
5	Application of contact force on the triple-stacked structure.
6	Heating (to 350°C)
7	Pre-sealing – anodic bonding in helium atmosphere (bonding voltage < breakdown voltage)
8	Backfilling of the chamber with air
9	Reinforcing sealing – anodic bonding in air (600 and 900 V)

First, the triple-stacked structure (glass-silicon-glass) is pre-sealed by anodic bonding in a chamber filled with helium-4 gas at the desired pressure (50 Torr). The bonding voltage has to be lower than the breakdown voltage of the gas atmosphere inside the chamber. This process does not allow to

obtain a reliable bond between the substrates (voltage too low) therefore the vacuum chamber is backfilled with air and a reinforcing sealing process is applied. It consists of anodic bonding carried out in air. At first the bonding voltage of 600 V is applied for 5 min, afterwards the voltage is increased to 900 V and maintained for 20 min. This process allows a proper hermetization of the cells.

The resulting structures are presented in Fig. 107 compared to a miniature  $\Phi 5 \times 5$  mm version of a glassblown cell.



Figure 107. Microfabricated helium-4 cells compared to a miniature  $\Phi 5 \times 5$  mm glassblown cell.

#### 4.4.2.3. Characterization – proof of concept of helium confinement

The presence of helium inside microfabricated cells and internal gas purity have been inspected by optical emission spectroscopy. This was done by establishing a discharge inside the cells with two ITO-coated glass electrodes brought into direct contact with the structure (c.f. Fig. 108a and 108b).

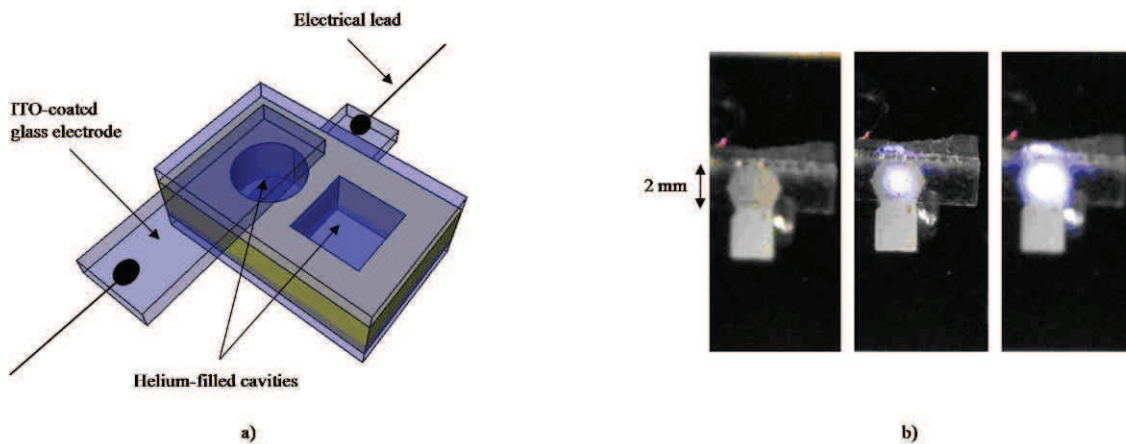


Figure 108. a) Discharge excitation scheme. b) Discharge ignited in a microfabricated helium cell.

They are symmetrically driven with a HF signal supplied by an RF amplifier followed by a resonant impedance matching network (c.f. §2.4.2). The impedance matching is slightly worse than in the case of glassblown cells (c.f. Fig. 109a) which is caused by the additional impedance of ITO and a conductive polymer used to form an electrical contact between the leads and the ITO layer.

The emitted light is coupled into an optical fiber and sent to a spectrometer. Spectral characteristics for each cell are analyzed using the NIST Spectral Database (c.f. Fig. 109b). Hermetic confinement of helium inside those microfabricated cells is confirmed.

Unfortunately spectroscopy measurements have also revealed the presence of oxygen inside the cells. This is likely related to an insufficient vacuum level inside the bonding chamber before filling with helium. This problem could be resolved with the use of a turbo-molecular vacuum pump and the incorporation of a getter film into the physics package.

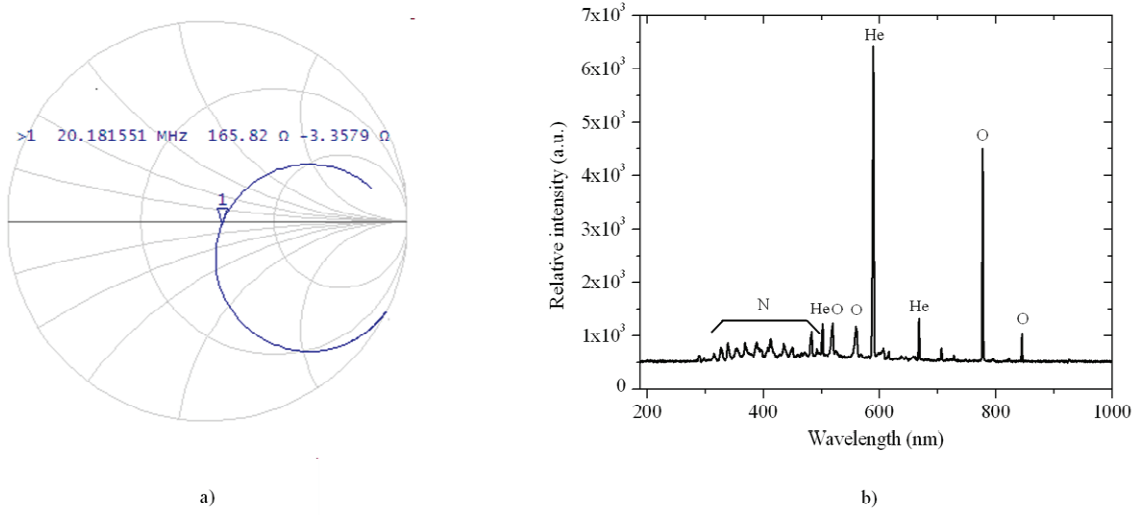


Figure 109. a) Smith's chart showing the impedance matching of the circuit. b) Emission spectrum of the discharge proving the presence of helium-4 inside the microfabricated cells.

#### 4.4.2.4. Limitations and further perspectives

The discharge ignited in microfabricated cells is very unstable and difficult to maintain. What is more, the amount of absorbed power necessary for the ignition of plasma ranged between 1 and 2 W. This value is an order of magnitude higher than the power used to obtain stable helium plasma with larger glassblown cells. The influence of silicon layer on the electric field distribution, which was initially suspected to have caused this problem, was modelled numerically. The distribution in case of an all glass cell is presented in Fig. 110a. The difference in distribution as compared with the glass-silicon-glass cell (c.f. Fig. 110b) is not very pronounced, yet has a non-negligible influence.

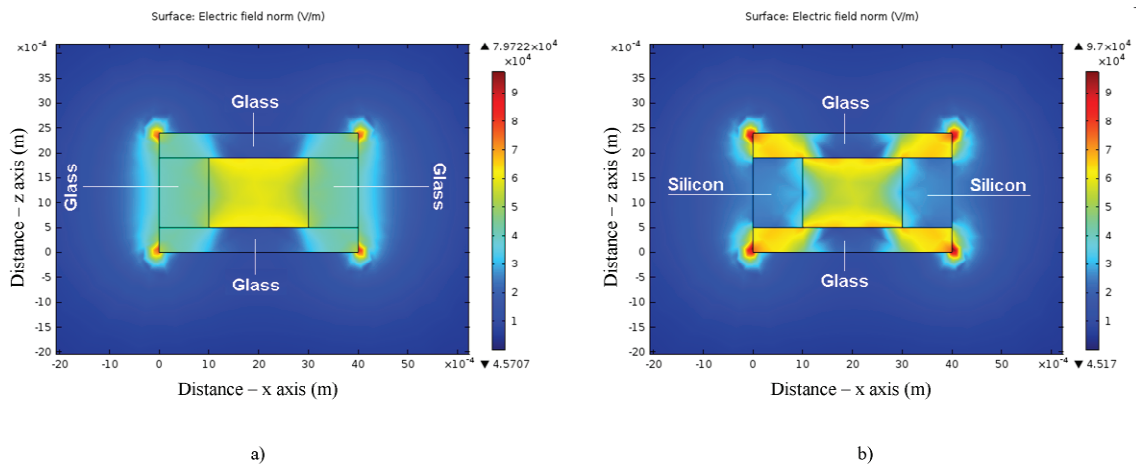


Figure 110. Finite element simulation of the electric field distribution (with Comsol Multiphysics). 100 V is applied on the top boundary, the bottom boundary is grounded. a) Case of an all-glass cell. b) Case of a glass-silicon-glass cell.

The high breakdown power is probably a resultant of two phenomena. The first of which is the presence of oxygen atoms inside the microfabricated cells. Indeed, Park et al. [31] have shown that the breakdown voltage increases very rapidly when a substantial fraction of oxygen is added to helium. The second could be related to scaling effects occurring in the plasma physics. Breakdown voltage increases when diffusion is not the dominant electron loss mechanism, as described earlier (c.f. §2.5).

In order to obtain an estimate of metastable density in the discharge ignited in the presented microfabricated cells a numerical simulation was done, using the algorithm presented in §2.7.1.1. The power dissipated into the discharge was assumed to be the same as for  $\Phi 5 \times 5$  mm cells (5 mW). The electrode separation is set to 1.3 mm (the thickness of the silicon wafer). Results, obtained for the value of pressure used in the cells (50 Torr), suggest a value of metastable atom density in the order of  $1 \cdot 10^{12} \text{ cm}^{-3}$  (c.f. Fig. 111a).

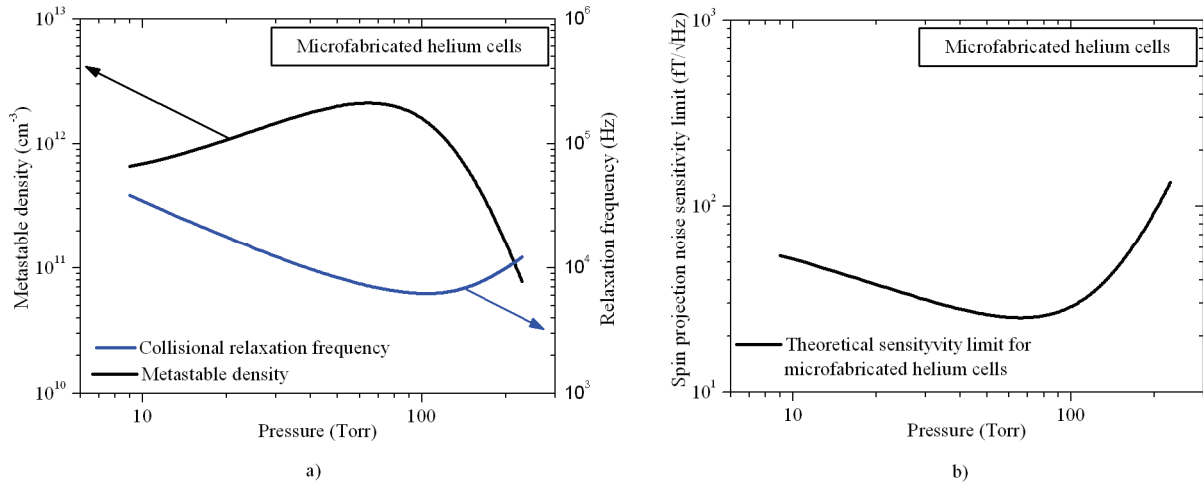


Figure 111. Results of a numerical simulation (c.f. §2.7.1.1) of discharge parameters for the case of the presented microfabricated helium cell. a) Metastable density and relaxation frequencies. b) Spin projection noise sensitivity limit.

This value would result in ~8% absorption of light (at the D<sub>0</sub> line) passing through the cell. The optimal value of pressure is estimated to lie in the 60 – 90 Torr range (c.f. Fig. 111b).

The value of absorption was investigated experimentally. The measurement was realized with a dedicated polymer mount (c.f. Fig. 112), which was used to align the ITO electrodes and input/output collimators.

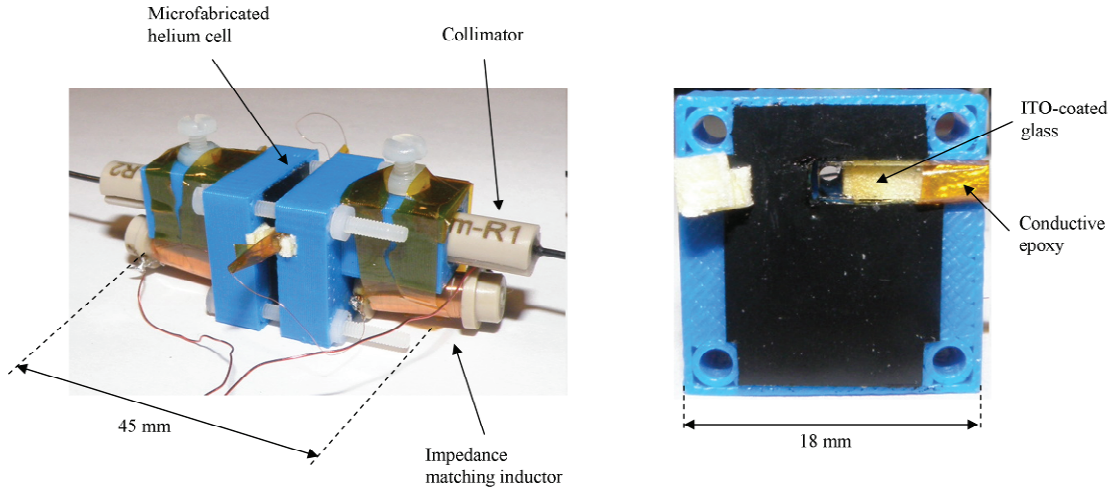


Figure 112. Polymer mount dedicated for absorption measurements in microfabricated helium cells.

Unfortunately the absorption (and thus metastable atom density) was found to have a value below the detection limit of the system used ( $\sim 0.5\%$ ). This fact is most probably related to the destruction of  $2^3S_1$  metastable atoms by excited oxygen atoms.

Further experimental work on the technology of microfabricated helium cells should resolve two problems. First of which is the improvement of the internal atmosphere purity, which is essential for the development of the sensor, since for the moment the value of metastable density in the discharge is below the detection limit.

The second problem, which needs to be addressed, is the high power consumption. The first attempt to resolve this issue would be to increase the internal pressure inside the samples, which would eliminate the possibility that the high power consumption is related with the fact that the breakdown process is drift-driven.

#### 4.4.3. Concept of a chip scale helium magnetometer

Although the technology behind microfabricated helium-4 cells still needs a lot of development, first proof-of-principle has been presented. The results obtained up to date allow to draw some guidelines on a general architecture of a future micro-scale isotropic helium-4 magnetometer.

##### 4.4.3.1. Optical architecture

The optical aperture of microfabricated cells is a lot smaller compared to glassblown ones. Consequently, this creates a need for further miniaturization of the optical architecture. A solution well adapted to this issue is the use of gradient-index (GRIN) optics in the collimator construction. Three possible configurations of this type can be distinguished. They are presented in Fig. 113.

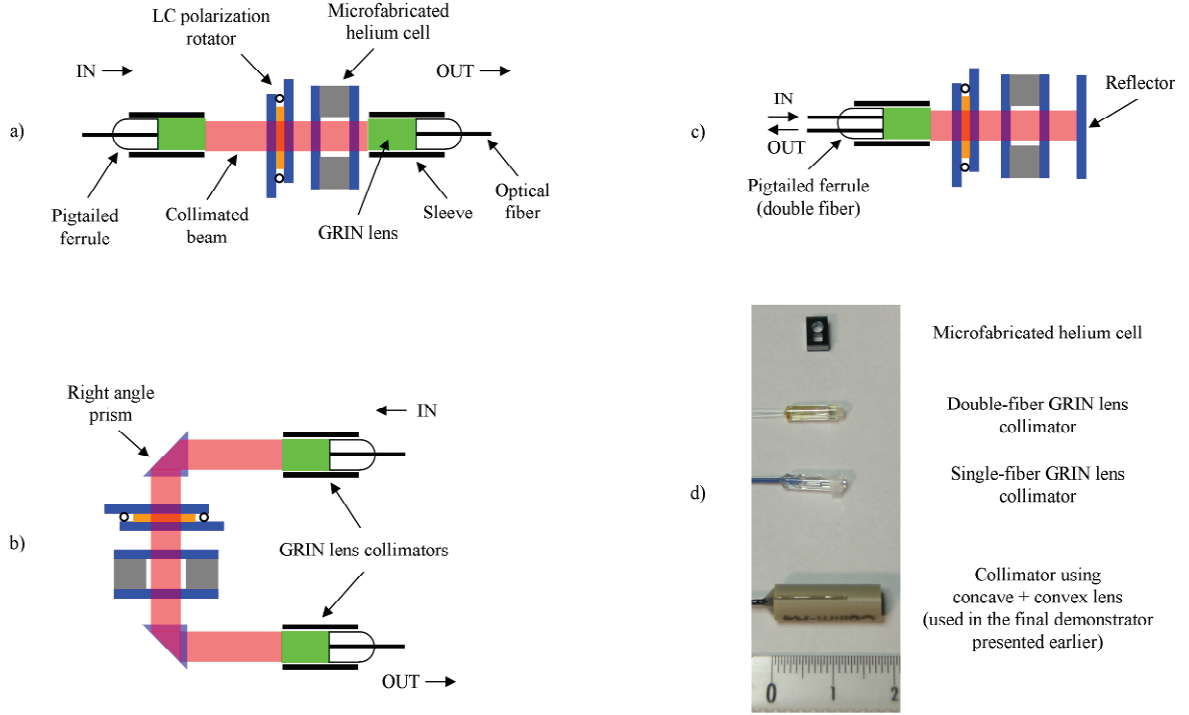


Figure 113. Optical architecture using GRIN lens. a) In-line configuration, using single-fiber GRIN lens collimators. b) Folded configuration, using single-fiber GRIN lens collimators. c) Reflective configuration, using a double-fiber GRIN lens collimator. d) Comparison of three collimator types.

In-line (c.f. Fig. 113a) and folded (c.f. Fig. 113b) configurations use two single-fiber GRIN lens collimators whereas the reflective configuration (c.f. Fig. 113c) is composed of a single double-fiber GRIN lens collimator. Both elements are presented in Fig. 113d, compared to a microfabricated helium cell and a previously discussed concave+convex lens collimator (c.f. §3.3.2).

The application of GRIN optics in the construction of miniature, high-sensitivity atomic magnetometers has already been reported several times in literature, which means that this solution is compatible with the construction of a chip-scale helium magnetometer.

#### 4.4.3.2. Integration of the liquid crystal polarization rotator

The construction of the liquid crystal polarization rotator and its fabrication technology are fully compatible with batch processing. This allows to integrate the rotator with a microfabricated helium-4 cell, once its fabrication technology reaches sufficient maturity. A concept of such an integrated structure is presented in Fig. 114. In this construction the discharge would be ignited by means of ITO electrodes deposited on glass. The LC rotator and helium cell are integrated into one structure, which can be packaged along with other optical components (of one of the proposed optical architectures - c.f. Fig. 113) using thick-film LTCC technology.



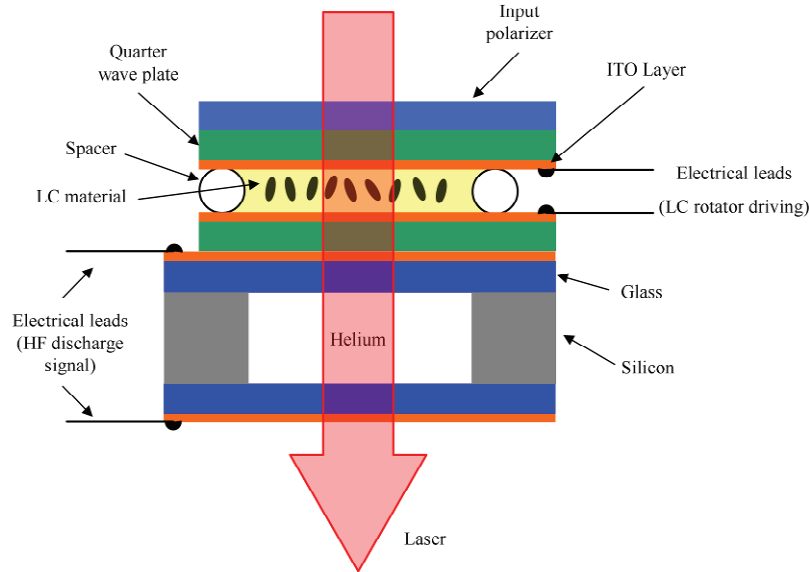


Figure 114. Concept of a microfabricated helium cell integrated with a liquid crystal (LC) polarization rotator.

## 4.5. Conclusion

A first demonstrator of an isotropic helium-4 atomic magnetometer has been presented. The sensor reaches a sensitivity of  $10 \text{ pT}/\sqrt{\text{Hz}}$ , which is subject to further optimization. Another possible improvement in terms of sensitivity and stability of measurement could be obtained by using a  $\Phi 5 \times 5 \text{ mm}$  40 Torr VE cell, which will be done during the further development of the sensor.

The isotropy of measurement of the demonstrator is provided by a liquid crystal polarization rotator, a solution which is proven non-magnetic and thus suitable for magnetometry applications. Although a detailed characterization of accuracy of the sensor is still to be done, the results obtained up to date show that all the developed building blocks can be successfully applied in the construction of a high-performance isotropic helium-4 magnetometer.

A concept of further miniaturization of the sensor is provided. Most of the key elements used previously in the construction of an atomic clock (developed by the MAC-TFC consortium) are found to be compatible with the requirements of an atomic magnetometer. First proof-of-principle of helium confinement in a microfabricated glass-silicon-glass structure is given. This paves the way for future development of a chip-scale isotropic helium-4 magnetometer.





## **Conclusion**



## Conclusion

The miniaturization of an isotropic helium-4 atomic magnetometer is a complex task which requires a multidisciplinary approach. It involves plasma physics and optics as well as electrical and mechanical engineering. The SWARM magnetometer developed at the laboratory was referenced as the starting point for this process.

The most important task is to determine how the behavior and characteristics of the sensor change along with its decreasing dimensions. The optimal value of helium pressure, with which the sensor's cells are filled, is bounded from the low and high-pressure side by phenomena taking place in the discharge. If this value is too low, the discharge is difficult to ignite and unstable. From the high-pressure side this value is limited by the decreasing electron temperature and collisions between metastable and neutral helium atoms. Optimal values of pressure of 20 and 40 Torr were experimentally found for  $\Phi 10 \times 10$  mm and  $\Phi 5 \times 5$  mm cells respectively.

Some applications, like unexploded ordnance detection, need array operation of magnetometers. Magnetometers using RF magnetic field to induce resonance in the atomic media are known to suffer from crosstalk. All-optical magnetometers do not experience such problems. For this purpose a study of angular characteristics of optically excited resonance signals has been done (the OSP scheme). A convenient operating point for the isotropy-providing mechanism is found for a frequency-modulated all-optical helium magnetometer.

Economic aspects, like unit cost reduction, inherently related with the miniaturization process, are also of great concern. The most expensive element of the sensor is the pumping source. The fiber laser used by the SWARM magnetometer is a very sophisticated construction. Its high performance and reliability come at the expense of high cost, complexity and large size. What is more, in practice this solution is impossible to miniaturize. An ideal replacement consists of a single mode semiconductor diode. The applicability of two types of diodes was tested. First of which is a commercial edge emitting DFB laser. Unfortunately its noise characteristics cause instabilities in the long term performance of the sensor. Several problems still need to be addressed like the elimination of optical feedback and electronic noise reduction. A solution which is even more appealing, in terms of low unit cost, is the application of VCSEL lasers. Dedicated VCSELs were developed and characterized. Obtained results are very promising although this solution still needs a long path of development.

Miniaturization of the sensitive element triggers the need to miniaturize all of its surrounding components. The most problematic element is the polarization rotation system, used to enable an isotropic measurement of magnetic field. It was found that a polarization rotator based on liquid crystals is a very good replacement of the piezoelectric motor used in the construction of the SWARM magnetometer. Contrary to the former solution, it does not contain any mechanical parts, allows integration and relatively easy further miniaturization. What is more, it was confirmed that the application of this element in the construction of a magnetometer does not change the sensitivity of the sensor. This leads to conclude that this solution as well as its electrical driving scheme are non-magnetic and thus adapted to magnetometry applications.

The maximal values of sensitivity, obtained with miniature helium cells were around 3.5 and 8 pT/Hz for 20 Torr  $\Phi 10 \times 10$  mm VE and 40 Torr  $\Phi 5 \times 5$  mm GB cells respectively. In terms of stability, excellent results were obtained with a 20 Torr  $\Phi 10 \times 10$  mm VE cell, for which the fluctuations were in the range of  $\pm 10$  pT over very long periods of time. A significant influence of trace impurities of oxygen present in the internal atmosphere of GB cells on the stability of measurement has been found. This proves that much attention should be paid to the filling process and validates the filling procedure developed at CEA-LETI. This tends to suggest that the sensitivity

obtained with  $\Phi 5 \times 5$  mm cells can be improved by the use of a 40 Torr cell filled according to this procedure.

A demonstrator of a miniature isotropic helium-4 magnetometer has been presented. The sensor uses a  $\Phi 5 \times 5$  mm glassblown cell and reaches a sensitivity of  $10 \text{ pT}/\sqrt{\text{Hz}}$ . Its isotropy is provided by a liquid crystal polarization rotator. The sensor head is more than an order of magnitude smaller compared to the SWARM sensor. These results are subject to further optimization by the development of dedicated electronics. Further work on the demonstrator will concern a detailed characterization of its anisotropy and accuracy, although all of the building blocks of the demonstrator are proven to be well adapted to the application in a high performance isotropic helium-4 magnetometer.

Finally, a concept of a chip-scale helium magnetometer is presented. The applicability of several key technological solutions used in an earlier construction of a microfabricated atomic clock has been validated. Furthermore a batch of microfabricated helium cells has been tested. A proof-of-principle of a microfabricated helium cell is provided. Even though there still remain several important technological challenges, which need to be addressed, this work lays the groundwork for further miniaturization of the sensor.

## Literature

- [1] S. Knappe, "Emerging Topics: MEMS Atomic Clocks," in *Comprehensive Microsystems*, vol. 3, Elsevier, 2007, pp. 571–612.
- [2] R. Mhaskar, S. Knappe, and J. Kitching, "A low-power, high-sensitivity micromachined optical magnetometer," *Appl. Phys. Lett.*, vol. 101, no. 24, pp. 241105–241105–4, Dec. 2012.
- [3] P. D. D. Schwindt, S. Knappe, V. Shah, L. Hollberg, J. Kitching, L.-A. Liew, and J. Moreland, "Chip-scale atomic magnetometer," *Appl. Phys. Lett.*, vol. 85, no. 26, pp. 6409–6411, Dec. 2004.
- [4] D. Budker and D. F. J. Kimball, *Optical Magnetometry*. Cambridge University Press, 2013.
- [5] J. M. Leger, "Magnétométrie à pompage optique: conception, réalisation et évaluation des performances d'un magnétomètre scalaire utilisant l'hélium 4 pompé par un laser LNA," Ph.D. thesis, Grenoble, 1990.
- [6] M. K. Plante, "A Generalized Theory of Double-Resonance Laser-Pumped Helium-4 Magnetometers," Ph.D. thesis, University of Texas at Dallas, August, 2010.
- [7] M. K. Plante, D. L. MacFarlane, D. D. McGregor, R. E. Slocum, W. M. Sampson, and A. W. Brown, "Generalized theory of double-resonance optical pumping of  $^4\text{He}$ ," *Phys. Rev. A*, vol. 82, no. 1, p. 013837, Jul. 2010.
- [8] A. Kastler, "Quelques suggestions concernant la production optique et la détection optique d'une inégalité de population des niveaux de quantification spatiale des atomes. Application à l'expérience de Stern et Gerlach et à la résonance magnétique," *J. Phys. Radium*, vol. 11, no. 6, pp. 255–265, 1950.
- [9] C. Cohen-Tannoudji, "Théorie quantique du cycle de pompage optique," Ph. D. thesis, Ann. Phys. Paris 7, 423 et 469 (1962).
- [10] C. Guttin, "Etude et réalisation d'un magnétomètre à hélium 4 pompé par laser à haute résolution et isotrope," Ph.D. thesis, Grenoble 1995.
- [11] T. Jager, J.-M. Léger, F. Bertrand, I. Fratter, and J.-C. Lalaurie, "SWARM Absolute Scalar Magnetometer accuracy: Analyses and measurement results," in *2010 IEEE Sensors*, 2010, pp. 2392–2395.
- [12] A. R. Keyser, J. A. Rice, and L. D. Scheerer, "A metastable helium magnetometer for observing small geomagnetic fluctuations," *J. Geophys. Res.*, vol. 66, no. 12, pp. 4163–4169, 1961.
- [13] R. E. Slocum, "Laser Magnetometry Using DBR Laser Pumped Helium Isotopes: Beyond 'Juno at Jupiter.'" LEOS, 2008.
- [14] R. E. Slocum and L. Ryan, "Self-Calibrating Vector Magnetometer for Space," presented at the ESTC, 2002.
- [15] A. Pollinger, R. Lammegger, W. Magnes, M. Ellmeier, W. Baumjohann, M. Volwerk, L. Windholz, and M. Dougherty, "CDSM – A New Scalar Magnetometer," presented at the EJSIM Instrument Workshop, 2010.
- [16] P. D. D. Schwindt, B. Lindseth, S. Knappe, V. Shah, J. Kitching, and L.-A. Liew, "Chip-scale atomic magnetometer with improved sensitivity by use of the Mx technique," *Appl. Phys. Lett.*, vol. 90, no. 8, pp. 081102–081102–3, Feb. 2007.
- [17] V. Schultze, R. IJsselsteijn, T. Scholtes, S. Woetzel, and H.-G. Meyer, "Characteristics and performance of an intensity-modulated optically pumped magnetometer in comparison to the classical Mx magnetometer," *Opt. Express*, vol. 20, no. 13, pp. 14201–14212, Jun. 2012.
- [18] J. Preusser, S. Knappe, J. Kitching, and V. Gerginov, "A microfabricated photonic magnetometer," in *Frequency Control Symposium, 2009 Joint with the 22nd European Frequency and Time forum. IEEE International*, 2009, pp. 1180–1182.
- [19] R. IJsselsteijn, M. Kielpinski, S. Woetzel, T. Scholtes, E. Kessler, R. Stolz, V. Schultze, and H.-G. Meyer, "A full optically operated magnetometer array: An experimental study," *Rev. Sci. Instrum.*, vol. 83, no. 11, pp. 113106–113106–7, Nov. 2012.
- [20] "High sensitivity potassium magnetometer." [Online]. Available: <http://physics.princeton.edu/romalis/magnetometer/>. [Accessed: 14-May-2013].
- [21] R. Wyllie, M. Kauer, G. S. Smetana, R. T. Wakai, and T. G. Walker, "Magnetocardiography with a modular spin-exchange relaxation-free atomic magnetometer array," *Phys. Med. Biol.*, vol. 57, no. 9, pp. 2619–2632, May 2012.

- [22] “Twinleaf Compact vector magnetometer SERF-2.” [Online]. Available: <http://www.twinleaf.com/magnetometer/vector/SERF-2/>. [Accessed: 14-May-2013].
- [23] “Twinleaf — Compact scalar magnetometer — SAM-2.” [Online]. Available: <http://www.twinleaf.com/magnetometer/scalar/SAM-2/>. [Accessed: 14-May-2013].
- [24] M. Prouty, “Development of a Micro-Fabricated Total-Field Magnetometer,” Geometrics Inc., SERDP Project MR-1512, Mar. 2011.
- [25] R. P. Cardoso, T. Belmonte, G. Henrion, and N. Sadeghi, “Influence of trace oxygen on He(2 3S) density in a He–O<sub>2</sub> microwave discharge at atmospheric pressure: behaviour of the time afterglow,” *J. Phys. Appl. Phys.*, vol. 39, no. 19, p. 4178, Oct. 2006.
- [26] Y. P. Raizer, M. N. Shneider, and N. A. Yatsenko, *Radio-Frequency Capacitive Discharges*, 1st ed. CRC Press, 1995.
- [27] “RF Inductance Calculator - HAMwaves.com.” [Online]. Available: <http://hamwaves.com/antennas/inductance.html>. [Accessed: 15-May-2013].
- [28] L. F. Berzak, S. E. Dorfman, and S. P. Smith, “Paschen’s Law in Air and Noble Gases,” Lawrence Berkeley National Laboratory, Apr. 2006.
- [29] Y. Sakiyama, “Minicourse: Low temperature plasma modelling and simulations and applications.” University of California, Berkley.
- [30] S. C. Brown, “Breakdown in Gases: Alternating and High-Frequency Fields,” in *Gas Discharges II / Gasentladungen II*, vol. 4 / 22, S. Flügge, Ed. Berlin, Heidelberg: Springer Berlin Heidelberg, 1956, pp. 531–575.
- [31] J. Park, I. Henins, H. W. Herrmann, and G. S. Selwyn, “Gas breakdown in an atmospheric pressure radio-frequency capacitive plasma source,” *J. Appl. Phys.*, vol. 89, no. 1, pp. 15–19, Jan. 2001.
- [32] “Daniel A. Steck, ‘Rubidium 85 D Line Data,’ available online at <http://steck.us/alkalidata> (revision 2.1.6, 20 September 2013).”
- [33] A. V. Phelps and J. P. Molnar, “Lifetimes of Metastable States of Noble Gases,” *Phys. Rev.*, vol. 89, no. 6, pp. 1202–1208, Mar. 1953.
- [34] A. V. Phelps, “Absorption Studies of Helium Metastable Atoms and Molecules,” *Phys. Rev.*, vol. 99, no. 4, pp. 1307–1313, août 1955.
- [35] M. A. Lieberman and A. J. Lichtenberg, *Principles of Plasma Discharges and Materials Processing*, 2nd Edition, 2nd ed. Wiley-Interscience, 2005.
- [36] Y. Ichikawa and S. Teii, “Molecular ion and metastable atom formations and their effects on the electron temperature in medium-pressure rare-gas positive-column plasmas,” *J. Phys. Appl. Phys.*, vol. 13, no. 11, p. 2031, Nov. 1980.
- [37] M. Surendra, “Radiofrequency discharge benchmark model comparison,” *Plasma Sources Sci. Technol.*, vol. 4, no. 1, p. 56, Feb. 1995.
- [38] X. Yuan and L. L. Raja, “Computational study of capacitively coupled high-pressure glow discharges in helium,” *IEEE Trans. Plasma Sci.*, vol. 31, no. 4, pp. 495–503, Aug.
- [39] P. M. Banks, “Collision Frequencies and Energy Transfer - Electrons,” Office of Naval Research, 1966.
- [40] J. W. Shon and M. J. Kushner, “Excitation mechanisms and gain modeling of the high-pressure atomic Ar laser in He/Ar mixtures,” *J. Appl. Phys.*, vol. 75, no. 4, pp. 1883–1890, Feb.
- [41] S. Rauf and M. J. Kushner, “Dynamics of a coplanar-electrode plasma display panel cell. I. Basic operation,” *J. Appl. Phys.*, vol. 85, no. 7, pp. 3460–3469, Apr. 1999.
- [42] Y. Sakiyama and D. B. Graves, “Corona-glow transition in the atmospheric pressure RF-excited plasma needle,” *J. Phys. Appl. Phys.*, vol. 39, no. 16, p. 3644, Aug. 2006.
- [43] N. Sadeghi-Kaharrazi, “Etude des différents processus de désexcitation des atomes métastables de l’hélium au sein d’un milieu ionisé,” Université de Grenoble, Laboratoire de Spectrométrie Physique CNRS, 1967.
- [44] A. C. G. Mitchell and M. W. Zemansky, *Resonance Radiation and Excited Atoms*. The SYSDIOS of the Cambridge University Press, 1961.
- [45] B. Niermann, T. Hemke, N. Y. Babaeva, M. Böke, M. J. Kushner, T. Mussenbrock, and J. Winter, “Spatial dynamics of helium metastables in sheath or bulk dominated rf micro-plasma jets,” *J. Phys. Appl. Phys.*, vol. 44, no. 48, p. 485204, Dec. 2011.

- [46] D. D. McGregor, "High-sensitivity helium resonance magnetometers," *Rev. Sci. Instrum.*, vol. 58, no. 6, pp. 1067–1076, Jun. 1987.
- [47] D. Budker and M. Romalis, "Optical magnetometry," *Nat. Phys.*, vol. 3, no. 4, pp. 227–234, avril 2007.
- [48] R. Jimenez-Martinez, W. C. Griffith, Y.-J. Wang, S. Knappe, J. Kitching, K. Smith, and M. D. Prouty, "Sensitivity Comparison of Mx and Frequency-Modulated Bell-Bloom Cs Magnetometers in a Microfabricated Cell," *IEEE Trans. Instrum. Meas.*, vol. 59, no. 2, pp. 372–378, 2010.
- [49] W. E. Bell and A. L. Bloom, "Optically Driven Spin Precession," *Phys. Rev. Lett.*, vol. 6, no. 6, pp. 280–281, Mar. 1961.
- [50] S. J. Seltzer, "Developments in Alkali-Metal Atomic Magnetometry," Princeton University, 2008.
- [51] J. Hamel, A. Cassimi, H. Abu-Safia, M. Leduc, and L. D. Scheerer, "Diode pumping of LNA lasers for helium optical pumping," *Opt. Commun.*, vol. 63, no. 2, pp. 114–117, Jul. 1987.
- [52] W. Fourcalt, J.-M. Léger, V. Costes, I. Fratter, and L. Mondin, "Athermal Fiber Laser for the SWARM Absolute Scalar Magnetometer," presented at the ICSO 2010, Rhodes, Grece, 2010.
- [53] C. E. Wieman and L. Hollberg, "Using diode lasers for atomic physics," *Rev. Sci. Instrum.*, vol. 62, no. 1, pp. 1–20, Jan. 1991.
- [54] R. W. Tkach and A. R. Chraplyvy, "Regimes of feedback effects in 1.5-  $\mu$ m distributed feedback lasers," *J. Light. Technol.*, vol. 4, no. 11, pp. 1655–1661, Nov.
- [55] C. Guttin, J. M. Leger, and F. Stoeckel, "An isotropic earth field scalar magnetometer using optically pumped helium 4," *J. Phys. IV*, vol. 04, no. C4, pp. C4–655–C4–659, Apr. 1994.
- [56] "Mini Dynamic Polarization Controller MPC - General Photonics Corporation." [Online]. Available: <http://www.generalphotonics.com/productOffline.aspx?dept=10&cp=55>. [Accessed: 26-Nov-2013].
- [57] H. Jiang, Y. K. Zou, Q. Chen, K. K. Li, R. Zhang, Y. Wang, H. Ming, and Z. Zheng, "Transparent electro-optic ceramics and devices," 2005, vol. 5644, pp. 380–394.
- [58] S. Thaniyavarn, "Wavelength independent, optical damage immune Z-propagation LiNbO<sub>3</sub> waveguide polarization converter," *Appl. Phys. Lett.*, vol. 47, no. 7, p. 674, 1985.
- [59] "Liquid Crystal: Meadowlark Optics." [Online]. Available: [http://www.meadowlark.com/liquid\\_crystal.php?pg=lcd](http://www.meadowlark.com/liquid_crystal.php?pg=lcd). [Accessed: 26-Nov-2013].
- [60] L. Nieradko, C. Gorecki, A. Douahi, V. Giordano, J. C. Beugnot, J. Dziuban, and M. Moraja, "New approach of fabrication and dispensing of micromachined cesium vapor cell," *J. MicroNanolithography MEMS MOEMS*, vol. 7, no. 3, pp. 033013–033013–6, 2008.
- [61] M. Hasegawa, R. K. Chutani, C. Gorecki, R. Boudot, P. Dziuban, V. Giordano, S. Clatot, and L. Mauri, "Microfabrication of cesium vapor cells with buffer gas for MEMS atomic clocks," *Sens. Actuators Phys.*, vol. 167, no. 2, pp. 594–601, Jun. 2011.



SPIM

■ École doctorale SPIM 16 route de Gray F - 25030 Besançon cedex

■ tél. +33 [0]3 81 66 66 02 ■ [ed-spim@univ-fcomte.fr](mailto:ed-spim@univ-fcomte.fr) ■ [www.ed-spim.univ-fcomte.fr](http://www.ed-spim.univ-fcomte.fr)



UNIVERSITÉ  
DE FRANCHE-COMTÉ